Site Effects on Spatial Coherency from Dense Arrays

N. Abrahamson

B27

ABSTRACT

The spatial coherency and amplitude variation of ground motion from ten dense seismic arrays are analyzed to examine the site-dependence of spatial variation of ground motion. The spatial coherencies computed for arrays located on alluvium are similar from array to array. The coherencies computed for arrays located on rock are lower than for arrays located on alluvium and show larger variability. The amplitude variation for arrays located on soil sites are also similar from array to array, but for rock site arrays, the amplitude variation is much larger than for soil site arrays. The aggregation of this information will be useful for estimating the overall uncertainty in spatial variation, with components from intra-event, inter-event and inter-site variability.

ACKNOWLEDGEMENTS

We thank and acknowledge the following institutions for making the array data available: Institute of Industrial Science, University of Tokyo for the Chiba Array; U.S. Geological Survey for the USGS Parkfield, Imperial Valley Differential, Hollister Differential, Coalinga, and Stanford arrays; University of California, Santa Cruz for the UCSC ZAYA array; and IRIS Data Management Center for the Pinyon Flat array.

CONTRACTOR SUMMARY

For separation distances of less than 100 m, the coherency at soil sites is not significantly different from the Lotung coherency functions. The coherency at rock sites is more variable than for soil sites and, on average, is lower than the Lotung coherency functions. The range of amplitude variations is greater than the range of coherencies, suggesting that amplitude variation is more sensitive to local site conditions than is coherency.

The analyses of the new array data also reinforce several results of a previous analysis of the EPRI LSST arrray. First, at separations <100 m coherency is not simply a function of wavelength, but rather a function of distance and frequency. Second, a comparison of weak and strong motion from the Chiba and Coalinga arrays shows no difference in observed spatial variation. We conclude that the Lotung spatial variation model is an adequate generic model for soil sites, with greater confidence in the coherency than the amplitude variation. The model over-estimates the average coherency for rock sites.

Ultimately, for the coherency and amplitude variation model to be applied routinely on a site-specific basis for engineering design, additional research is required. First, an inexpensive empirical method is needed to assess directly the level of site-dependence. In areas of high seismicity, recordings of small earthquakes over a range of azimuths and station separations should be sufficient. For application to low-seismicity sites, methods to utilize artificial sources are needed; our preliminary analysis indicates that use of microtremors is not promising. Work is also needed to develop a physical model for the process; numerical simulations should be performed to replicate the scattering phenomena observed and to provide insight into the sensitivity of observations to physical characteristics of the site. Further study should also examine the time dependency of coherency for P, S and surface waves. For engineering application, incoherent time histories should then be computed to determine the sensitivity of spatial variation to engineering analyses and the development of site-specific designs.

CONTENTS

1

INTRODUCTION

The spatial coherency of strong ground motions recorded by the EPRI/Taipower LSST array in Taiwan was analyzed and empirical coherency functions appropraite for use in soil-strucutre interaction studies were derived (EPRI RP2978-1). The LSST data set included recordings from a wide range of magnitudes, source distances, and focal mechanisms; however, the data were all from a single site condition. The most important aspect of the spatial coherency not resolved in this earlier study is the dependence of the coherency on local site condition.

In a preliminary test of the site effect on coherency, the coherencies computed from a small earthquake recorded by the EPRI Parkfiled array were compared to the Lotung coherency functions (EPRI RP2978-2). The EPRI Parkfield coherencies were found to be compatible with the Lotung coherency functions even though the local site conditions are quite different: Parkfield is a stiff site whereas Lotung is a soft soil site. This agreement suggested that the variations in the Lotung coherencies due to different seismic sources and ray paths may be large enough to encompass the coherency variations due to different site conditions. This previous study concluded that the Lotung coherency functions may be applicable to other sites, but additional tests of the Lotung coherency functions against coherencies from other earthquakes and sites were needed before the Lotung coherency functions can be confidently applied to other sites.

To evaluate the stablity of spatial variation of ground motion from site to site requires dense array recordings at multiple sites. By far, the largest set of dense array strong motion recordings are from the SMART 1 and LSST arrays in Taiwan; however, there are several other dense arrays in California and Japan that have recorded strong motions. In addition, there are several dense arrays that have recorded weak motions.

The objective of the current study is to determine if the spatial coherency and amplitude variations functions derived from the LSST array are applicable to other sites. In this study, we compare the spatial coherency and amplitude variations computed at 9 dense arrays with the empirical models developed for the extensive LSST data set to determine the importance of site-to-site variability.

2

ESTIMATION OF SPATIAL VARIATION

The spatial variation of ground motion has two parts: variation in waveform and variation in amplitude. Spatial coherency is used to describe the variation in the waveforms. The amplitude variation is used to describe scaling variations in the ground motion.

Estimation of Spatial Coherency

In this study, the coherency analysis procedure used by Abrahamson (1992) for the EPRI Lotung array data is followed. The estimation of coherency is breifly discussed below. A more detailed discussion is given by Abrahamson(1992).

The spatial variability of the ground motion waveforms can be quantified by the spatial coherency. Let $u_j(\omega)$ be the Fourier transform of the tapered time series $u_j(t)$, then

$$u_j(\omega) = \sum_{k=1}^{T} v(t_k)\, u_j(t_k) \exp\{-i\omega t_k\}, \tag{2-1}$$

where $v(t_k)$ is the data taper, T is the number of time samples, t_k is the time of the k^{th} sample, and ω is the frequency. The smoothed cross-spectrum is given by

$$S_{jk}(\omega) = \sum_{m=-M}^{M} a_m\, u_j(\omega_m)\bar{u}_k(\omega_m)\,, \tag{2-2}$$

where 2M+1 is the number of discrete frequencies smoothed, $\omega_m=\omega+2\pi m/T$, a_m are the weights used in the frequency smoothing, and the overbar indicates the complex conjugate. The coherency, $\gamma_{ij}(\omega)$, is given by

$$\gamma_{ij}(\omega) = \frac{S_{ij}(\omega)}{S_{ii}(\omega)S_{jj}(\omega)} \tag{2-3}$$

where $S_{ij}(\omega)$ is the smoothed cross-spectrum for stations i and j. As shown in Eq. 2-3, the coherency is a complex number. In this study, we use the absolute value of the coherency (sometimes called the lagged coherency because it lags the data to remove the wave-passage effect). A $\tanh^{-1}$ transformation is used to produce an approximately normal distribution (Enochson and Goodman, 1968).

The computed lagged coherency depends strongly on the selected frequency smoothing. An 11-point Hamming window is used for the frequency smoothing (a_m) and a 5% double cosine bell taper is used for the data window ($v(t)$). In order to make consistent comparisons of coherency for differenct events, it is important to keep the number of discrete frequencies smoothed fixed. This can lead to different frequency bands for the frequency smoothing if the window lengths are not the same for all events.

Estimation of Amplitude Variation

The spatial coherency discussed above measures the variations in the waveforms across the array. The variation in the scaling of the ground motion across the array can also be measured. This type of variation can be quantified by the standard error of the Fourier amplitude spectrum across the array.

Let $A_{ij}(\omega)$ be the Fourier amplitude spectrum of the transverse component for the j^{th} station for the i^{th} earthquake. Let $\Delta A_{ijk}(\omega)$ be the difference between the log spectral amplitude of the j^{th} and k^{th} stations from the i^{th} event. That is

$$\Delta A_{ijk}(\omega) = \ln A_{ij}(\omega) - \ln A_{ik}(\omega). \qquad (2\text{-}4)$$

The Fourier amplitude spectrum is assumed to be log-normally distributed with a variance that depends on the frequency smoothing (Brillinger, 1985). Let $\sigma(\omega,\xi)$ be the standard deviation of $A(\omega)$ and assume that $\sigma(\omega,\xi)$ is independent of the event, then $\Delta A_{ijk}(\omega)$ is normally distributed with mean zero and standard deviation $\sqrt{2}\sigma(\omega,\xi)$. Calculations of $\Delta A_{ijk}(\omega)$ are used to estimate $\sigma(\omega,\xi)$. To be consistent with the coherency analysis, the same frequency smoothing (Hamming window, M=5) is used is estimate the amplitude spectra.

3

DATA SET OF ARRAY RECORDINGS

The largest set of dense-array strong-motion recordings are from the SMART-1 and LSST arrays in Taiwan; however, there are several other dense arrays in California and Japan that have recorded strong motions. In addition, there are several dense arrays that have recorded weak motions.

We considered only arrays with minimum station separations of less than 100 m and obtained recordings from ten dense arrays for use in the analysis. The arrays and their general characteristics are listed in Table 3-1. For this study, the arrays have been grouped only by the general site classes of soil and rock, with five arrays on rock and five on soil. The data sets for each array are summarized in Table 3-2. Five of the arrays have recorded strong motion and five have recorded only weak motion. The individual events for each array are listed in Tables 3-3 to 3-12.

The lack of magnitude and distance dependence on spatial coherency observed at Lotung (Schneider et al., 1990; Abrahamson, 1992) indicates that comparisons of spatial coherency observed at different sites can be made using a mixture of small and large earthquakes recorded over a wide range of distances without contributing a significant bias. While a lack of bias is assumed in the comparisons made here, it is expected that in the extremes, observations from large/small magnitude and/or distant/close earthquakes may yield significant departures from the mean. In particular, if the signal amplitudes are low (due to a small magnitude or large distance) then the coherency is expected to be low due to the poor signal-to-noise ratio. This is most likely a problem for low frequencies from small magnitude events.

The level of site characterization at the arrays differs greatly. Some of the arrays have had extensive geotechnical site investigations, other arrays just surface geologic information, and some have almost no site information. The available information for the individual arrays is given below.

EPRI/Taipower LSST Array

The Lotung LSST array is located in northeastern Taiwan near the town of Lotung (Figure 3-1). It is located at the southern end of the Lanyang River plain. The array was installed in 1985 as part of a joint program by EPRI and Taipower.

The array consists of free-field surface, free-field downhole, and structure instruments. Only the free-field surface stations were used in the coherency study. The surface array consists 15 three-component force balanced accelerometers. The stations are configured in a Y-shaped array with a 85 m radius (Figure 3-2). To avoid soil structure interaction effects on the coherency, the station closest to the structure on each arm was not used in the analysis. The topography in the array region is flat.

Extensive in situ and laboratory studies were conducted to define the soil statigraphy and geotechnical properties beneath the LSST array (Anderson and Tang, 1987). A total of 12 drill holes to depths of from 30 to 150 m were sampled. In the top 50 m, the S-wave velocities from cross-hole and u-hole seismic tests is 100 m/s near the surface and increases to 250 m/s at 18 m depth. It remains 250/s to a depth of 50 m. The results of laboratory tests also indicate that the shear modulus and damping becomes nonlinear at shear strains of about 10^{-2}%. Recent observations of vertical transfer functions obtained from selected LSST recorded earthquakes suggest that nonlinearity is significant at accelerations of about 0.15g (Chang et al., 1989). For this study, this site is classified as a soil site.

EPRI Parkfield Array

In anticipation of the rupture of the Parkfield segment of the San Andreas fault, EPRI installed a dense strong motion array at Stone Corral, about 15 km southeast of Parkfield (Figure 3-3). The array is located 7 km east of the San Andreas Fault along the rupture zone of the 1966 Parkfield earthquake. The array has been fully operation since November 1987.

The array consists of 21 three-component force-balanced accelerometers connected to a central recording facility on site. There are 13 surface and 8 downhole elements distributed to 90 m depth. This study only considers the surface stations. The surface stations are configured in a Y-shaped array with a 120 m radius (Figure 3-4). The topography in the array region is fairly flat.

The site has been characterized using a variety of geotechnical methods (EPRI RP2556-40). Studies include: 1) Reconnaissance geologic mapping of surface exposures; 2) stratigraphic mapping and mineralogic analysis from drilling and coring of 4 6-cm boreholes to a maximum depth of 120 m; 3) uphole-downhole seismic velocity profiling for P and S waves to 90 m depth; and 4) seismic refraction analysis from four profiles extending parallel and perpendicular to structure and extending from 180 m to 460 m in length. The refraction data yield P-wave velocity information to about 150 m depth throughout the array.

The site array site is located in a complex tectonic block on the northeast side of the San Andreas Fault. The deep basement in the area is composed of pervasively sheared Franciscan and related ultramafic rocks of Mesozoic age. The basement rocks are overlain by about 5000 m of Tertiary and Cretaceous marine sedimentary rocks. The basement and overlying meta-sedimentary rocks have been progressively transposed into a series of NW-SE trending en echelon folds and faulted folds, probably in response to the right-lateral shear associated with the San Andreas Fault system.

The central portion of the seismic array is located on an old (> 10,000 years) alluvial deposit which is up to about 6 m thick. The bedrock underlying and surrounding the array is predominantly sandstone of the Miocene Temblor Formation (Diblee, 1971). A small area of mudstone and siltstone is also mapped at the surface in the northwestern portion of the array. The array is located on the eastern limb of a steep, NW plunging, N40W trending asymmetric syncline. At the array center, the Temblor formation extends from 6m depth to below 90 m, with a bedding plane dip of 70°. For this study, this site is classified as a rock site.

Chiba Array

The Chiba array is located at the Chiba experiment station approximately 30 km east of Tokyo (Figure 3-5). The array became operational in April 1982.

The Chiba array consists of 15 three-component near surface accelerometers in an area about 300m x 400m (Figure 3-6). There is a very dense subarray which contains 9 of the 15 stations in an area about 30m x 30m. The near-surface stations are buried at a depth of 1 m. There are also 29 three-component downhole accelerometers at depths ranging from 5 to 40 m. Only the 1 m depth stations are used in this study.

The ground at the Chiba array is very flat at the array and the soils are uniform. The soil profile consists of about 3-5 km of loam over about 5 m of sandy clay and clayey sand. There is more than 30 m of fine sands below the clayey sands. The shear wave velocity of these layers are approximately 140 m/s, 320 m/s and 320-420m/s, respectively. A complete description of the array is given by Katayama et al. (1990). For this study, this site is classified as a soil site.

USGS Parkfield Array

The USGS Parkfield array is located at Work Ranch due west of Gold Hill (Figure 3-7). The array is located about 8 km southwest of the San Andreas Fault. This area has steep topography. The instruments are located along ridge line with about 50 m of relief and slopes of about 45 degrees.

The array consists of 14 six component GEOS seismometers (a three-component force-balanced accelerometer and a three-component velocity transducer). The accelerometers are for strong ground motion and the velocity transducers are for weak motions. The instruments are configured in an irregular pattern along the ridge line (Figure 3-8). A detailed description of the array and instrumentation is given by Fletcher et al (1991).

The array is located on the Paso Robles Formation which is a loosely consolidated gravel and sandstone unit about 500 m thick. It is underlain by more consolidated layers of sandstone and shale to a depth of about 1500 m at which there is granite. For this study, this site is classified as a rock site.

Imperial Valley Differential Array

The Imperial Valley Differential array is located in the Imperial Valley about 4 km west of the Imperial Fault (Figure 3-9). This fault was the source of the 1979 Imperial Valley Earthquake.

The array consists of 5 three-component force-balanced accelerometers stations. The instruments are configured in a north-south line (Figure 3-10).

The array is located at a deep soil site. The surface velocities were measured at the site from drill holes and refraction surveys (Smith et al., 1982). The top 12 m has a shear wave velocity of about 150 m/s. Below this top layer, the shear-wave velocity is about 200 m/s to a depth of about 330 m. The total depth of the sediments in the Imperial Valley is about 5 km. For this study, this site is classified as a soil site.

Hollister Differential Array

The Hollister differential array is located at the Hollister airport (Figure 3-11). It is located about 10 km northeast of the San Andreas fault. The array was installed and operated by the USGS.

The array consists of 7 three-component accelerometers in a V-shape (Figure 3-12). The lengths of the two arms of the array are 2015m and 1000 m.

There are no measurements of the site velocities available; however, the region is deep alluvium. For this study, this site is classified as a soil site.

Stanford Temporary Array

Following the 1989 Loma Prieta earthquake, the USGS deployed a temporary dense array at Stanford near SLAC (Mueller and Glasmoyer, 1990). The array is located about 4 km east of the San Andreas Fault, about 30 km northwest of the Loma Prieta rupture zone (Figure 3-13).

The array consists of 4 three-component GEOS seismometers. The instruments are configured in a line (Figure 3-14).

There is no information available about the site velocities, however, based on the regional geology, the site is classified as a soil site for this study.

Coalinga Temporary Array

The USGS Coalinga Temporary Array was deployed during the aftershock sequence of the 1985 Coalinga earthquake (Mueller et al. (1984). The array is located 10 km north of Coalinga on Anticline ridge (Figure 3-15).

The array consists of a 7 stations that are a mix of accelerometers and velocity transducers. The instruments are configured in a V-shape array (Figure 3-16). In this study, only the accelerometer data are used.

The array is located on the sandstone outcrop along anticline ridge. No other site-specific information on the site velocities is available. For this study, this site is classified as a rock site.

UCSC ZAYA TemporaryArray

Following the 1989 Loma Prieta earthquake, UCSC deployed a temporary dense array in the Santa Cruz mountains to measure aftershocks (Bonamassa et al., 1991). Recordings from three earthquakes were available during this study. The locations of the epicenters are shown in Figure 3-17.

The ZAYA array consists of 6 stations configured in two concentric triangles (Figure 3-18). The triangles are close to equilateral with sides of length 25m and 300 m. The stations in the inner triangle are located in a fairly flat region between two ridges. The stations in the outer triangle are located up the ridges.

There are no measurements of the site velocities available. Based on the regional geology, the site is classified as a rock site for this study.

Pinyon Flat Temporary Array

The Pinyon Flat array is located in Southern California between the San Jacinto and southern San Andreas Faults (Figure 3-19). The array was deployed as part of a PASSCAL experiment to study wave propagation, scattering, and spatial variations (Owens et al. 1991).

The Pinyon Flat array consists of 71 force-balanced accelerometers. The array has two part. In one part, the instruments are configured in an L-Shaped array and in the second part 49 instruments are configured in a dense grid with 7 m spacing (Figure 3-20).

The Pinyon Flat area consists of granite. Only P-wave velocities at the site are available at this time. In the top 2 meters, the P-wave velocity in the weathered rock ranges from 400 to 1300 m/s with an average of about 600 m/s (Pavlis, 1992). There are large lateral variations in the P-wave velocities of the near-surface rock indicating that the weathering is less along the southern arm of the array. Based on nearby boreholes, the shear-wave velocity has been estimated at 250 m/s at the surface and increasing to 890 m/s at a depth of 8 m and to 1,650 m/s at a depth of 13.5 m (Hanson, 1992). For this study, the site is classified as a rock site.

Table 3-1.
Dense Array Characteristics

Array	Location	Site Class	Surface Stations	Spacing (m) Min	Max
EPRI LSST	Taiwan	Soil	15	3	85
EPRI Parkfield	CA	Rock	13	10	191
Chiba	Japan	Soil	15	5	319
USGS Parkfield	CA	Rock	14	25	952
Imperial Valley Diff	CA	Soil	5	18	213
Hollister Diff	CA	Soil	4	61	256
Stanford (temp)	CA	Soil	4	32	185
Coalinga (temp)	CA	Rock	7	48	313
UCSC ZIYA (temp)	CA	Rock	6	25	300
Pinyon Flat (temp)	CA	Rock	58	7	340

Table 3-2.
Dense Array Data Sets

Array	No.of Eqk Analyzed	Mag Min	Mag Max	Dist (km) Min	Dist (km) Max	Max GM
EPRI LSST	15	3.0	7.8	5	113	0.26g
EPRI Parkfield	2	3.0	3.9	13	15	0.04g
Chiba	9	4.8	6.7	61	105	0.41g
USGS Parkfield	9	2.2	3.5	18	45	0.04g
Imperial Valley Diff	2	5.1	6.5	4	14	0.89g
Hollister Diff	1	5.3	5.3	17	17	0.20g
Stanford (temp)	4	≈3.5	≈4.5			0.007g
Coalinga (temp)	6	2.3	5.2	≈10	≈15	0.21g
UCSC ZIYA (temp)	3	2.3	3.0	9	19	
Pinyon Flat (temp)	6	2.0	3.6	14	39	

Table 3-3.
Events Recorded by the LSST Array

Event Name	Date	Time	M	Epicentral Dist (km)	Depth (km)	Az (degrees)	No. Stations
event 2	10/26/85		4.6	29	1	165	7
event 3	11/07/85		4.7	81	79	30	11
event 4	1/16/86		6.0	26	10	61	10
event 5	3/29/86		3.9	13	10	159	12
event 6	4/08/86		4.3	33	11	174	11
event 7	5/20/86		6.4	71	16	195	11
event 8	5/20/86		5.5	72	22	192	11
event 10	7/16/86		3.7	6	1	162	10
event 11	7/17/86		4.1	6	2	90	10
event 12	7/30/86		5.6	4	2	131	12
event 13	7/30/86		-	5	-	90	12
event 14	7/30/86		4.1	5	2	119	10
event 15	8/05/86		-	5	-	120	10
event 16	11/14/86		7.8	68	7	174	9
event 17	11/14/86		6.3	80	-	180	9

Table 3-4.
Events Recorded by the EPRI Parkfield Array

Event Name	Date	Time	M	Epicentral Dist (km)	Depth (km)	Az (degrees)	No. Stations
event 1	10/23/88	00:00	3.0	9	9	210	13
event 2	5/25/89	00:00	3.9	12	9	275	10

Table 3-5.
Events Recorded by the Chiba Array

Event Name	Date	Time	M	Epicentral Dist (km)	Depth (km)	Az (degrees)	No. Stations
8307	2/27/83		6.0	35	72	353	11
8420	12/17/84		4.9	5	78	120	11
8510	6/8/85		4.8	16	64	234	15
8519	10/4/85		6.1	28	78	351	15
8525	11/16/85		5.0	32	63	202	15
8722	12/17/87		6.7	45	58	232	11
8806	1/16/88		5.2	38	48	226	11
8816	3/18/88		6.0	42	96	84	15
8901	2/19/89		5.6	48	55	22	12

Table 3-6.
Events Recorded by the USGS Parkfield Array

Event Name	Date	Time	M	Epicentral Dist (km)	Depth (km)	Az (degrees)	No. Stations
event 1	8/2/90	01:00	3.1	30	11	123	11
event 3	8/28/90	02:38	2.9	30	10	124	11
event 4	9/10/90	06:53	3.3	19	5	345	12
event 5	11/14/90	19:34	2.7	16	10	353	11
event 6	11/28/90	03:42	2.2	14	14	4	11
event 7	11/30/90	04:25	2.3	13	13	3	11
event 8	12/10/90	02:34	3.5	36	17	58	11
event 9	12/19/90	16:25	2.8	45	4	257	11
event 10	12/26/90	23:02	2.5	22	5	342	9

Table 3-7.
Events Recorded by the Imperial Valley Differential Array

Event Name	Date	Time	M	Epicentral Dist (km)	Depth (km)	Az (degrees)	No. Stations
event A	10/15/79		6.5	4	0	60	4
event B	10/15/79		5.1	10	10	111	5

Event A location given by the closest distance from the site to the fault rupture

Table 3-8.
Events Recorded by the Hollister Differential Array

Event Name	Date	Time	M	Epicentral Dist (km)	Depth (km)	Az (degrees)	No. Stations
event 1	2/20/88		5.3	14	9	136	4

Table 3-9.
Events Recorded by the Stanford Temporary Array

Event Name	Date	Time	M	Epicentral Dist (km)	Depth (km)	Az (degrees)	No. Stations
event 1	3/10/90		≈4	≈40			3
event 2	3/11/90		≈4	≈40			4
event 3	3/12/90		≈4	≈40			4
event 4	3/13/90		≈4	≈40			4

Table 3-10.
Events Recorded by the Coalinga Temporary Array

Event Name	Date	Time	M	Epicentral Dist (km)	Depth (km)	Az (degrees)	No. Stations
126E57	5/6/83	04:57	3.3				4
126H43	5/6/83	07:43	2.3				4
126S31	5/6/83	18:31	3.2				4
127A17	5/7/83	00:17	3.2				4
129C49	5/9/83	02:49	5.2	1	12	179	4
129D26	5/9/83	03:26	4.1				4

Table 3-11.
Events Recorded by the ZAYA Temporary Array

Event Name	Date	Time	M	Epicentral Dist (km)	Depth (km)	Az (degrees)	No. Stations
318	11/14/89	4:50	2.3	7	5	51	6
319	11/15/89	13:04	2.6	15	12	129	6
320	11/16/89	4:59	3.0	5	11	333	6

Table 3-12.
Events Recorded by the Pinyon Flat Temporary Array

Event Name	Date	Time	M	Epicentral Dist (km)	Depth (km)	Az (degrees)	No. Stations
event 1	4/18/90	14:25	3.0	39	5	43	58
event 2	4/18/90	14:32	3.6	39	5	43	58
event 3	5/2/90	11:34	2.1	13	7	182	58
event 4	5/5/90	08:10	2.0	12	8	184	58
event 5	5/14/90	05:05	2.6	16	12	239	58
event 6	5/16/90	01:14	2.4	19	11	178	58

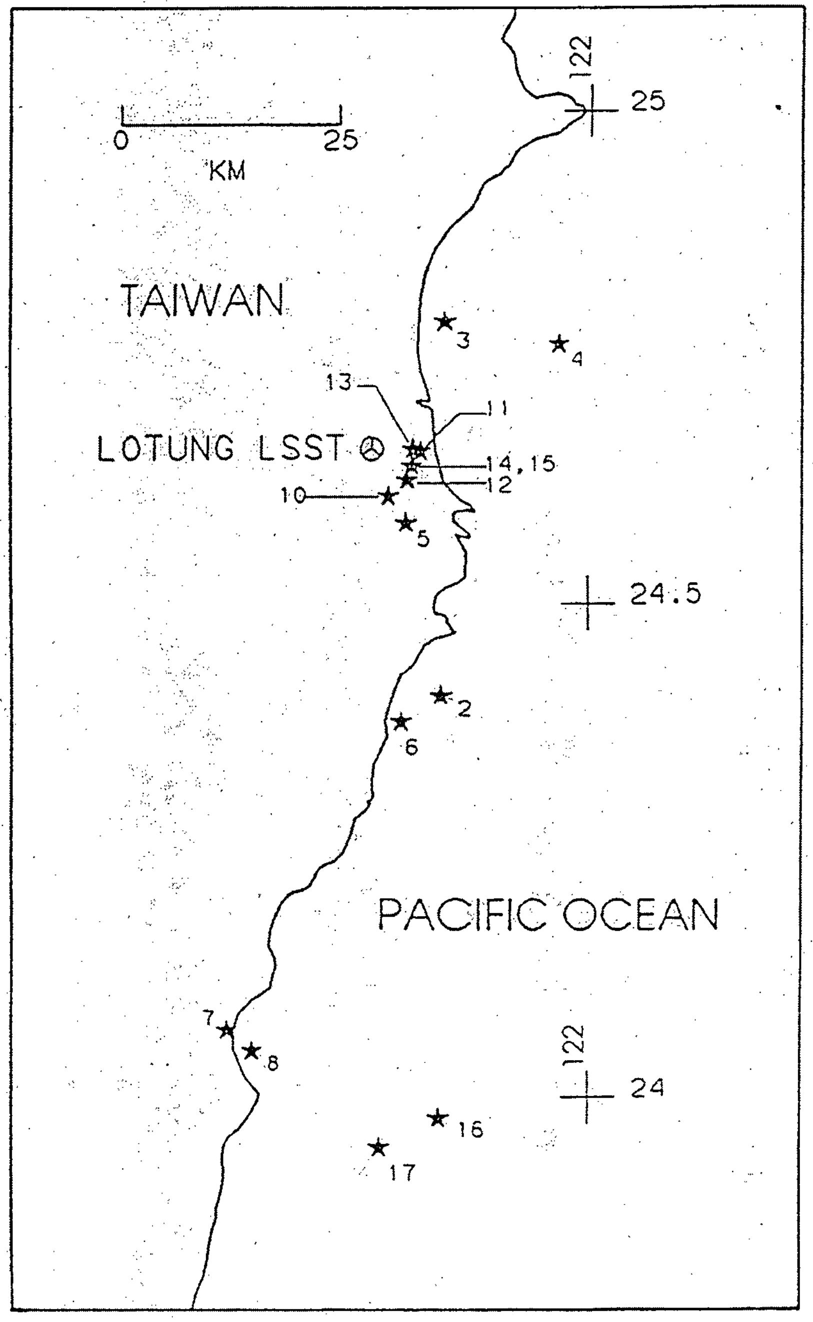

Figure 3-1. Location of the EPRI/Taipower LSST array and epicenters of recorded events.

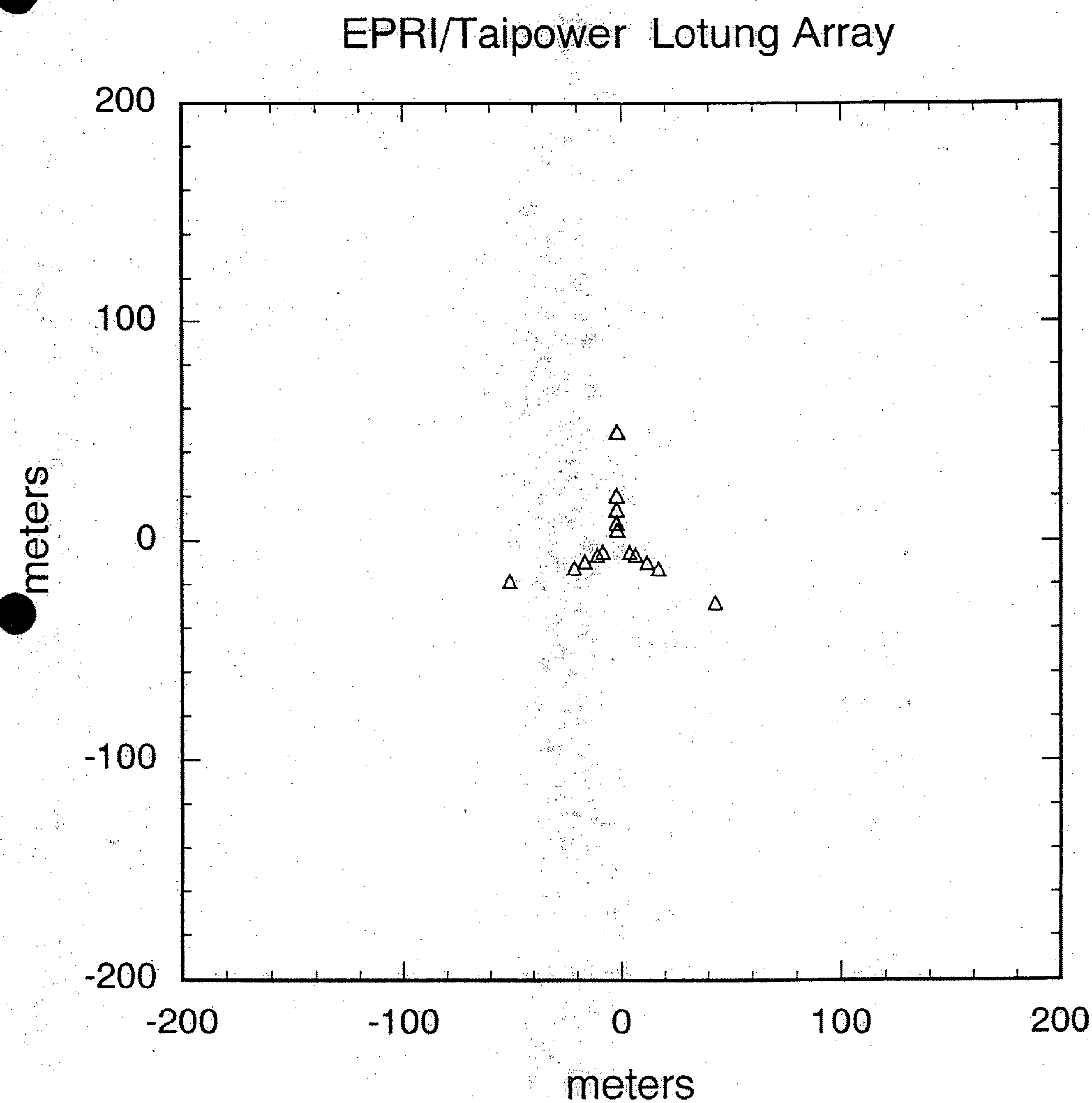

Figure 3-2. Array configuration of the EPRI/Taipower LSST array.

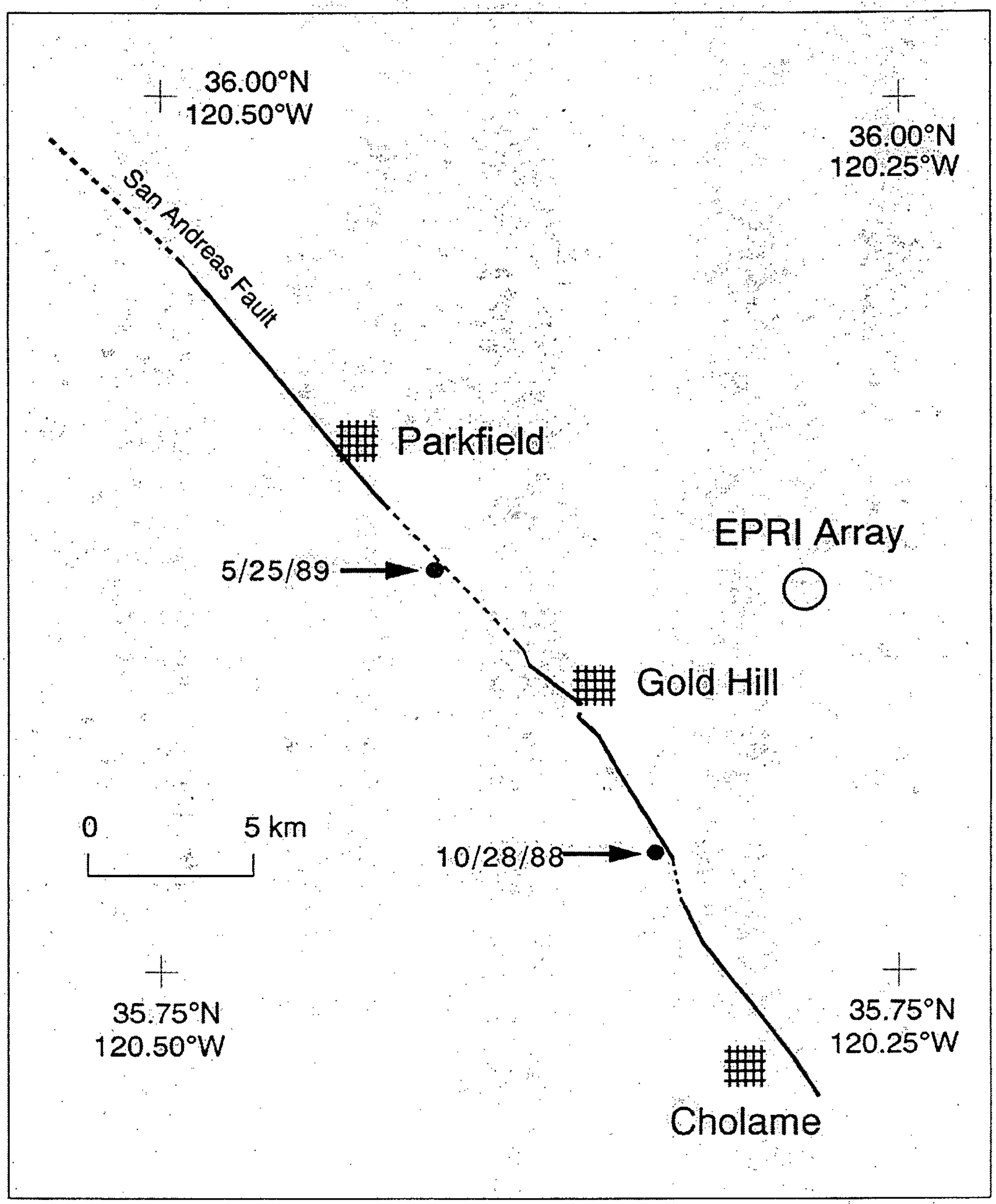

Figure 3-3. Location of the EPRI Parkfield array and epicenters of recorded events.

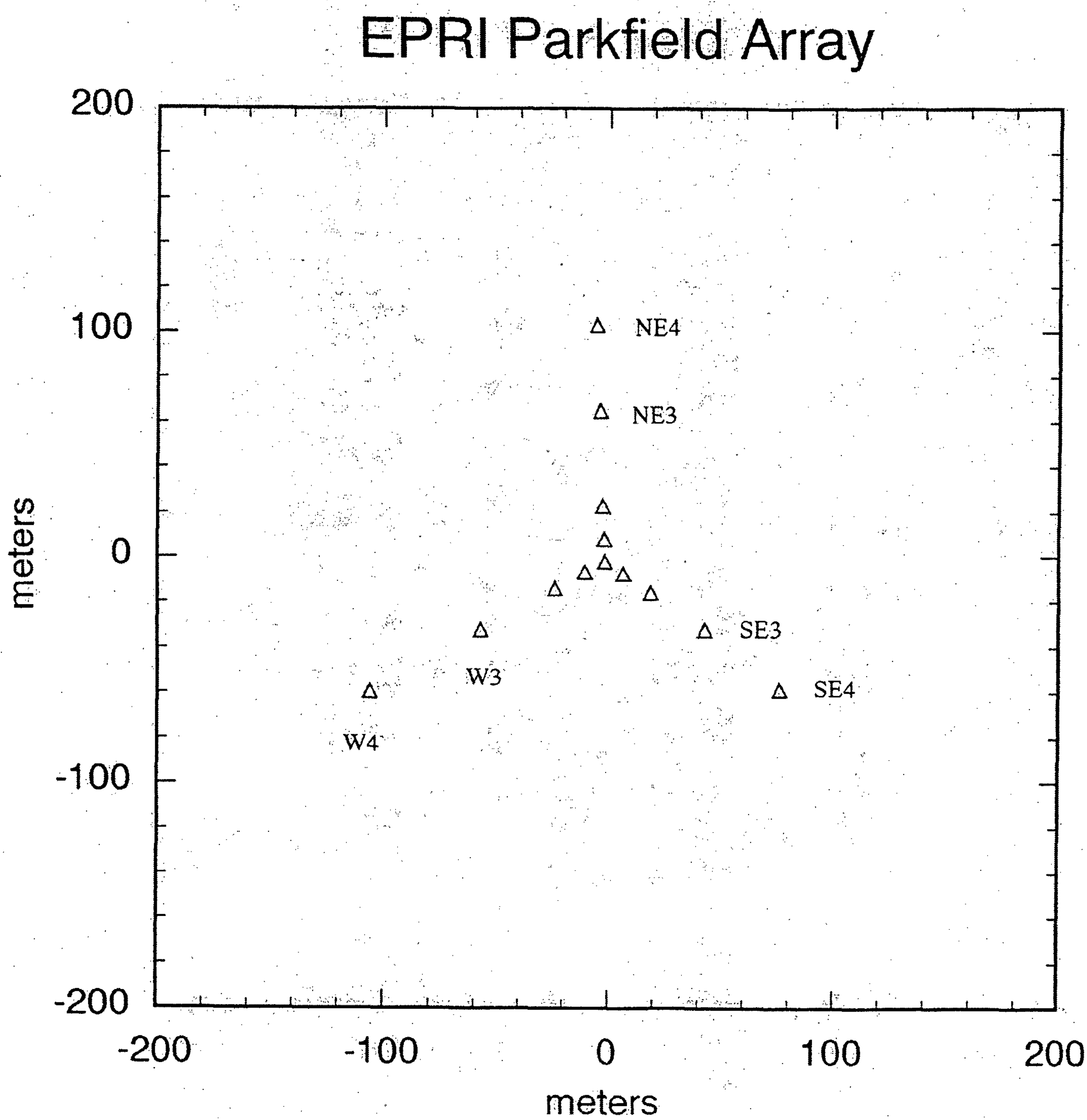

Figure 3-4. Array configuration of the EPRI Parkfield array.

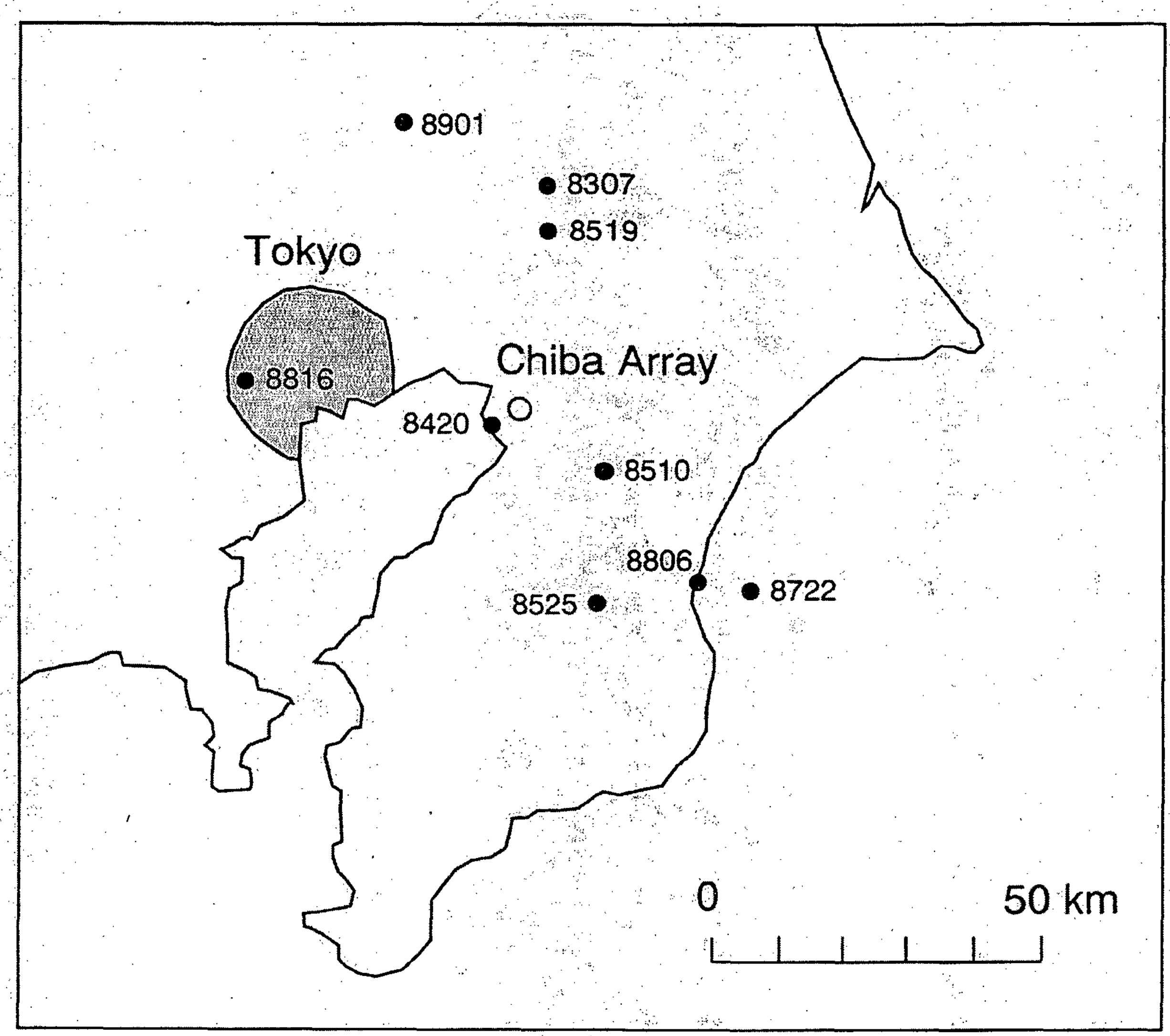

Figure 3-5. Location of the Chiba array and epicenters of recorded events.

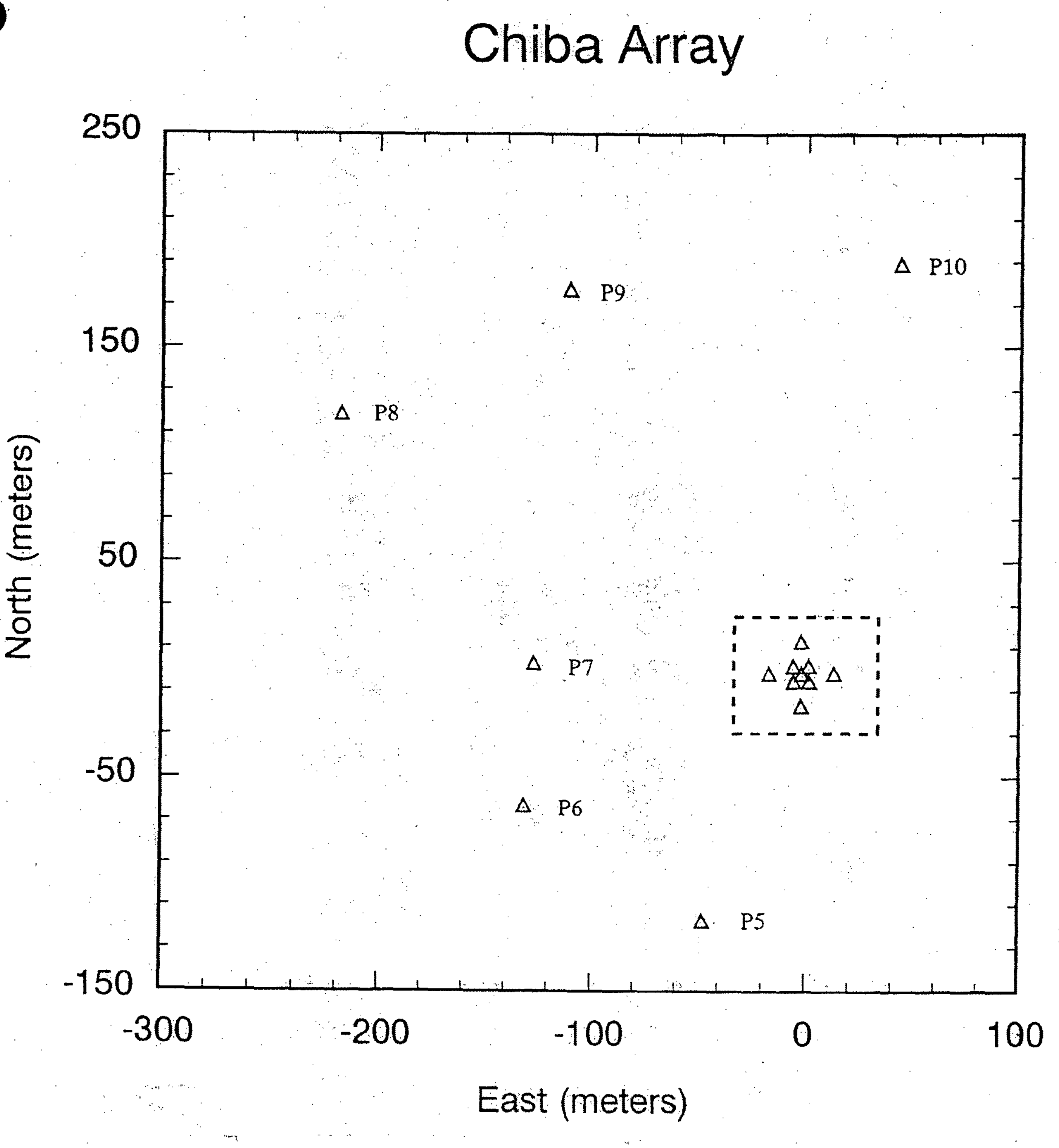

Figure 3-6. Array configuration of the Chiba array.

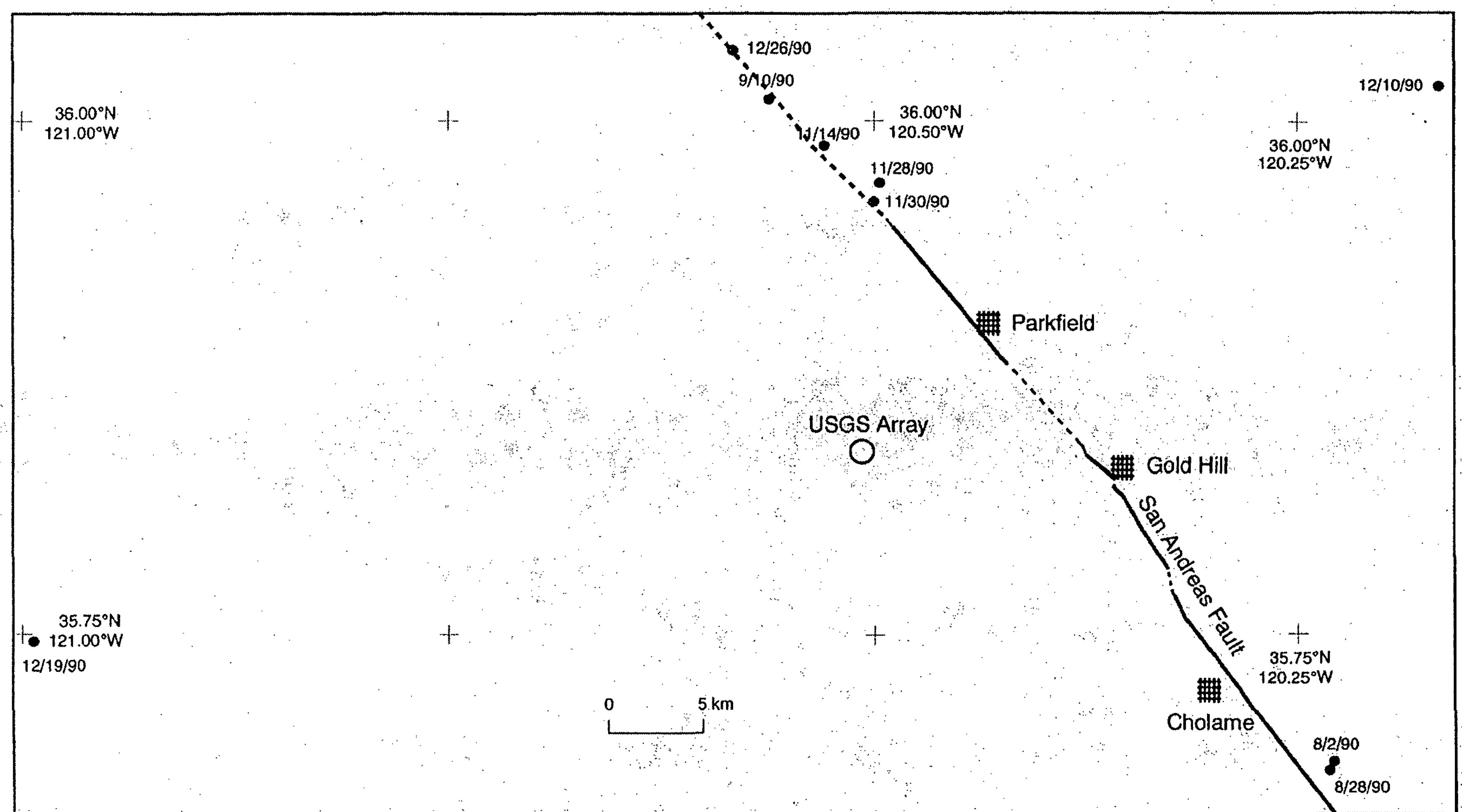

Figure 3-7. Location of the USGS Parkfield array and epicenters of recorded events.

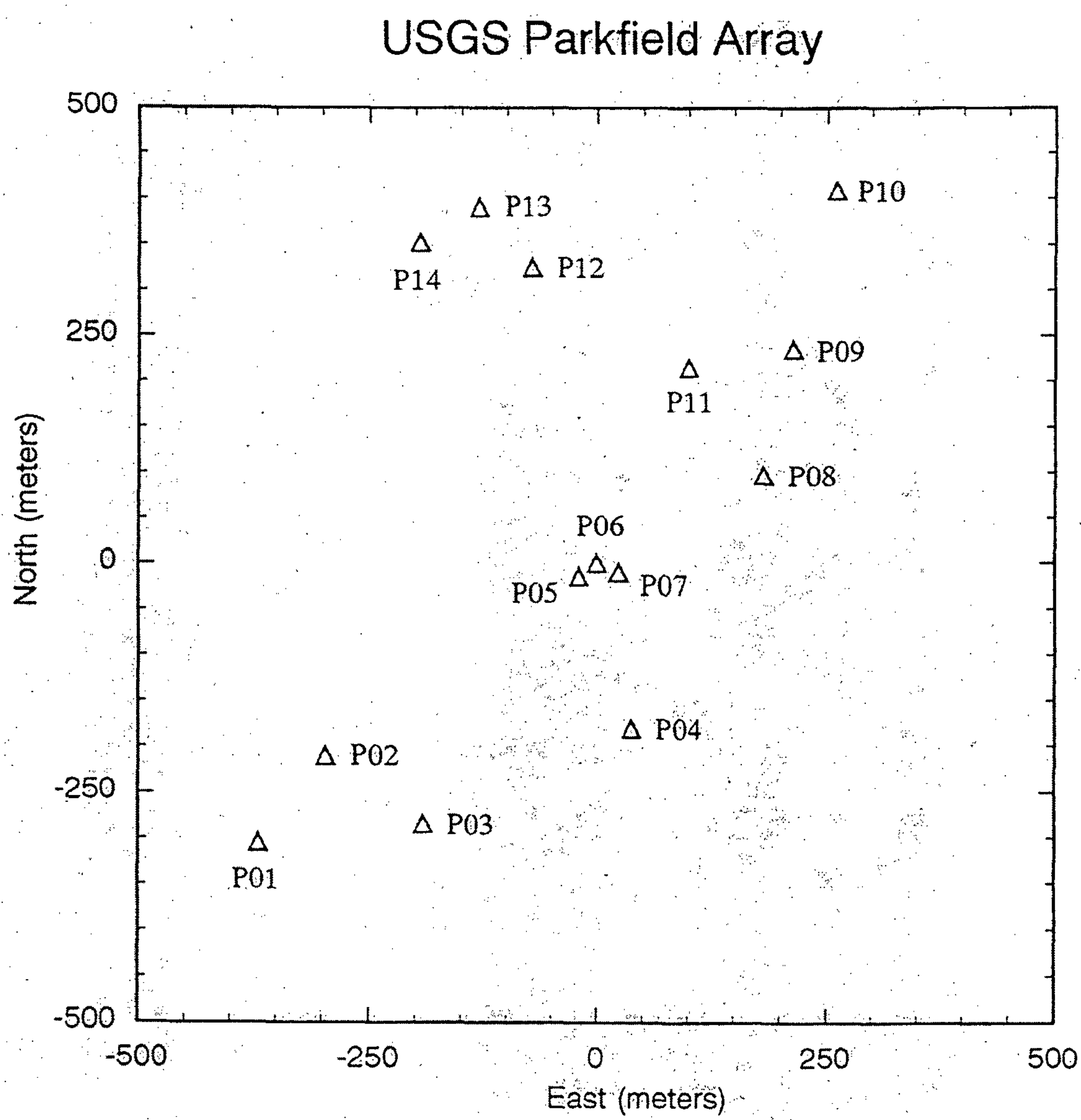

Figure 3-8. Array configuration of the USGS Parkfield array.

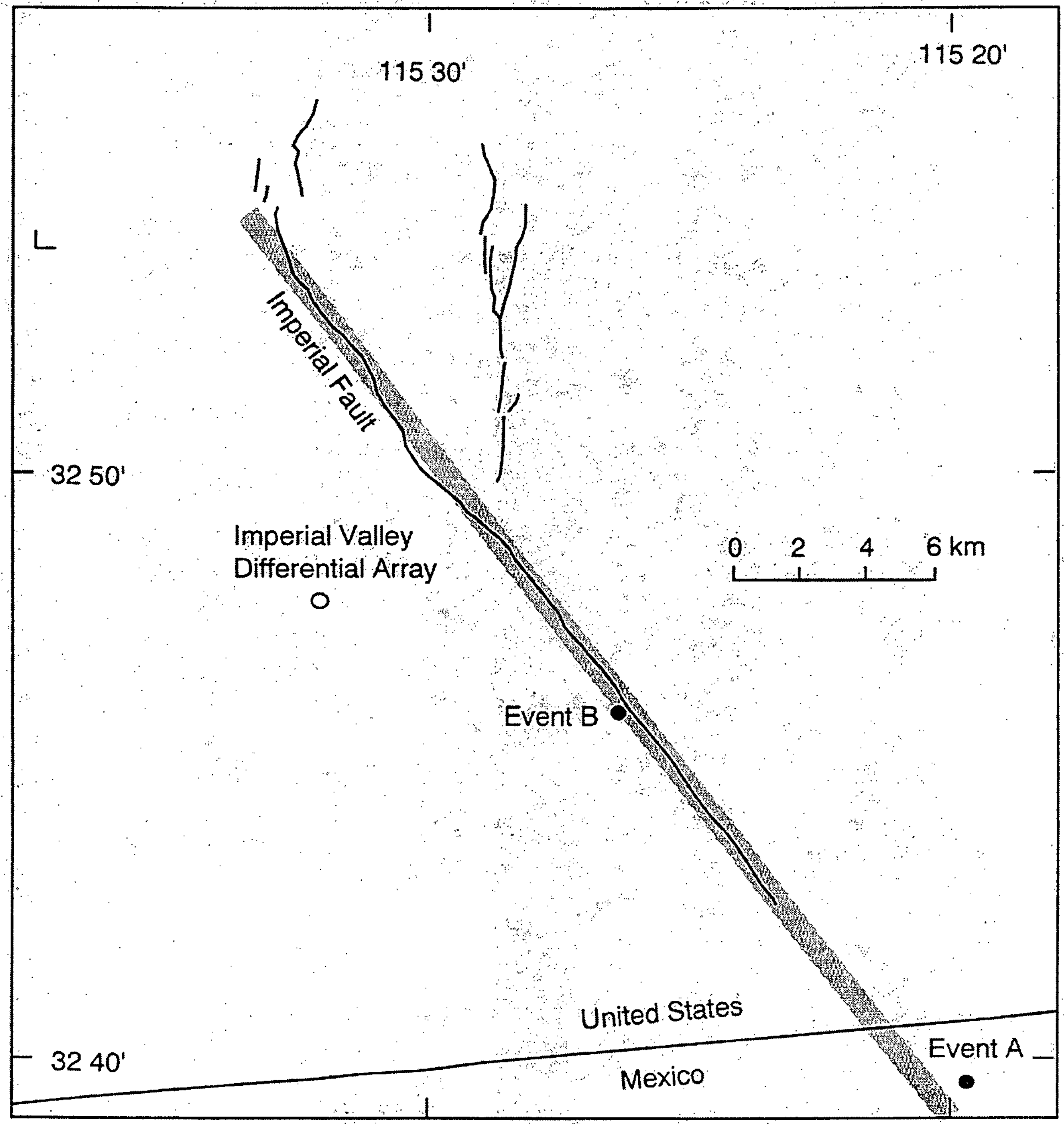

Figure 3-9. Location of the Imperial Valley Differential array and epicenters of recorded events.

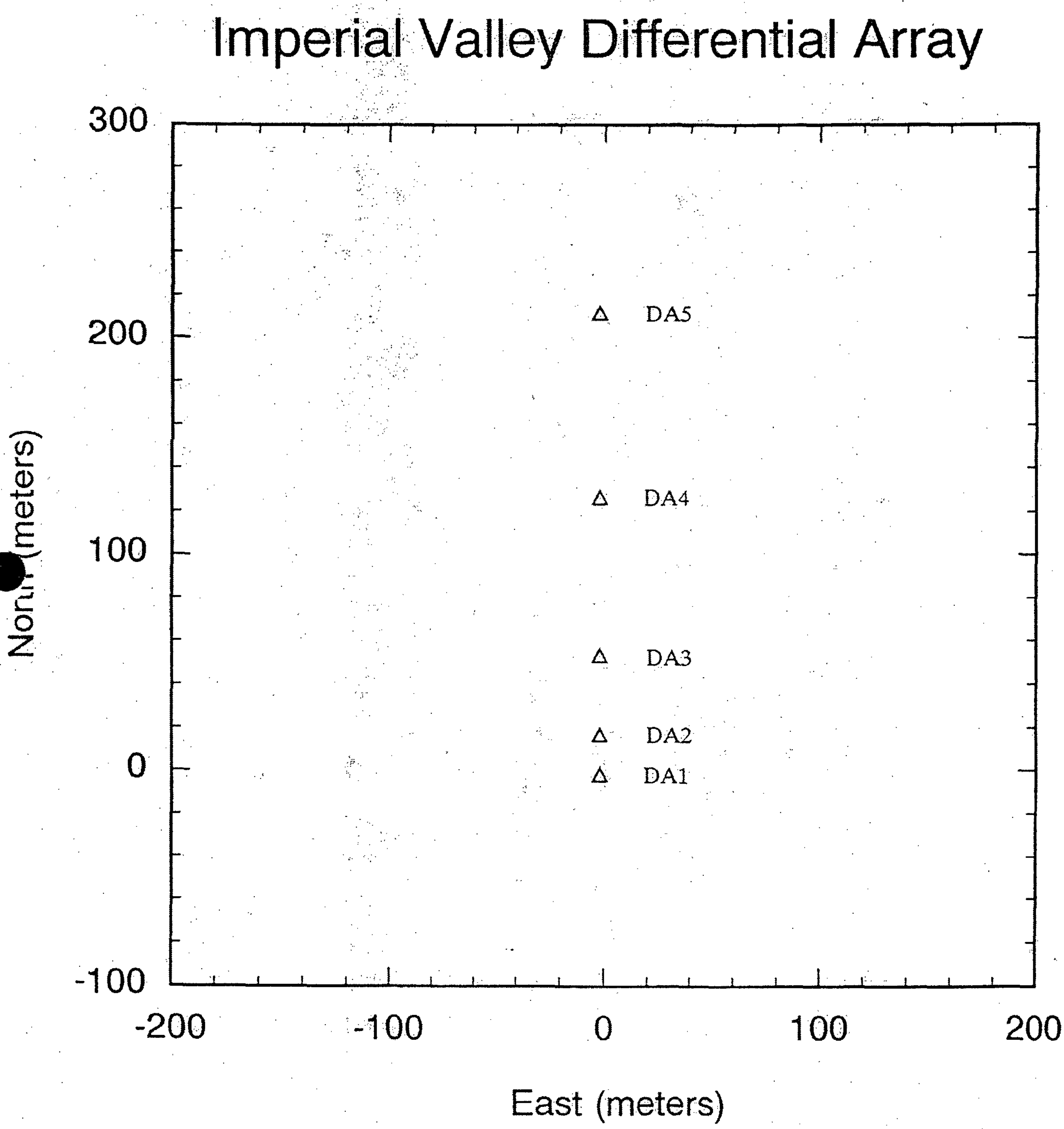

Figure 3-10. Array configuration of the Imperial Valley Differential array.

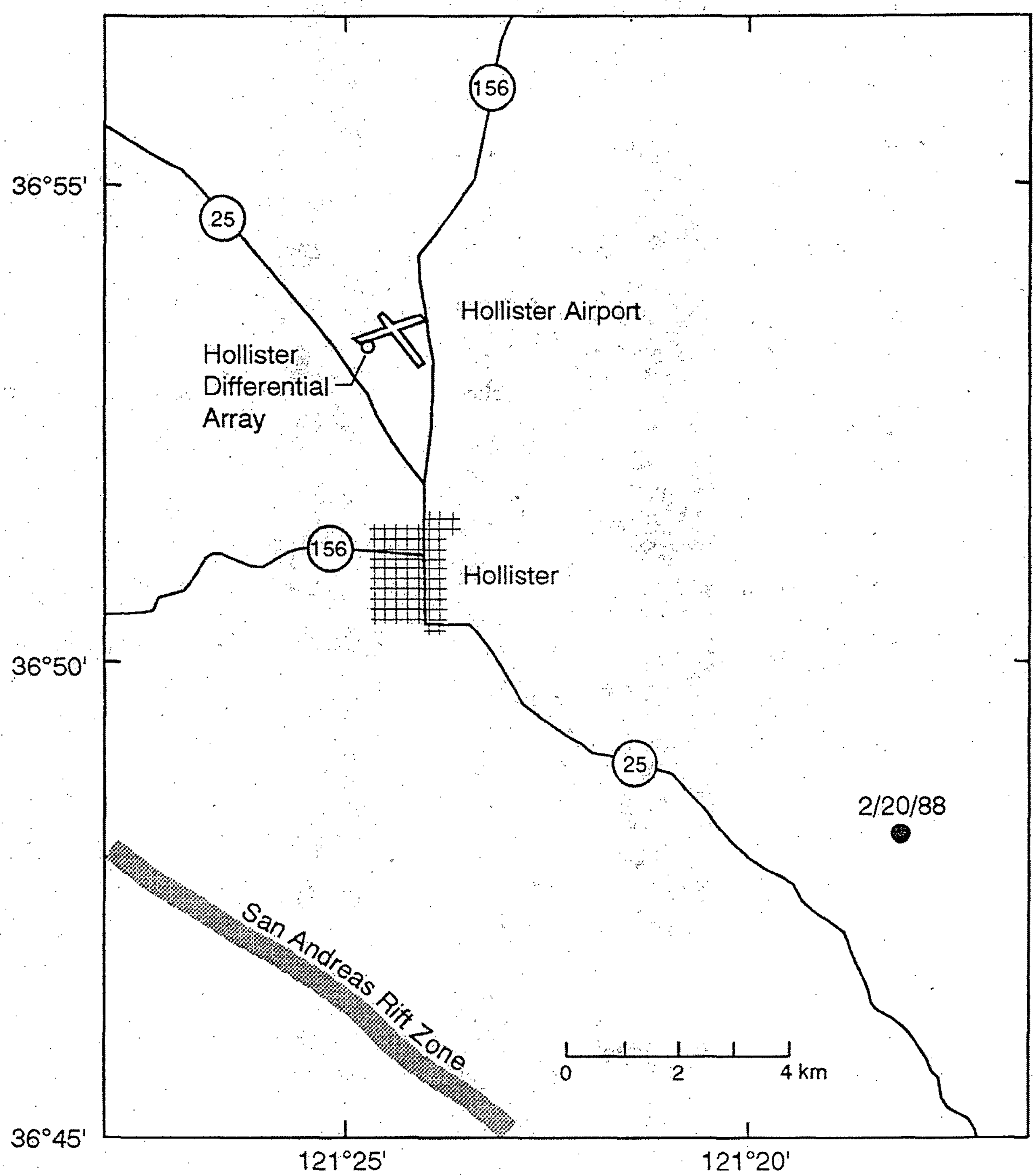

Figure 3-11. Location of the Hollister Differential array and epicenters of recorded events.

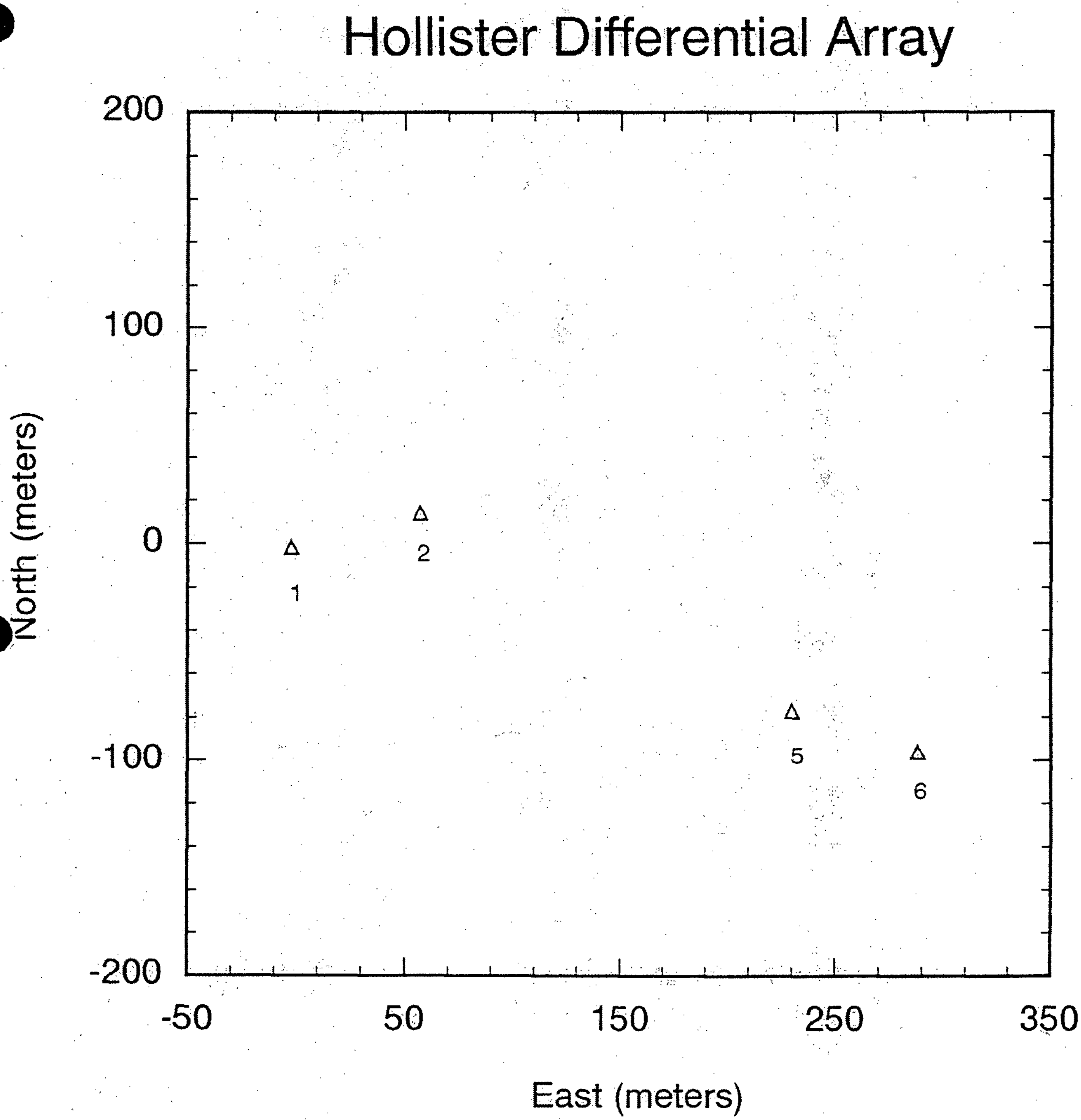

Figure 3-12. Array configuration of the Hollister Differential array.

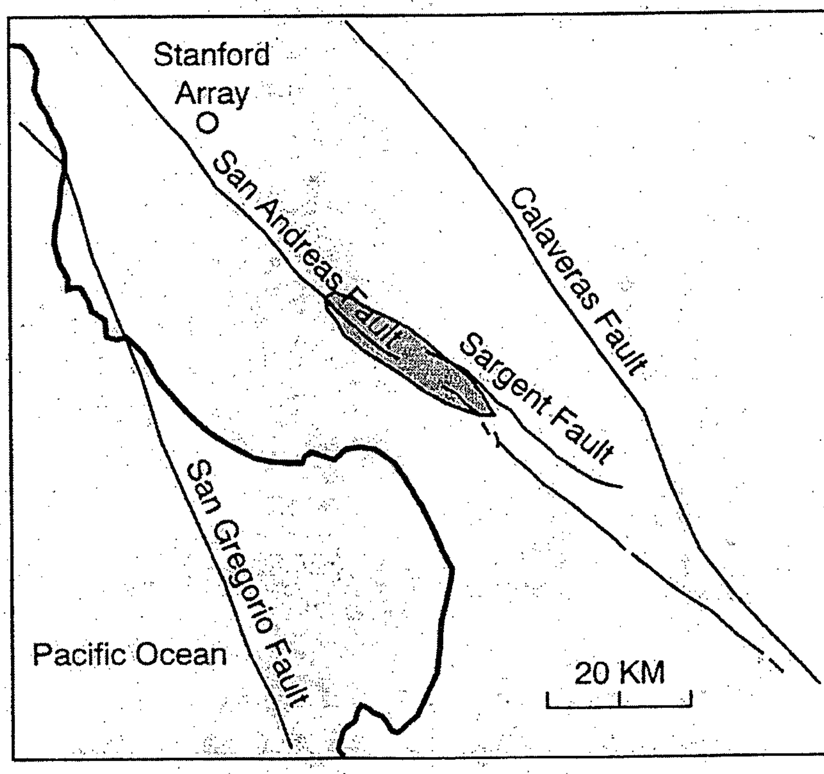

Figure 3-13. Location of the Stanford temporary array. Epicenters of recorded events are not available at this time, but they are aftershocks of the Loma Prieta earthquake.

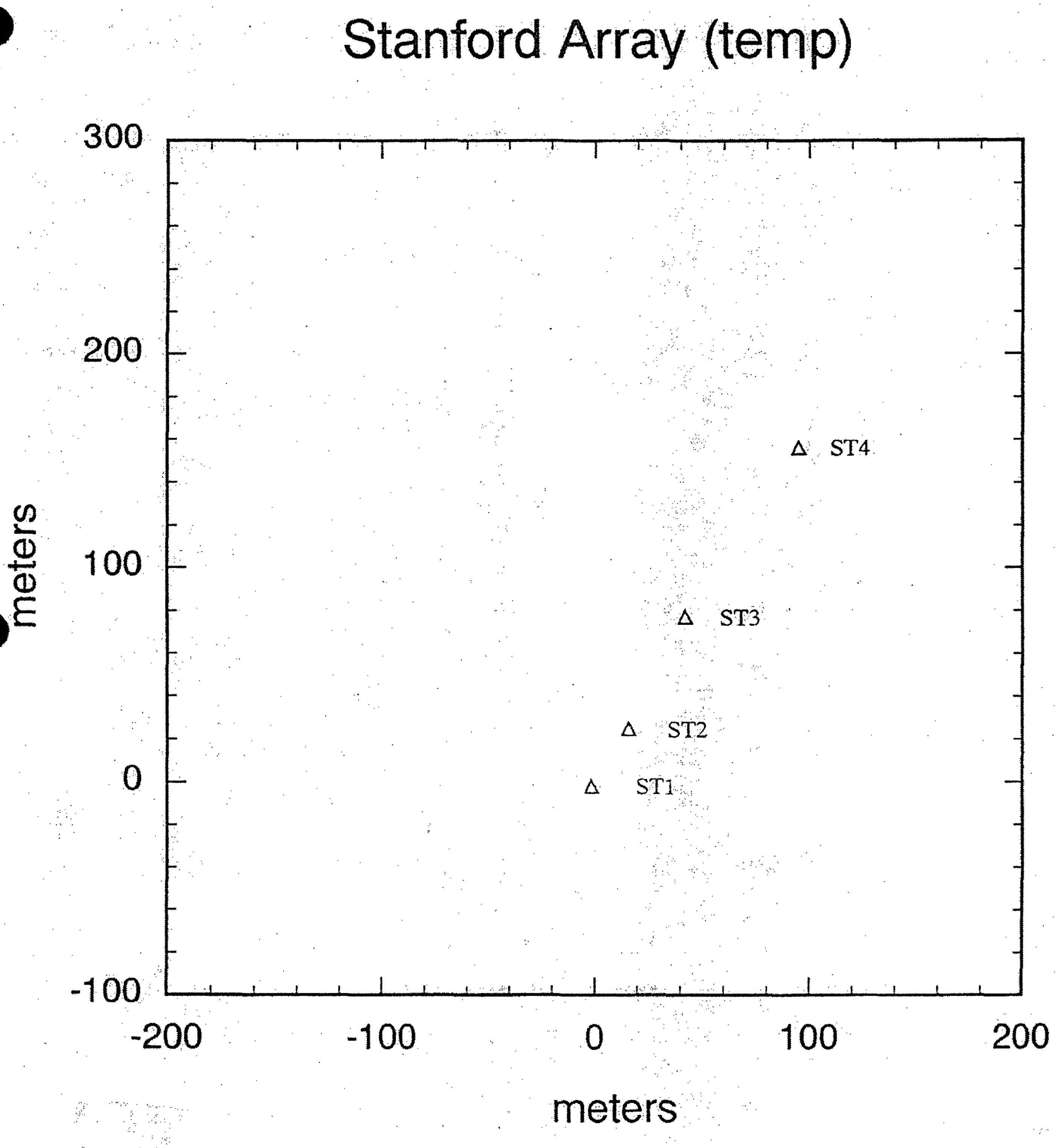

Figure 3-14. Array configuration of the Stanford temporary array.

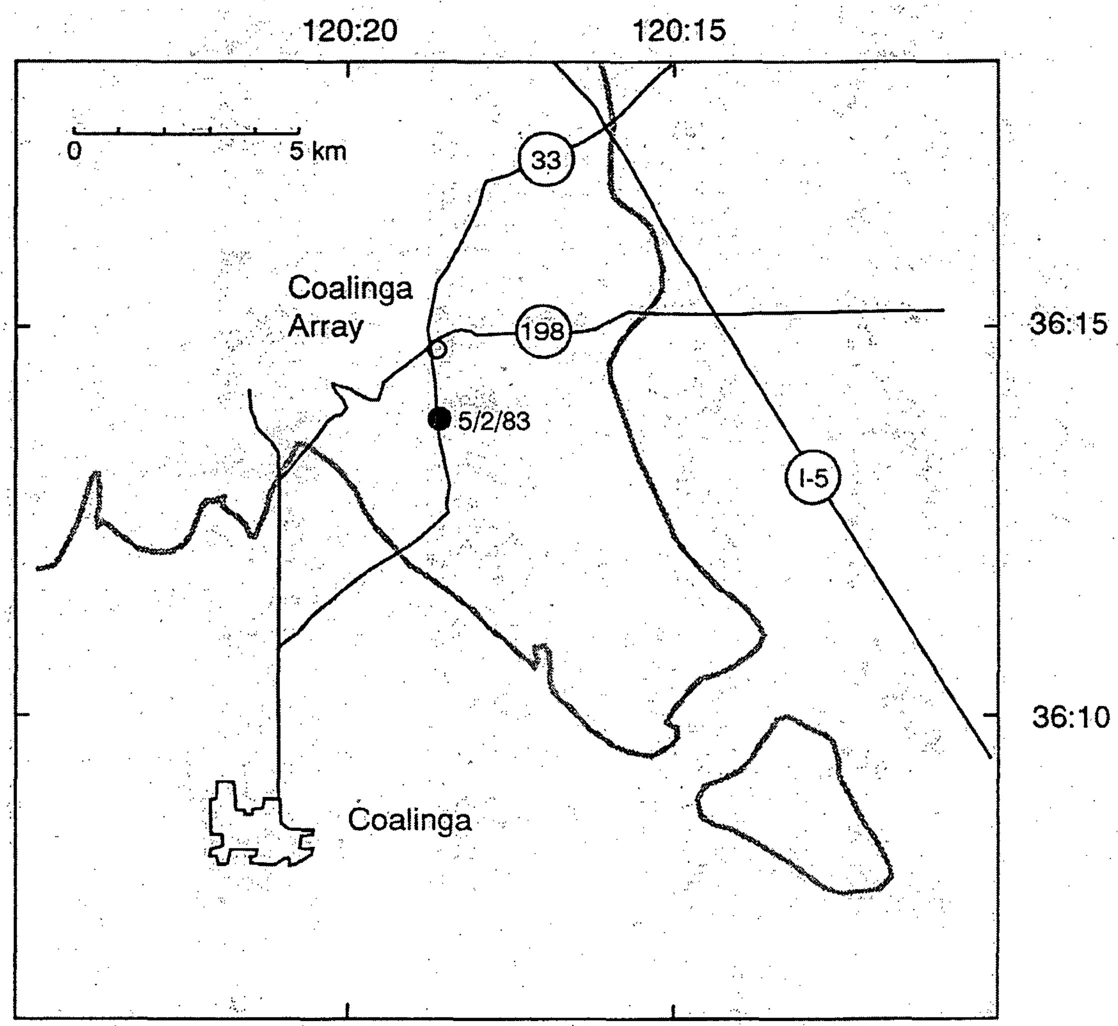

Figure 3-15. Location of the Coalinga temporary array and epicenters of recorded events.

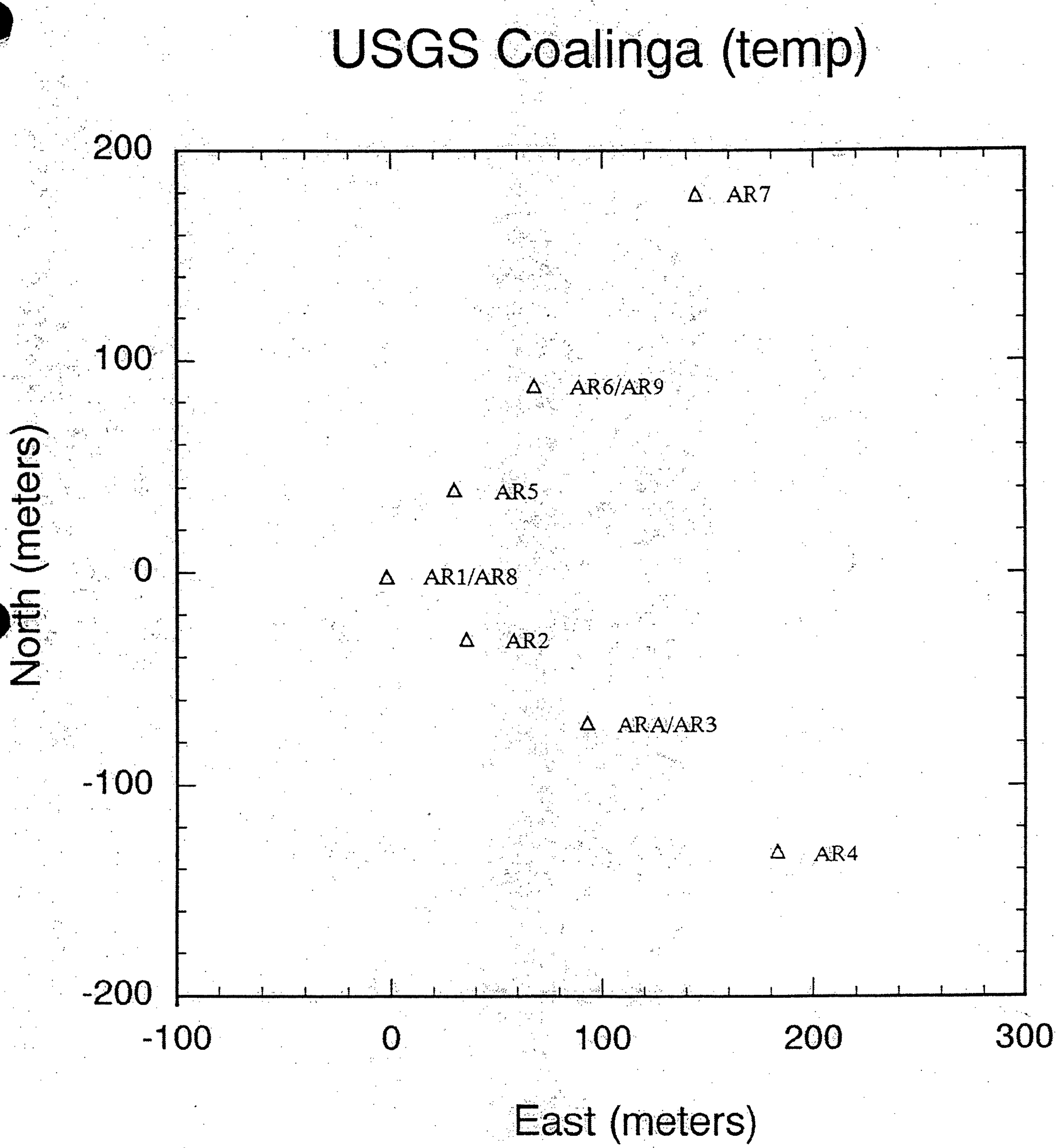

Figure 3-16. Array configuration of the Coalinga temporary array.

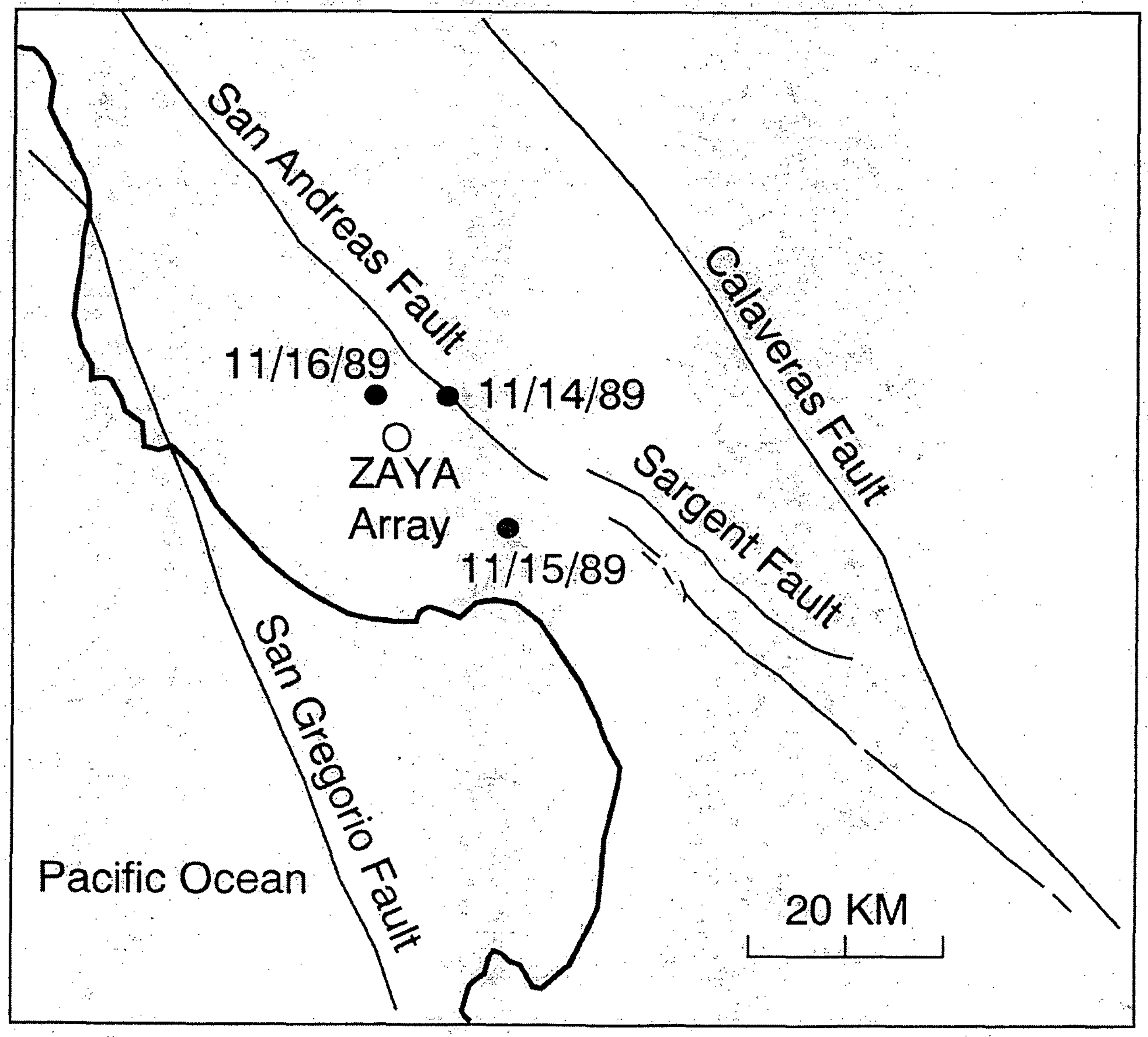

Figure 3-17. Location of the UCSC ZAYA temporary array and epicenters of recorded events.

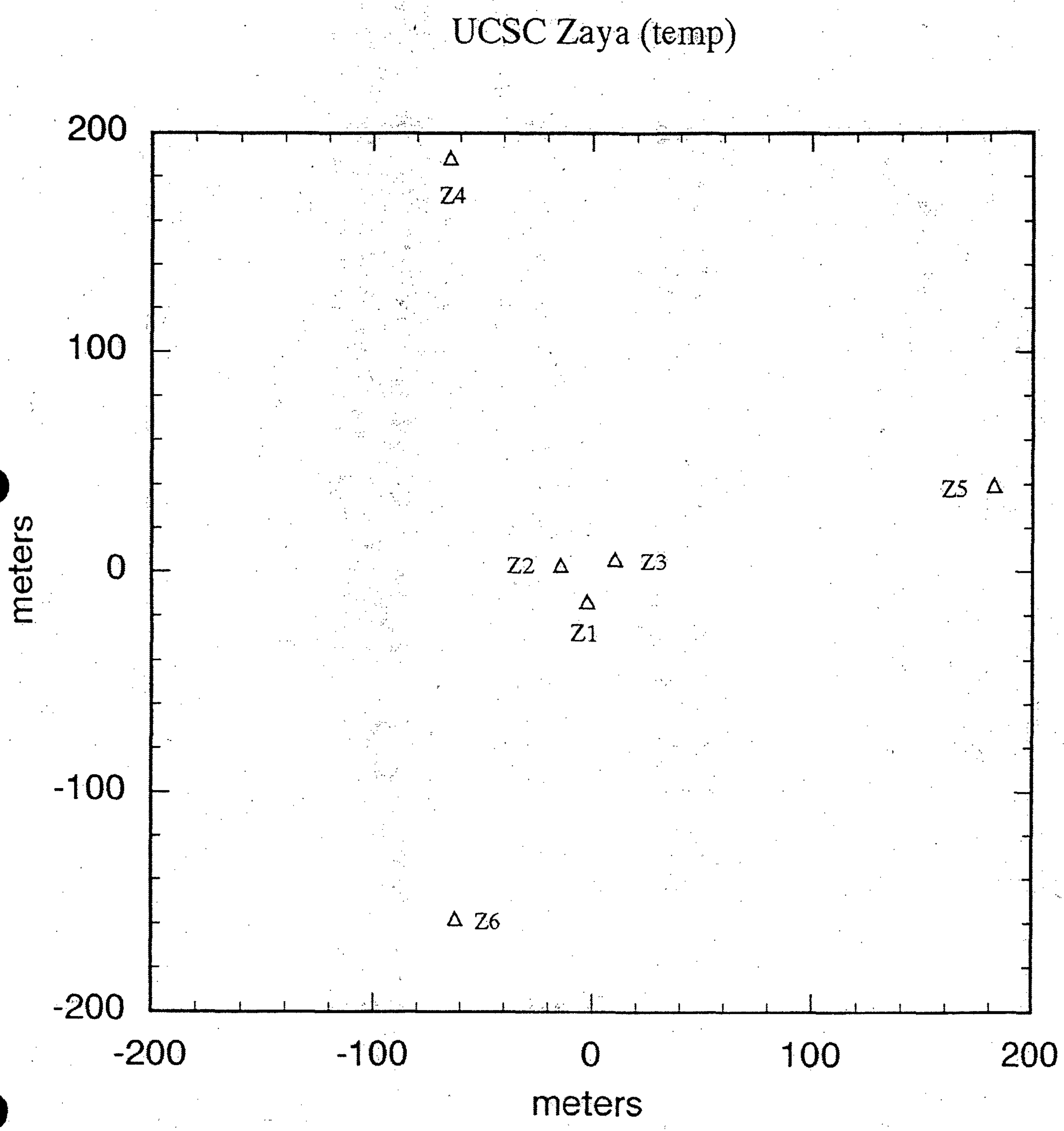

Figure 3-18. Array configuration of the UCSC ZAYA temporary array.

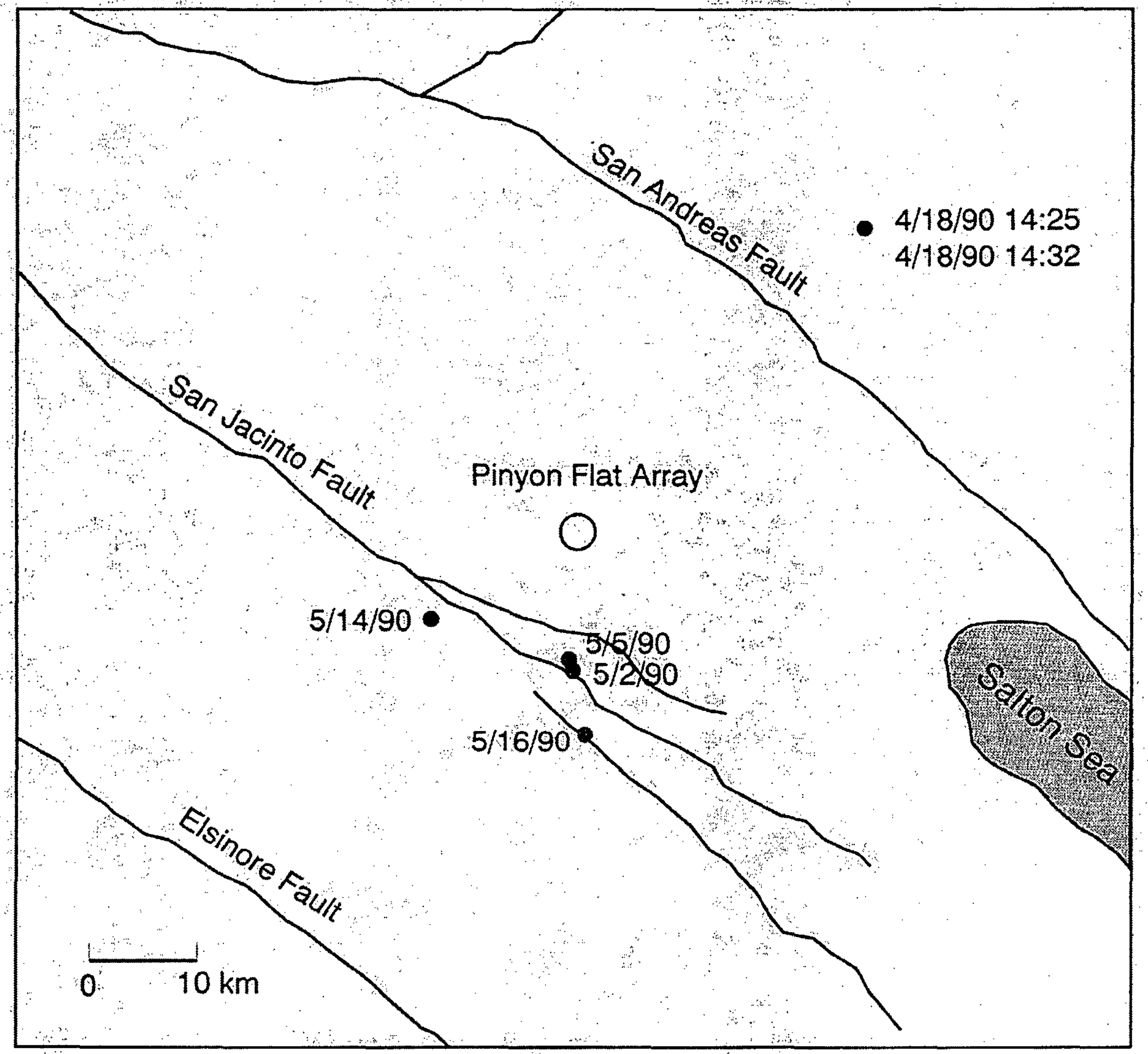

Figure 3-19. Location of the Pinyon Flat temporary array and epicenters of recorded events.

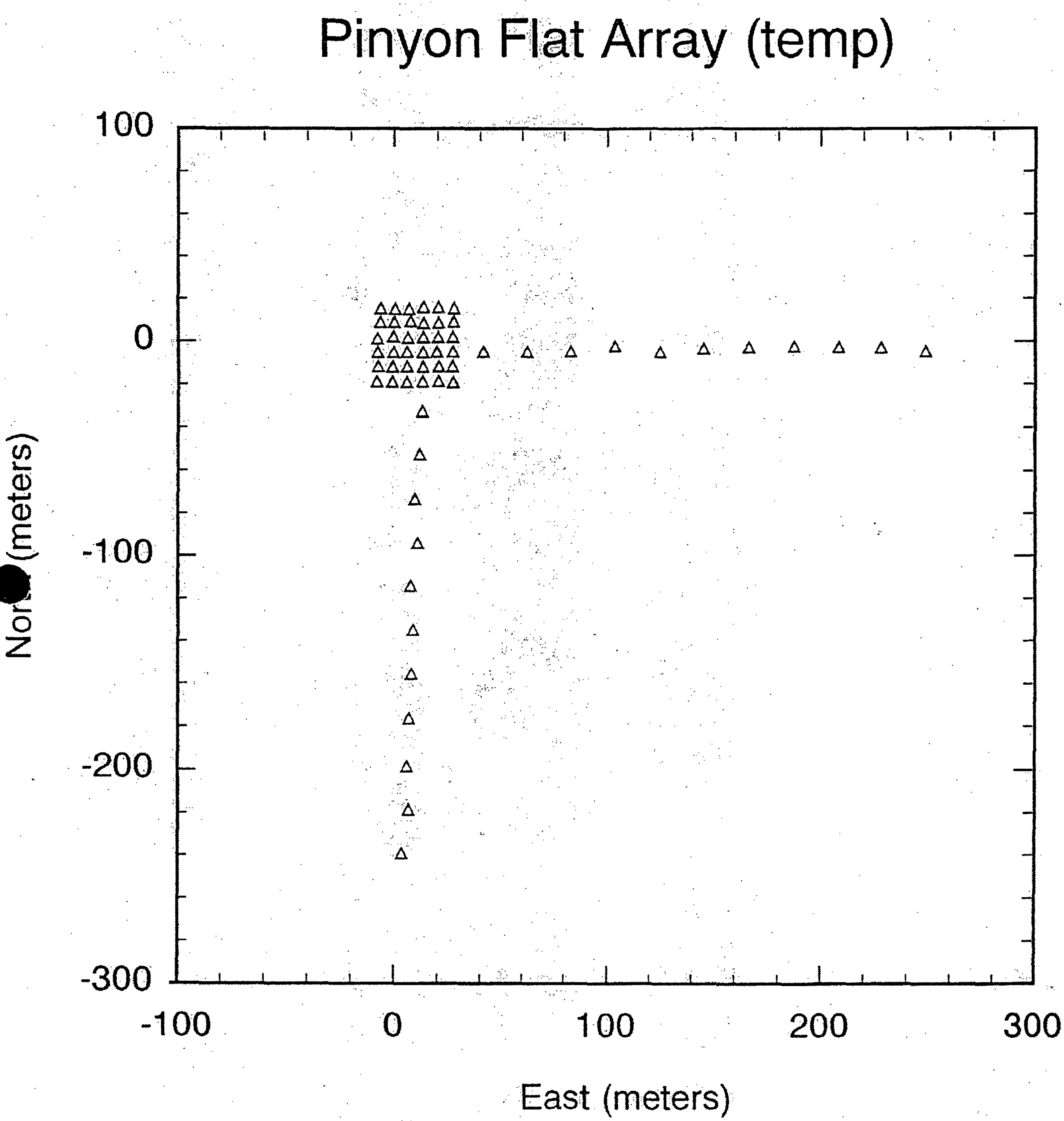

Figure 3-20. Array configuration of the Pinyon Flat temporary array.

4

SITE DEPENDENCE OF COHERENCY

LSST Coherency Function

Abrahamson et al. (1991, 1992) developed a functional relation for the observed coherency for the Lotung LSST strong motion data set. The relation given for lagged coherency is as follows:

$$\tanh^{-1}|\gamma(f,\xi)| = (2.54 - 0.012\xi)\,[\exp\{(-0.115 - 0.00084\xi)f\} + \tfrac{1}{3}f^{-0.878}] + 0.35, \qquad (4\text{-}1)$$

where ξ and f represent station separation and frequency, respectively. This relation is applicable to separation distance of 5-100 m and frequencies of 0.5 to 25 Hz. In the following analysis, we use these functions to compare lagged coherency observed at Lotung to observations from other sites. Functional relations for other attributes of the coherency model (as expressed by real or complex parts of the γ function) were also developed for the Lotung data set, but will not be discussed here.

The unusually wide distribution of earthquake magnitudes and distances available from Lotung (Table 3-3) permitted expression of standard errors as a combination of intra-event (between stations for a given station) and inter-event (between events for a given station) spatial variation. Direct comparison of intra- and inter-event variation yielded comparable errors (each about 0.26 $\tanh^{-1}$ units). Moreover, the residuals of the intra-event coherencies compared to the mean for all events and stations (intra- plus inter-event) showed no significant magnitude or distance bias.

Coherencies from Other Sites

The coherencies computed for the horizontal component S-wave window are shown for each array in Figures 4-1 to 4-9. Each plot shows the coherencies for all of the events considered for each array. These figures show the individual coherency values except for the Chiba and Pinyon Flat arrays. There are too many coherency values from these two arrays and so the mean coherency and plus or minus one standard error are shown instead.

An important feature to note is that the coherencies values have a great deal of scatter. This indicates that many repeated estimates of coherency are needed to get stable results. Since the individual coherency values are highly uncertain, it is important not to over-interpret observed variations in coherency from just a few events and/or station pairs.

The coherency function from the Lotung LSST array data is shown in these figures for reference. The solid curves show the mean coherency for the upper and lower end of the distance range in each plot. The dashed curves show plus an minus one standard error from the upper and lower curves, respectively.

The average coherencies for the four soil arrays are compared to the LSST lagged coherency functions in Figures 4-10 to 4-13 for separation distances of 5-15 m, 15-30 m, 30-60 m, and 60-100 m. The scatter of the soil site coherencies is comparable to the scatter found at the LSST array, indicated by the dashed lines. The coherencies from the four soil arrays are not significantly different from the LSST coherency function indicating that the LSST coherency function can be used as a generic coherency function for soil sites.

The average coherencies for the five rock site arrays are similarly compared to the LSST array coherency function in Figures 4-14 to 4-17. The coherencies from the EPRI Parkfield and Pinyon Flat arrays are compatible with the LSST coherency function but the coherencies from the USGS Parkfield and ZAYA arrays are much lower than the LSST coherency function. One explanation may be that the USGS Parkfield data are strongly affected by significant topographic variations (Fletcher et al., 1991) which could reduce the coherency, but that is not the case for the ZAYA array (Bonamassa et al., 1991). Somerville et al. (1988) found that coherency measured from synthetic seismograms generated from wave propagation in a complex crustal structure has very low coherency where energy is strongly focused from a variety of ray paths. Similar effects are to be expected in the near surface as well. These results suggest that geologic complexity, particularly for rock sites, can have a controlling influence on the site component of coherency.

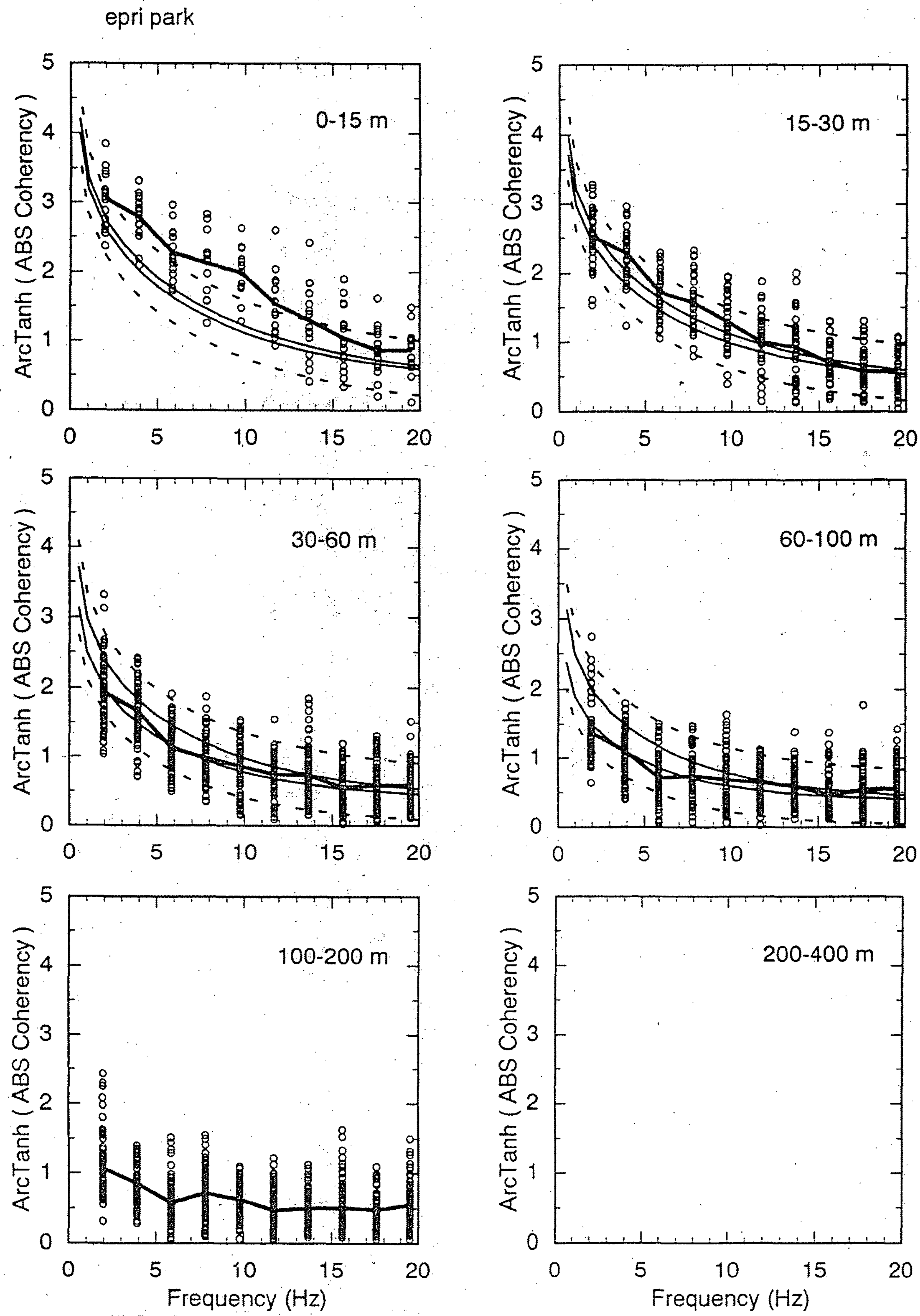

Figure 4-1. Computed coherency from the EPRI Parkfield array. The thick curve shows the mean coherency and the thin curves show the LSST coherency functions (see text).

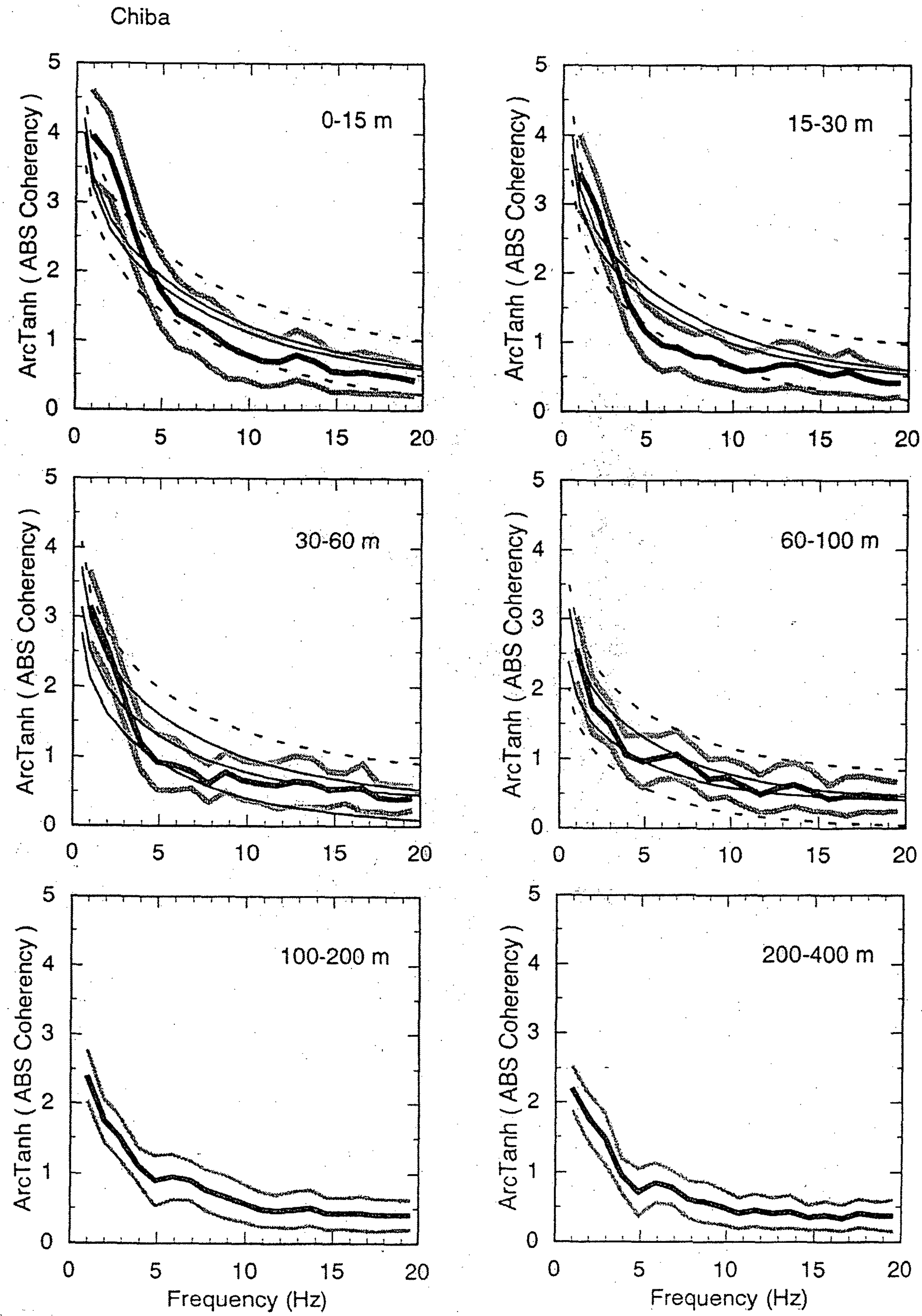

Figure 4-2. Computed coherency from the Chiba array. The thick curve shows the mean coherency and the thin curves show the LSST coherency functions (see text).

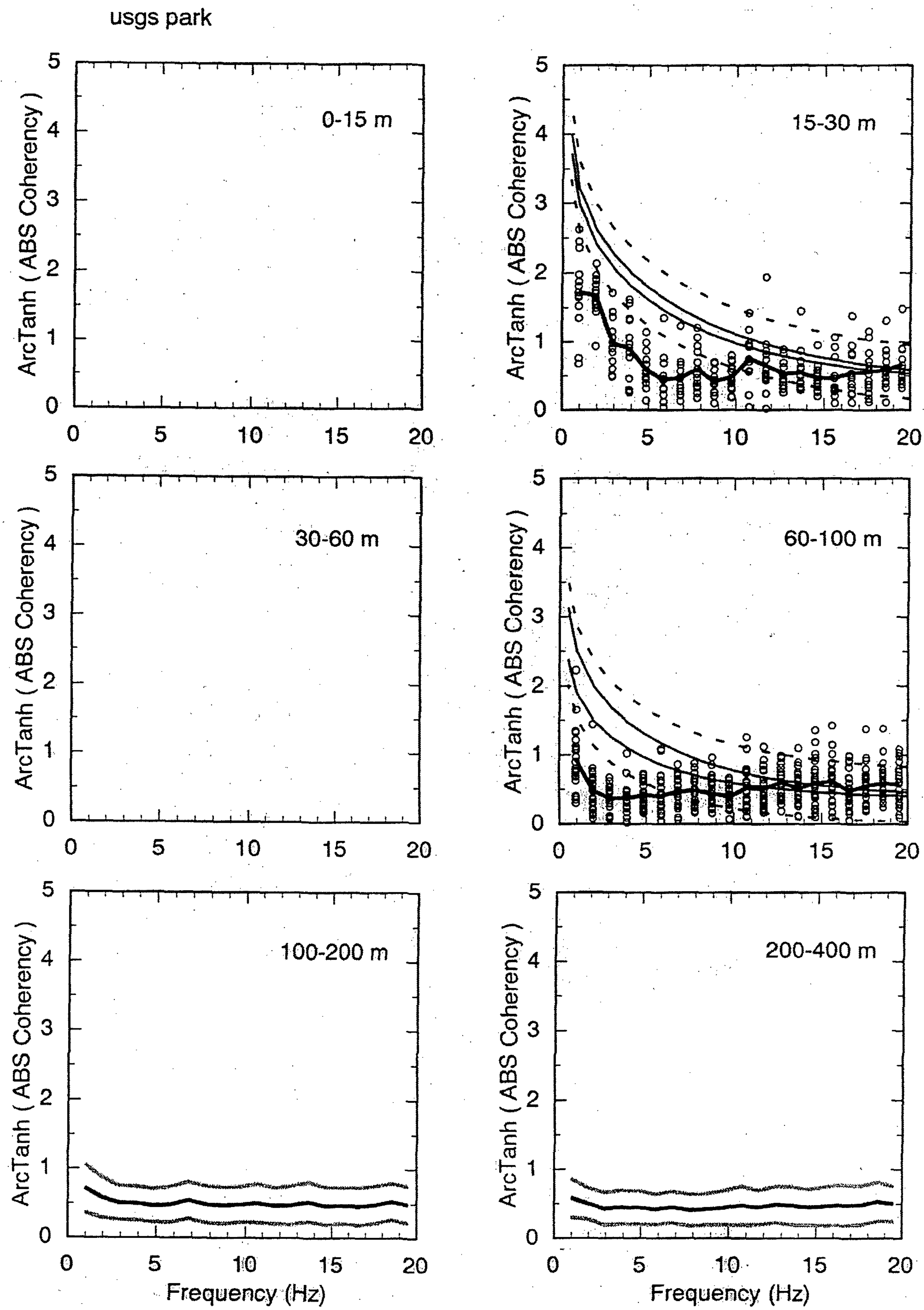

Figure 4-3. Computed coherency from the USGS Parkfield array. The thick curve shows the mean coherency and the thin curves show the LSST coherency functions (see text).

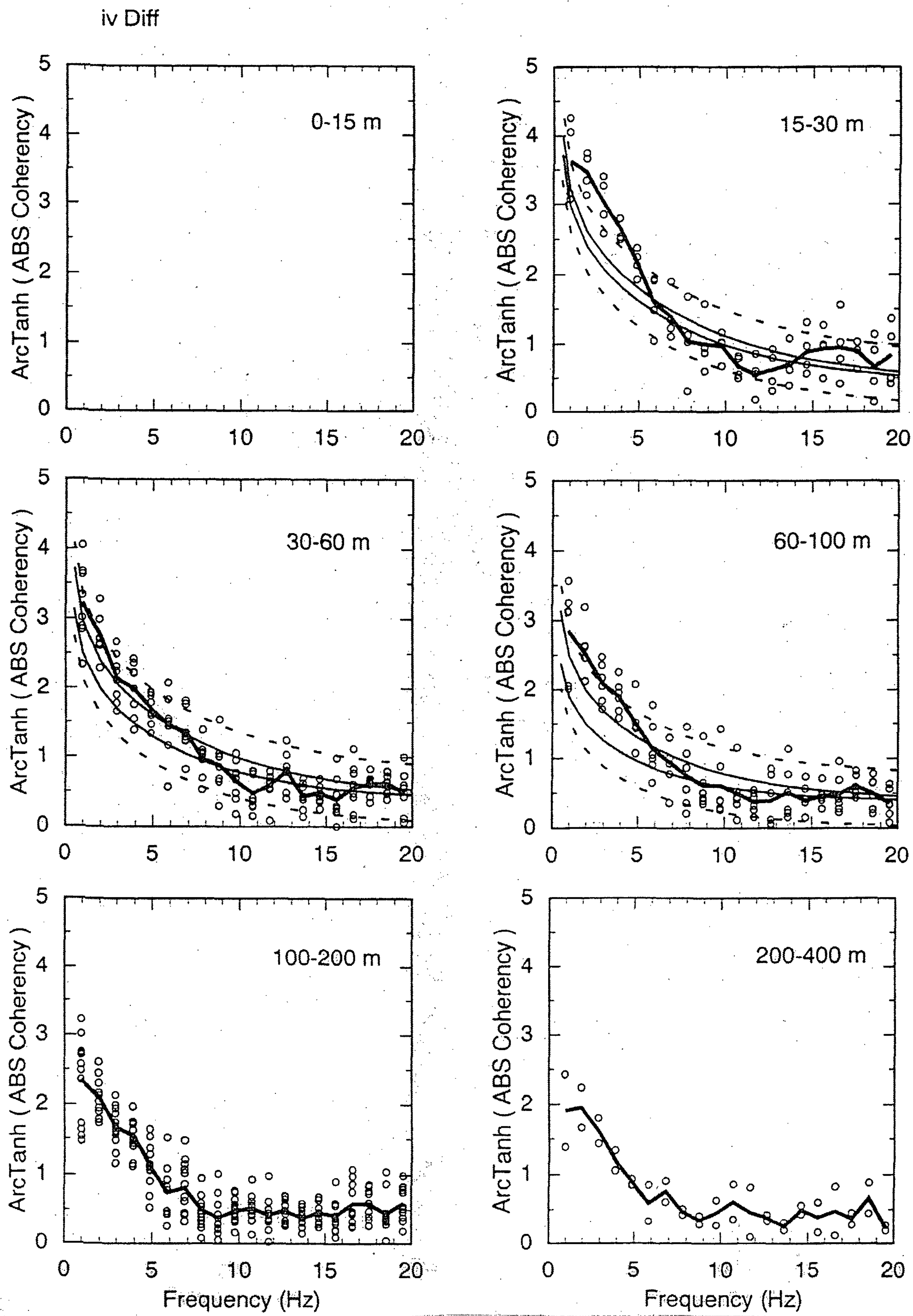

Figure 4-4. Computed coherency from the Imperial Valley Differential array. The thick curve shows the mean coherency and the thin curves show the LSST coherency functions (see text).

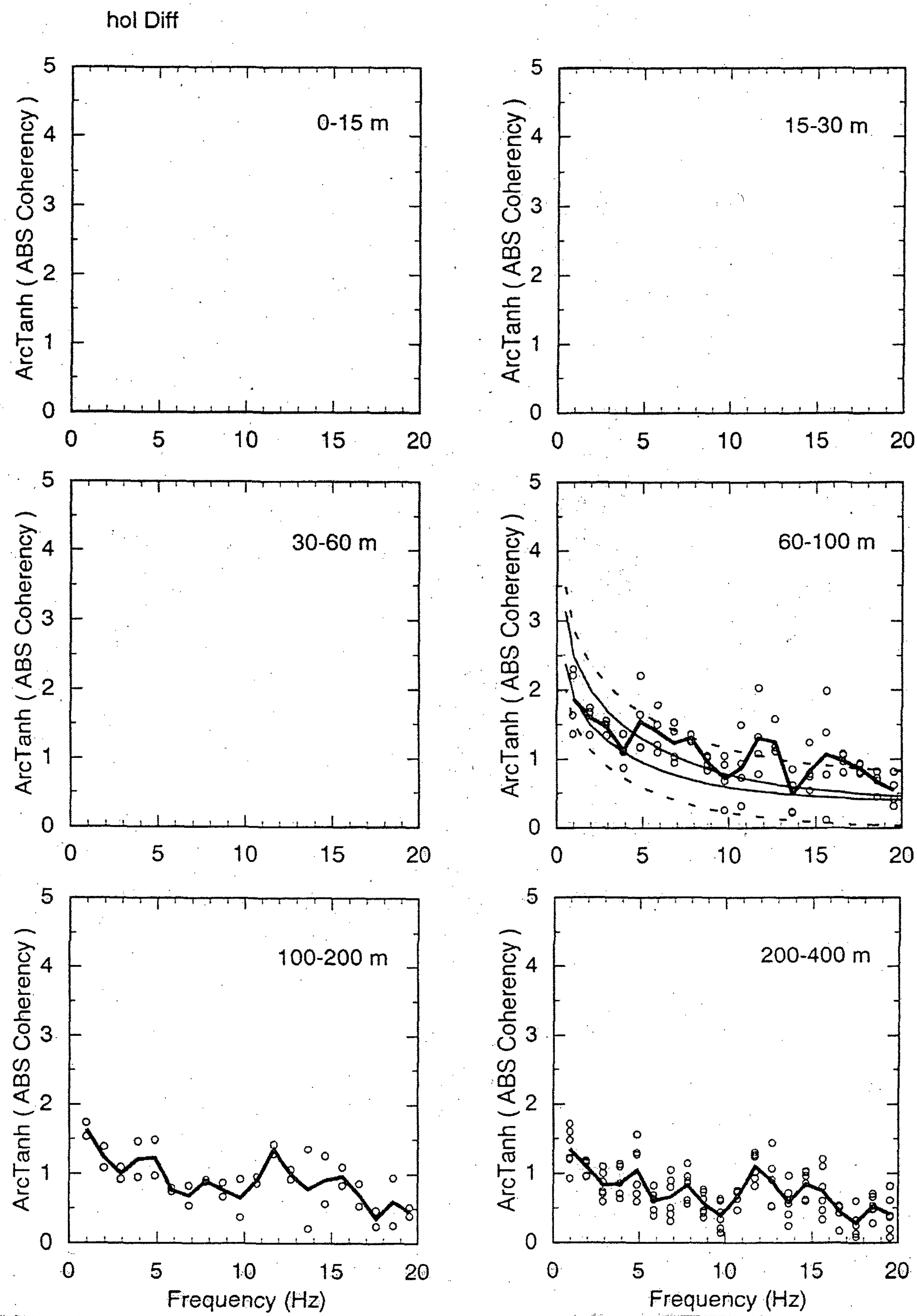

Figure 4-5. Computed coherency from the Holister Differential array. The thick curve shows the mean coherency and the thin curves show the LSST coherency functions (see text).

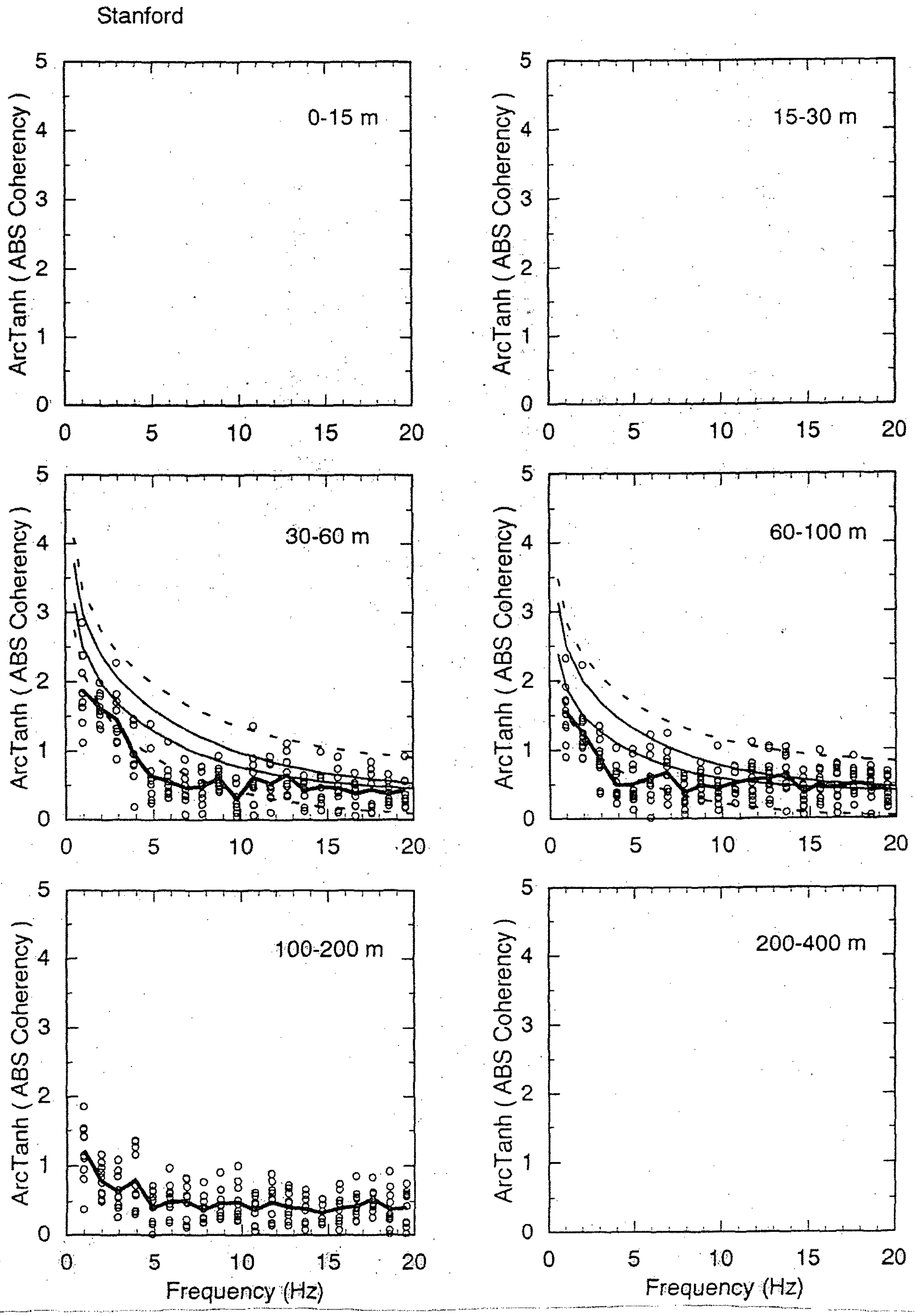

Figure 4-6. Computed coherency from the Stanford temporary array. The thick curve shows the mean coherency and the thin curves show the LSST coherency functions (see text).

Coalinga

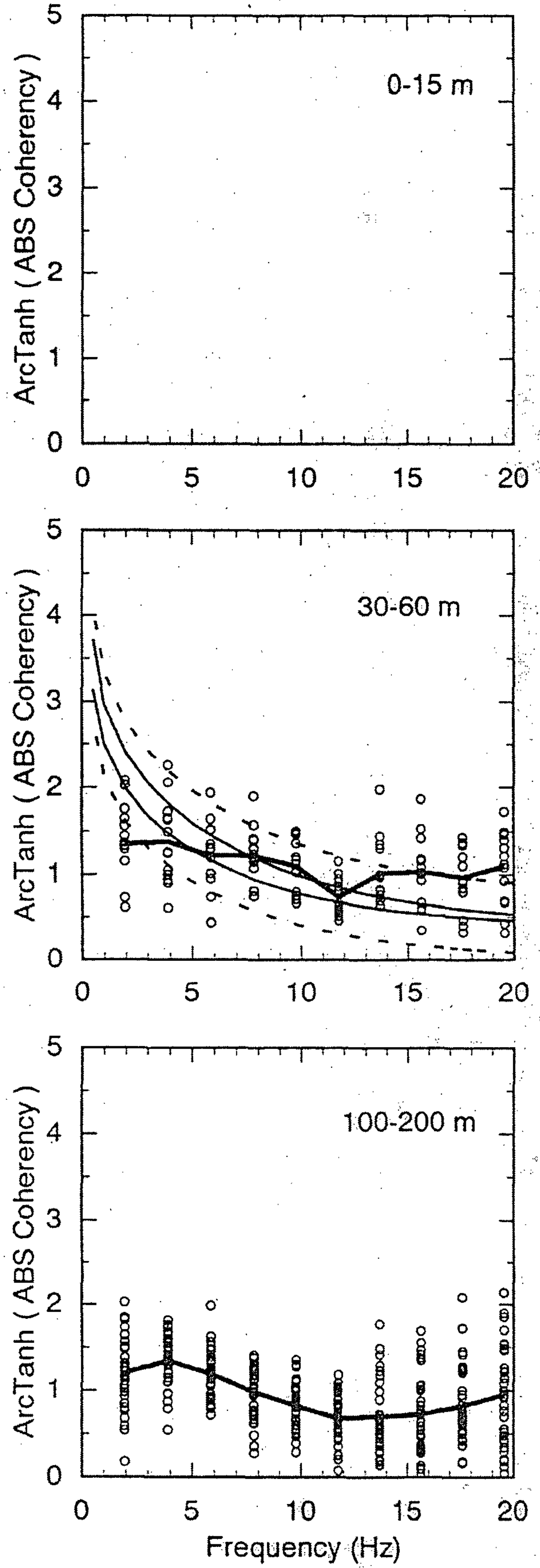

Figure 4-7. Computed coherency from the Coalinga temporary array. The thick curve shows the mean coherency and the thin curves show the LSST coherency functions (see text).

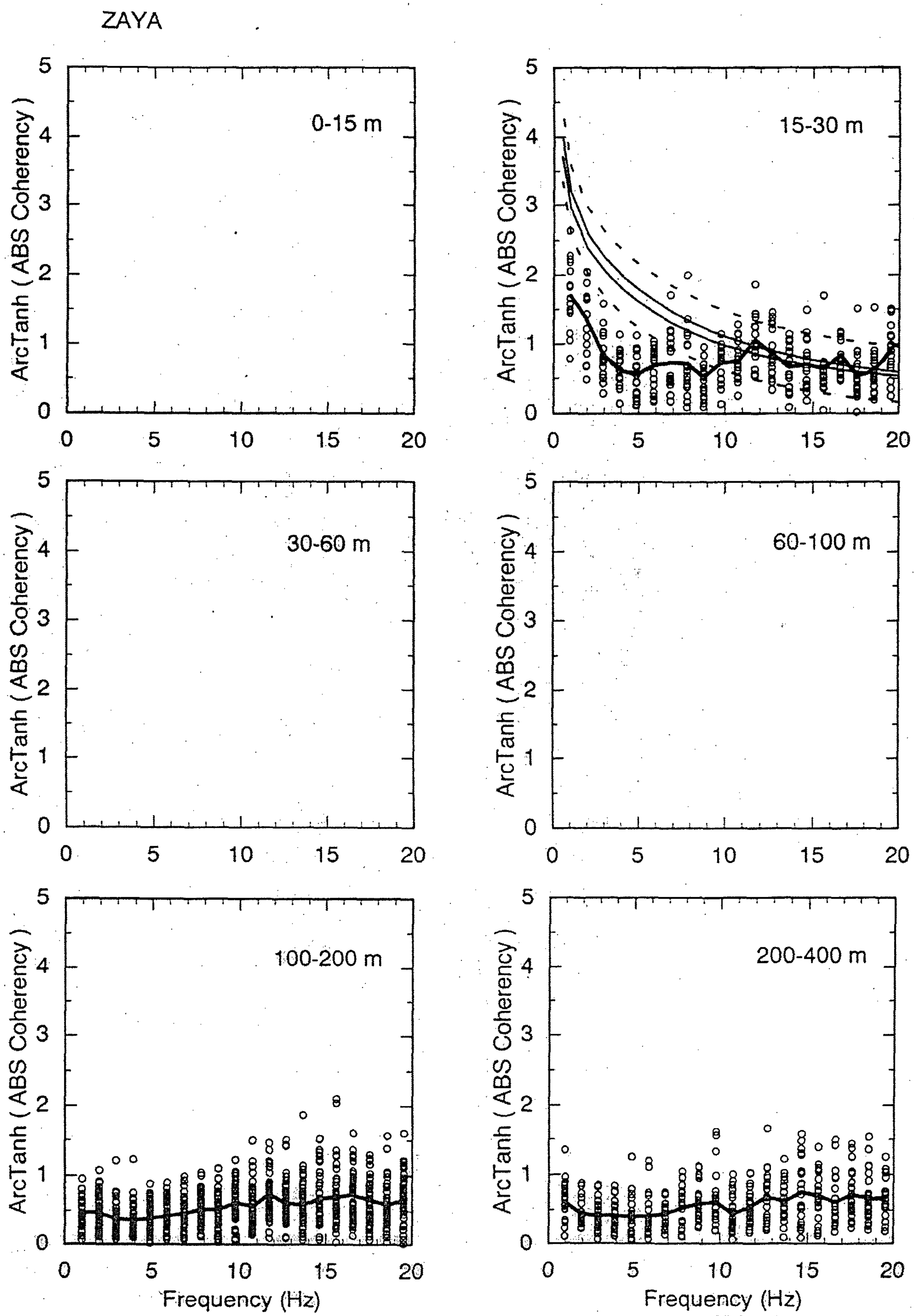

Figure 4-8. Computed coherency from the UCSC ZAYA temporary array. The thick curve shows the mean coherency and the thin curves show the LSST coherency functions (see text).

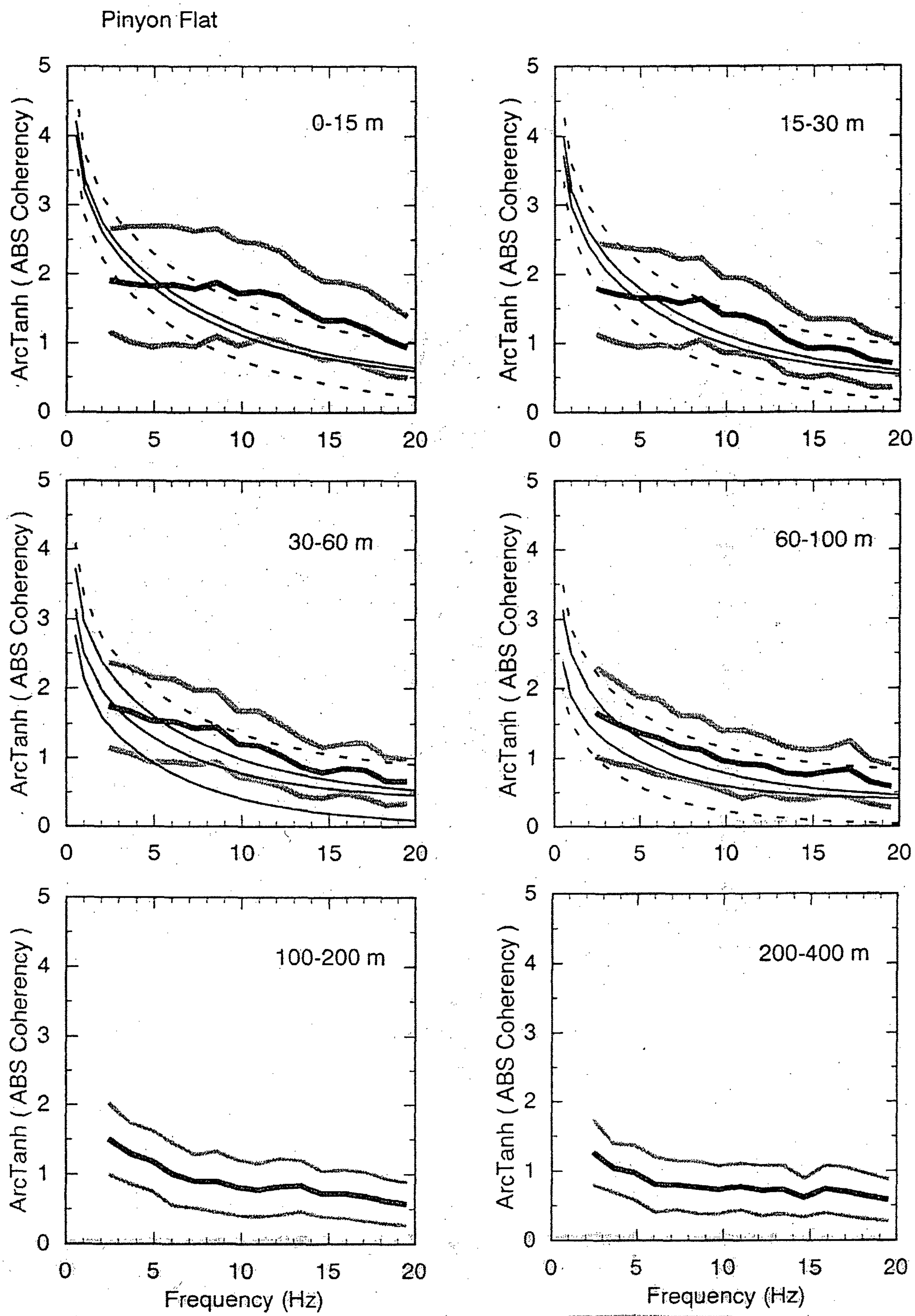

Figure 4-9. Computed coherency from the Pinyon Flat temporary array. The thick curve shows the mean coherency and the thin curves show the LSST coherency functions (see text).

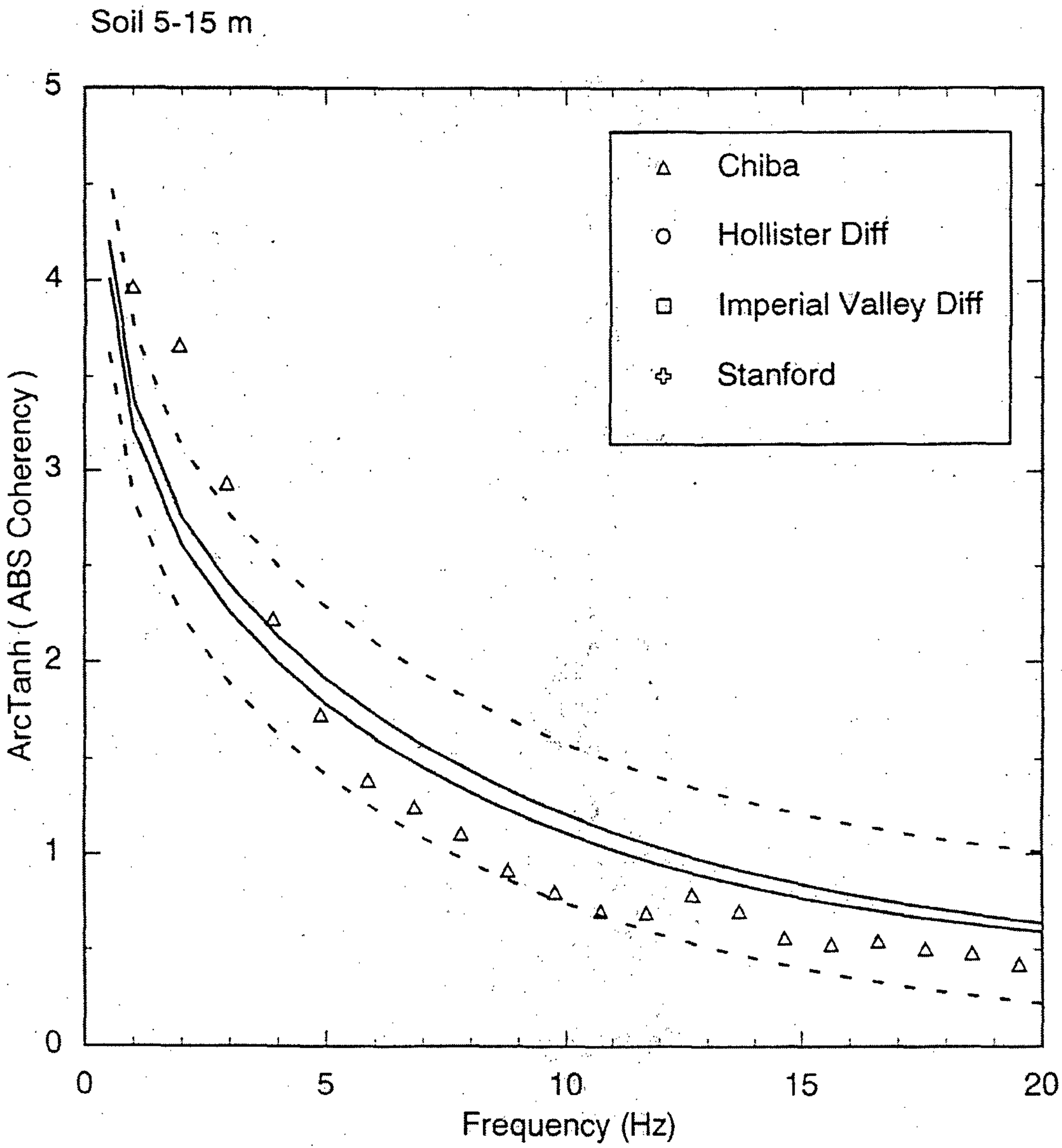

Figure 4-10. Average coherencies from arrays on soil sites for separations distances of 5-15 m. The solid curves show the mean LSST coherency functions for 5 and 15 m. The dashed curves show plus and minus one standard error of the LSST coherency functions.

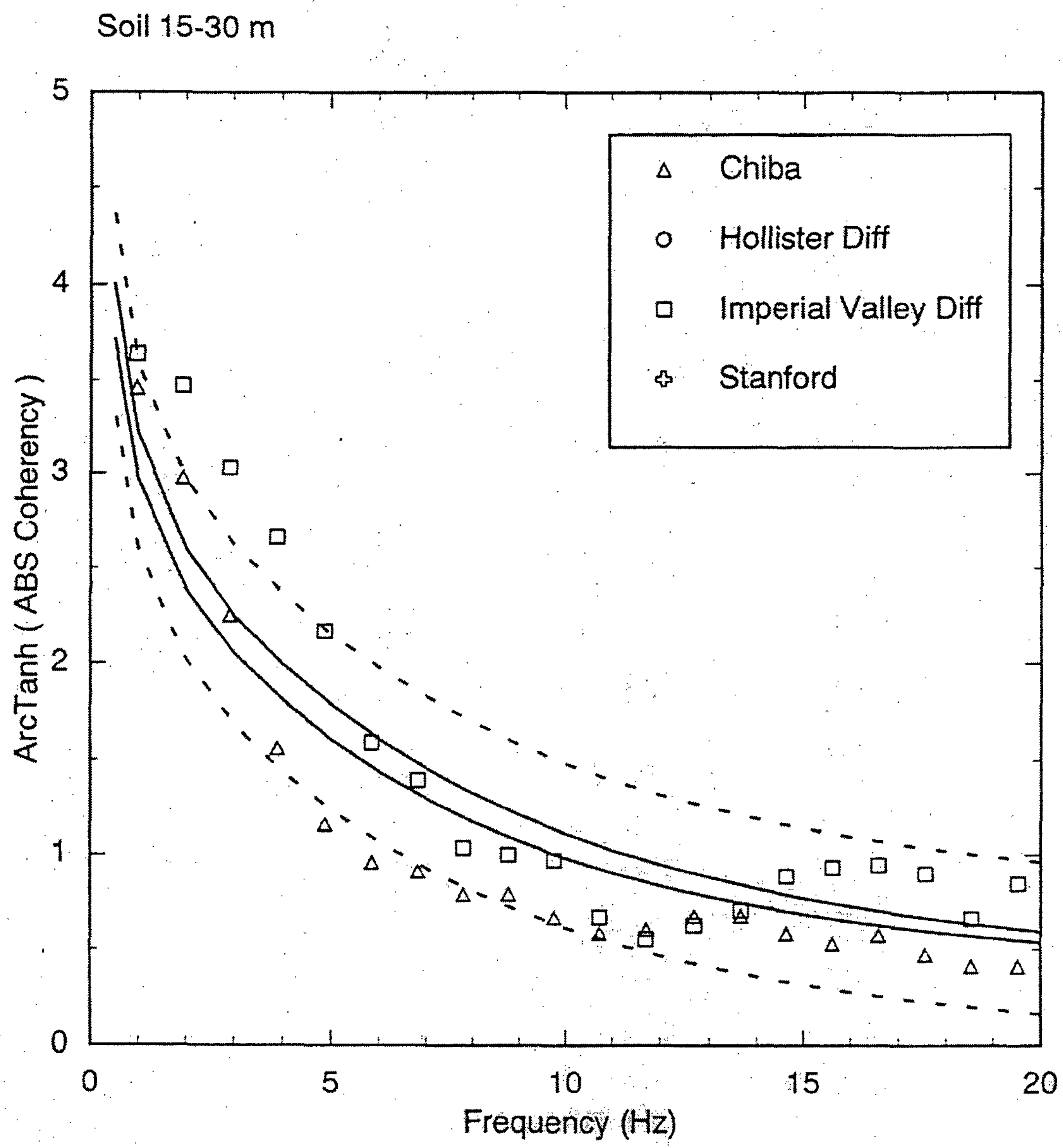

Figure 4-11. Average coherencies from arrays on soil sites for separations distances of 15-30 m. The solid curves show the mean LSST coherency functions for 15 and 30 m. The dashed curves show plus and minus one standard error of the LSST coherency functions.

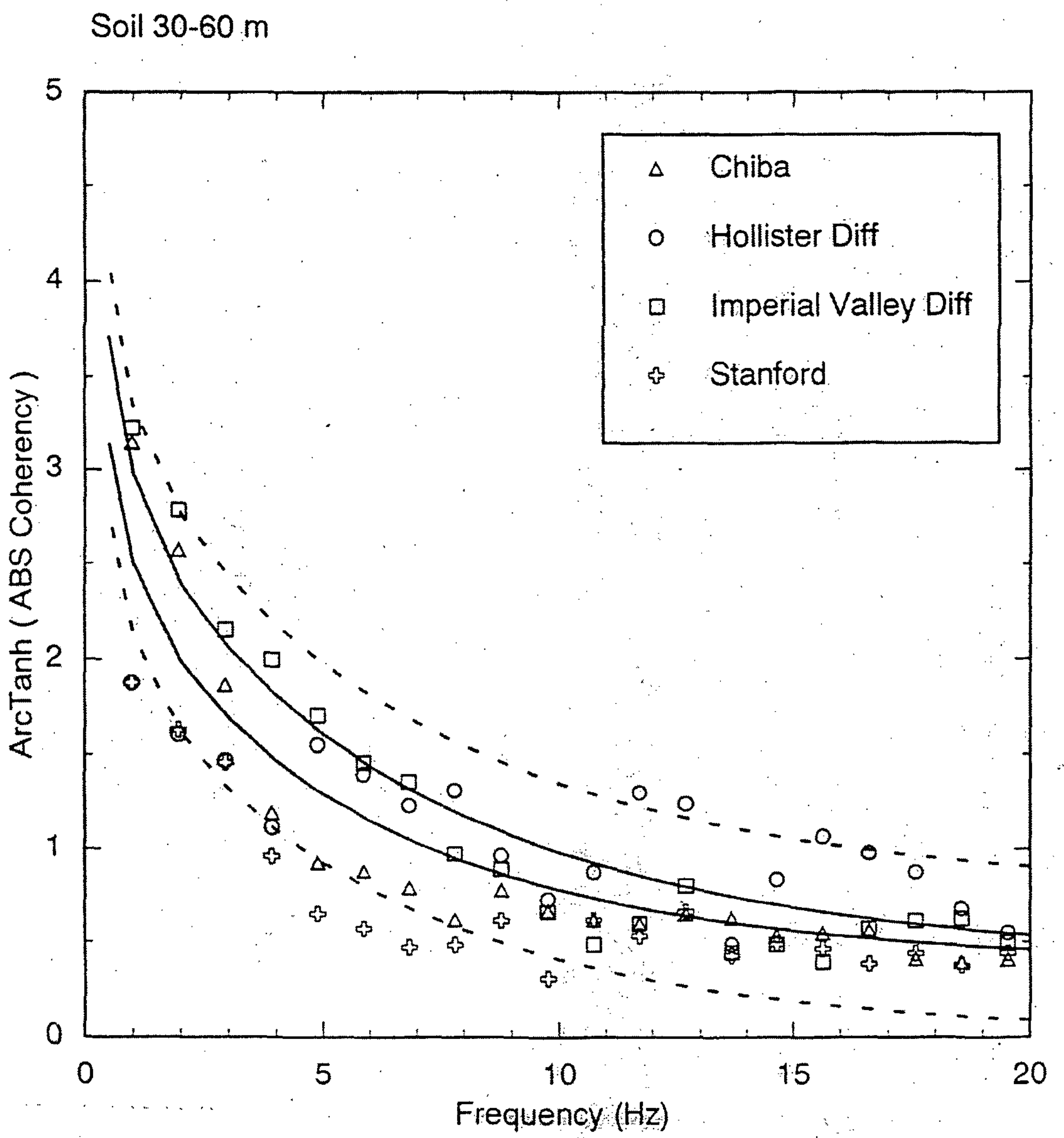

Figure 4-12. Average coherencies from arrays on soil sites for separations distances of 30-60 m. The solid curves show the mean LSST coherency functions for 30 and 60 m. The dashed curves show plus and minus one standard error of the LSST coherency functions.

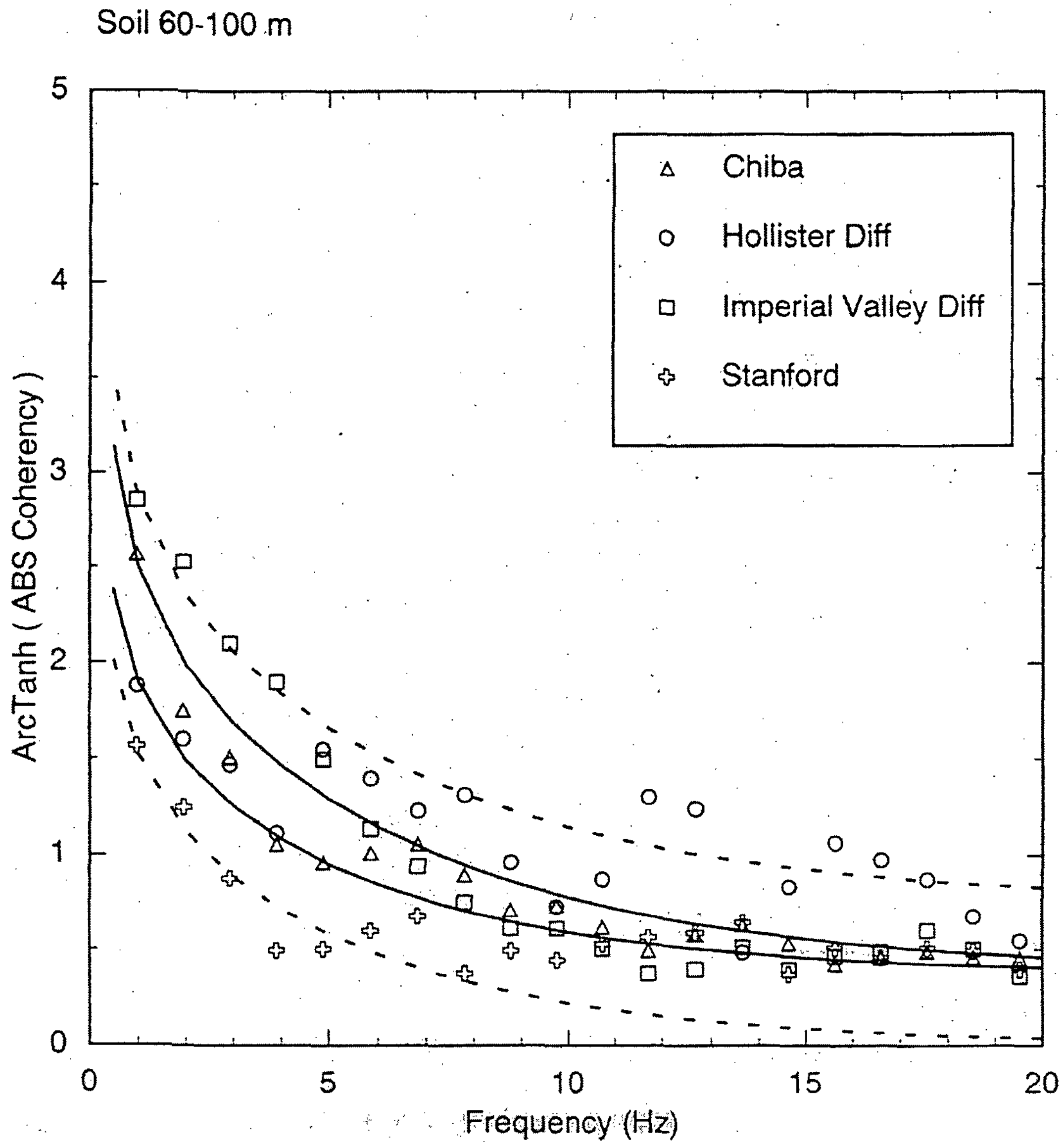

Figure 4-13. Average coherencies from arrays on soil sites for separations distances of 60-100 m. The solid curves show the mean LSST coherency functions for 60 and 100 m. The dashed curves show plus and minus one standard error of the LSST coherency functions.

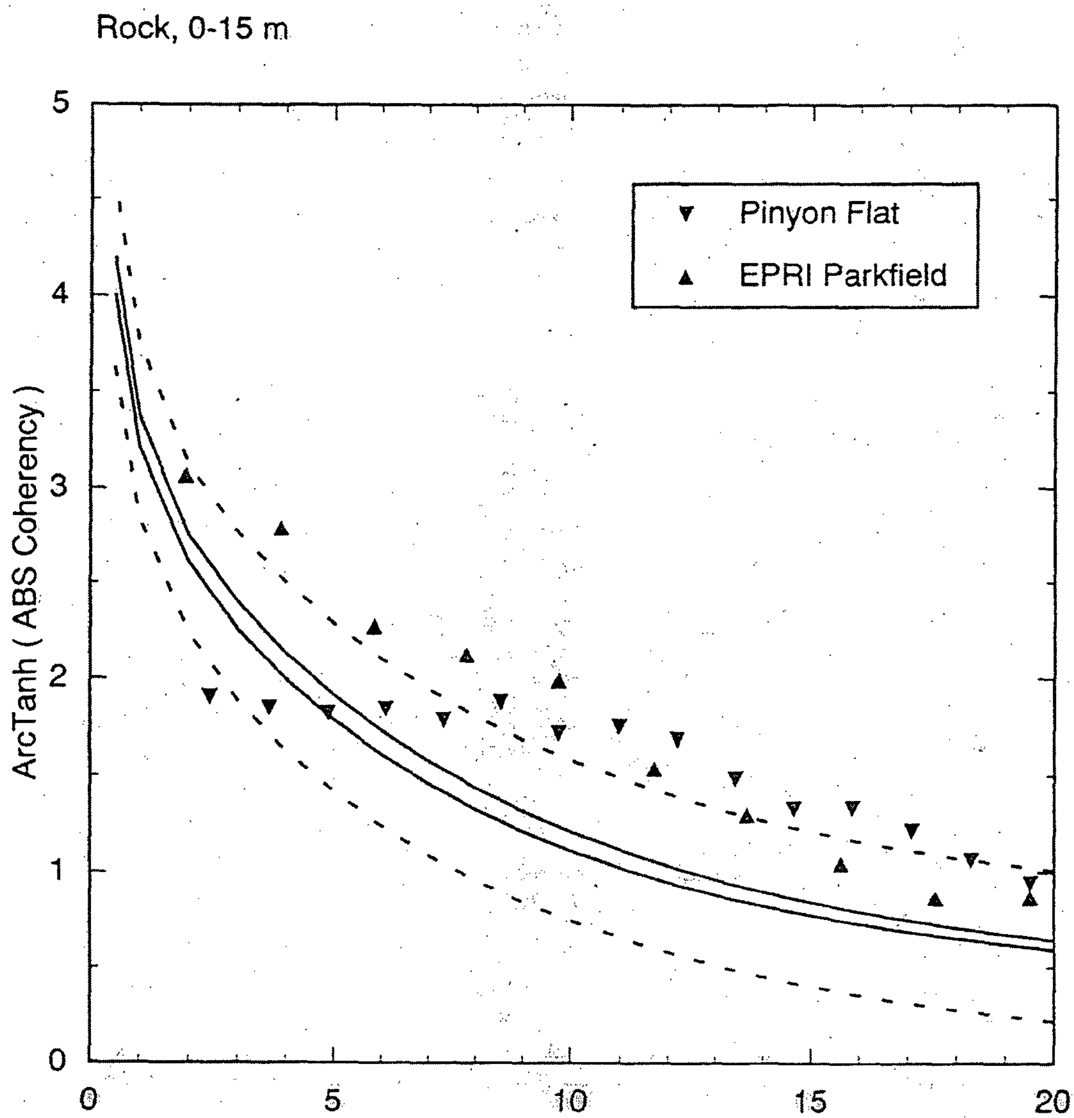

Figure 4-14. Average coherencies from arrays on rock sites for separations distances of 5-15 m. The solid curves show the mean LSST coherency functions for 5 and 15 m. The dashed curves show plus and minus one standard error of the LSST coherency functions.

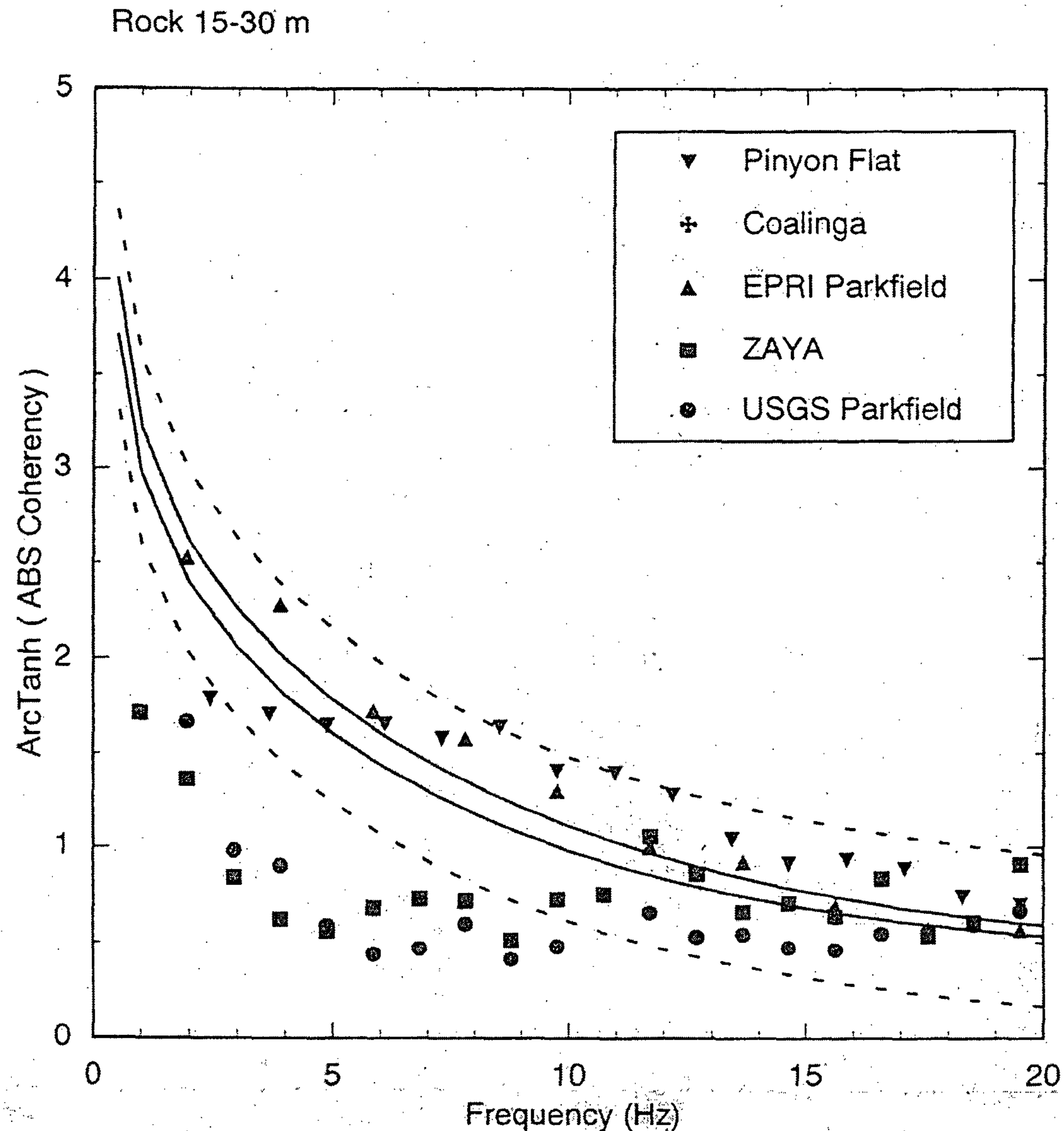

Figure 4-15. Average coherencies from arrays on rock sites for separations distances of 15-30 m. The solid curves show the mean LSST coherency functions for 15 and 30 m. The dashed curves show plus and minus one standard error of the LSST coherency functions.

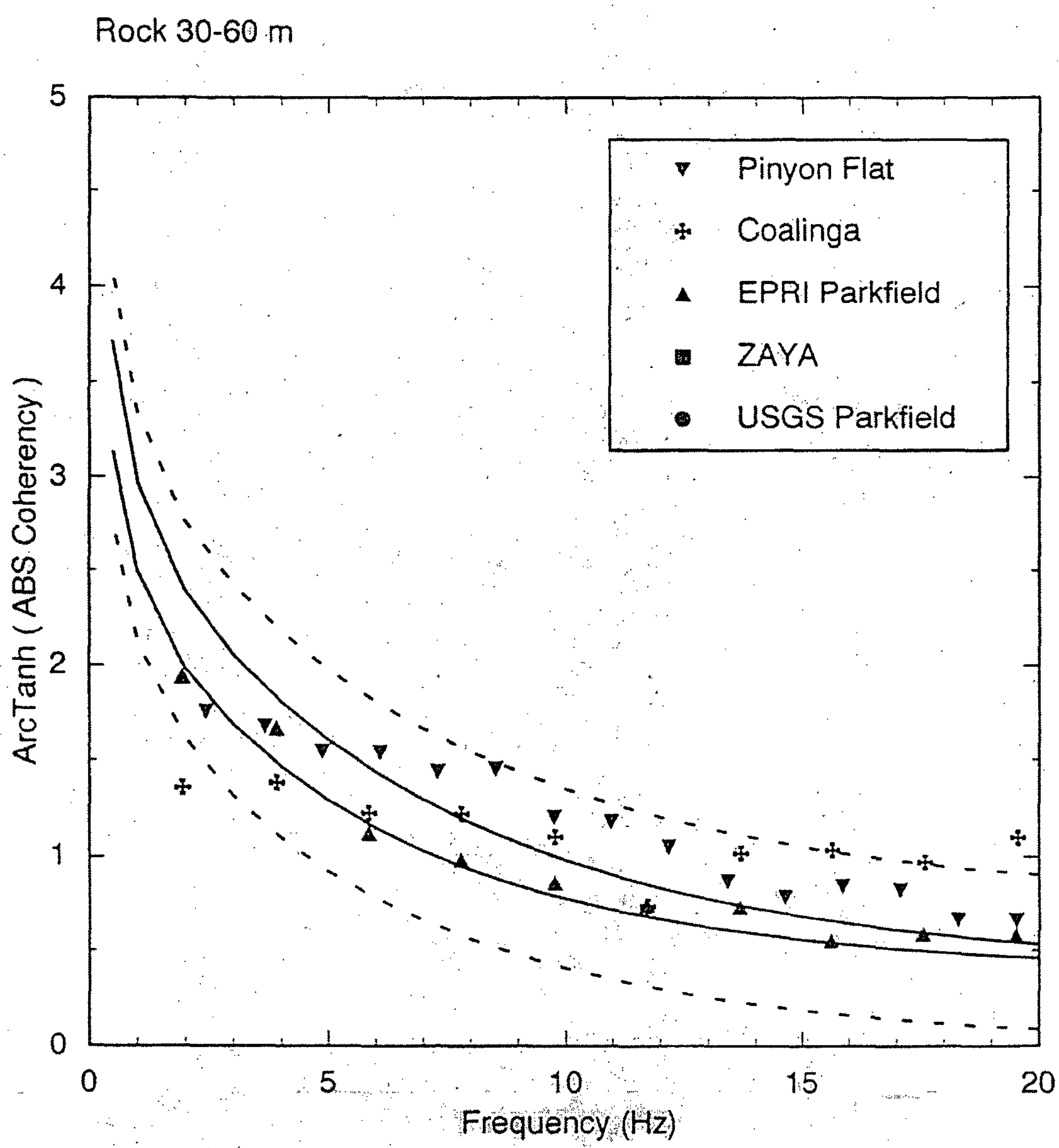

Figure 4-16. Average coherencies from arrays on rock sites for separations distances of 30-60 m. The solid curves show the mean LSST coherency functions for 30 and 60 m. The dashed curves show plus and minus one standard error of the LSST coherency functions.

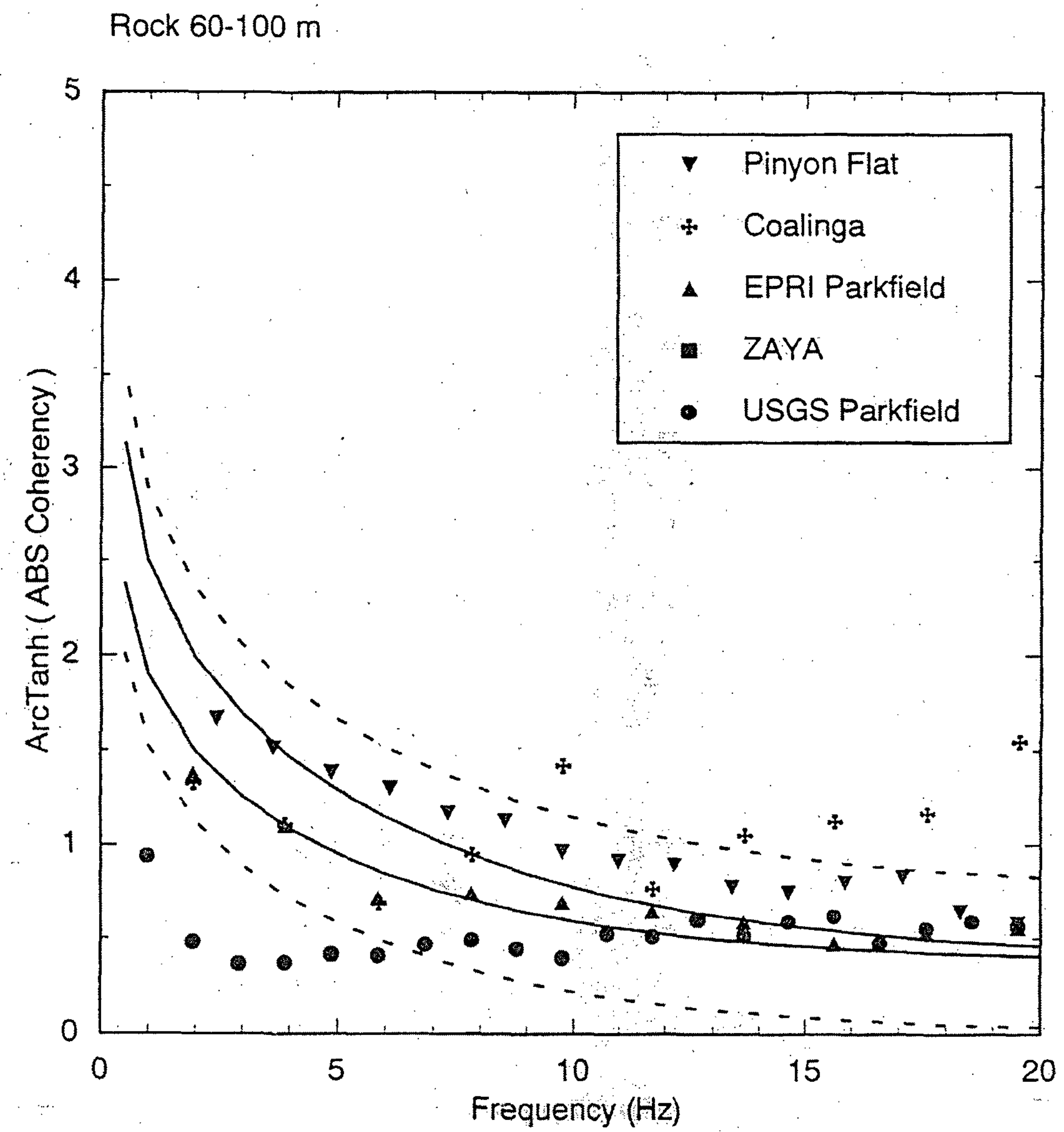

Figure 4-17. Average coherencies from arrays on rock sites for separations distances of 60-100 m. The solid curves show the mean LSST coherency functions for 60 and 100 m. The dashed curves show plus and minus one standard error of the LSST coherency functions.

5

SITE DEPENDENCE OF AMPLITUDE VARIATION

Abrahamson et al. (1991, 1992) developed functional relations for the observed amplitude variation for the Lotung LSST strong motion data set. This model was developed by computing the standard error of the ΔA terms (Eq. 2-4) for selected distance ranges and frequency bands. The dependence of the computed standard errors on separation distance and frequency was used to develop an empirical model of the amplitude variation based on least-squares.

As part of the current study, an alternative methodology was used to model the amplitude variation. Rather than compute the standard error of the ΔA for distance and frequency bins, a maximum likelihood formulation is used. This approach has the advantage that the ΔA do not have to be put into bins to compute the standard error. Instead, various functional forms of the separation distance and frequency dependence of the standard error were tested. The coefficients for each model are estimated using the maximum likelihood method.

The various functional forms that were considered are listed in Table 5-1. Model 3 gave the best fit to the LSST data, but model 7 (which gave the second best fit to the LSST data) gave a better fit to the data from the other arrays. For the comparison of the amplitude variations at different site, the results of the fit to model 7 are used.

The estimated coefficients for model 7 are listed in Table 5-2. The Stanford array is not included because the scaling between different instruments in the array is uncertain.

Comparison of Amplitude Variations

The estimated amplitude variation functions for the three soil arrays are compared to the LSST amplitude variation function in Figures 5-1 to 5-3 for separation distances of 20m, 60m, and 100m, respectively. The amplitude variation functions for the three soil arrays are similar to the LSST amplitude variation function, indicating that the along waveform variation

with the coherency, the LSST amplitude variation function is applicable to generic soil sites.

Similarly, the estimated amplitude variation functions for the five rock arrays are compared to the LSST amplitude variation function in Figures 5-4 to 5-6 for separation distances of 20m, 60m, and 100m, respectively. The rock arrays show much larger variability in the amplitude variation than do the soil arrays. This trend is consistent with the larger variability of coherency found for rock arrays as compared to soil arrays. marginal The Coalinga and Pinyon Flat arrays show similar amplitude variation as the LSST model, but the EPRI Parkfield, USGS Parkfield, and ZAYA arrays show significantly larger amplitude variations than the LSST model.

Generally, the range of amplitude variations is greater than the range of coherencies, suggesting that amplitude variation is more sensitive to local site conditions than is coherency. One source of this difference is site resonance in that a slight shift in resonance across a site can easily generate large variations in amplitude (at a given frequency), but have little or no effect on coherency. In this regard, small changes in layer thickness would produce more predominant shifts in resonance for shallow layers; thus shallow soil sites and rock sites with complex geology would tend to experience the largest amplitude variations.

Table 5-1.
Models Considered for the Amplitude Variation

Model	Functional Form
1	$\sigma = A(1-e^{Bf})$
2	$\sigma = A(1-e^{B\xi f})$
3	$\sigma = A(1-e^{Bf+C\xi})$
4	$\sigma = A(1-e^{Bf+C\xi^2})$
5	$\sigma^2 = A(1-e^{Bf+C\xi})$
6	$\sigma^2 = A(1-e^{Bf+C\xi^2})$
7	$\sigma = A(1-e^{Bf+Cf\xi})$
8	$\sigma^2 = A(1-e^{Bf+Cf\xi})$

(f = frequency in Hz, ξ = separation distance in m)

Table 5-2.
Model Coefficients for Amplitude Variation (Model 7)

Array	A	B	C	
LSST	0.93	-0.163	-0.0019	soil
USGS Parkfield	1.01	-0.29	-0.0056	rock
ZAYA	1.07	0.00	-0.018	rock
Imperial Valley Diff	1.09	-0.07	-0.0012	soil
Hollister Diff	0.94	-0.05	-0.0041	soil
EPRI Parkfield	1.23	-0.019	-0.0035	rock
Chiba	1.11	-0.102	-0.0011	soil
Pinyon Flat	0.79	-0.45	-0.0017	rock

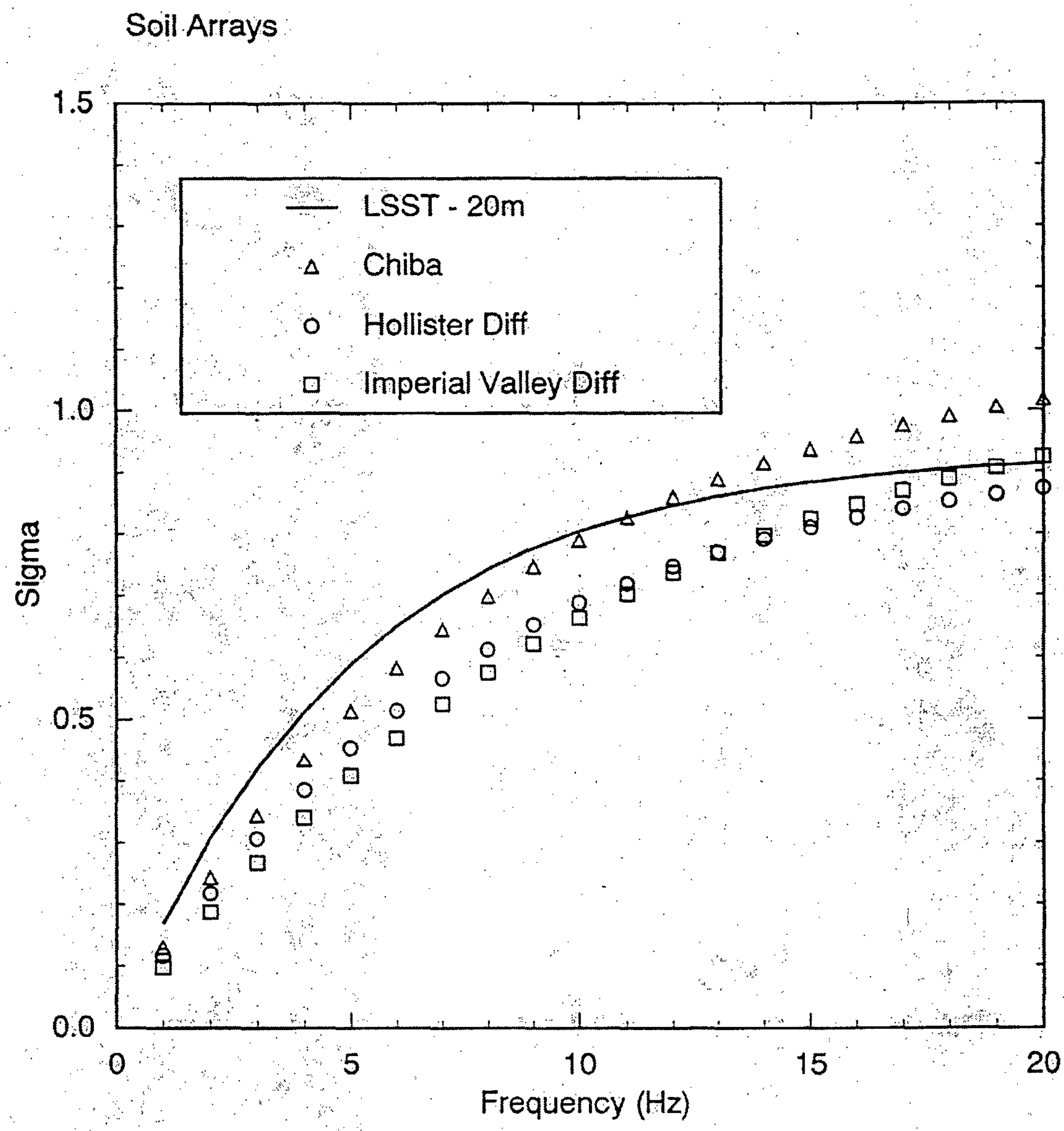

Figure 5-1. Amplitude variations from arrays on soil sites for a separation distance of 20 m.

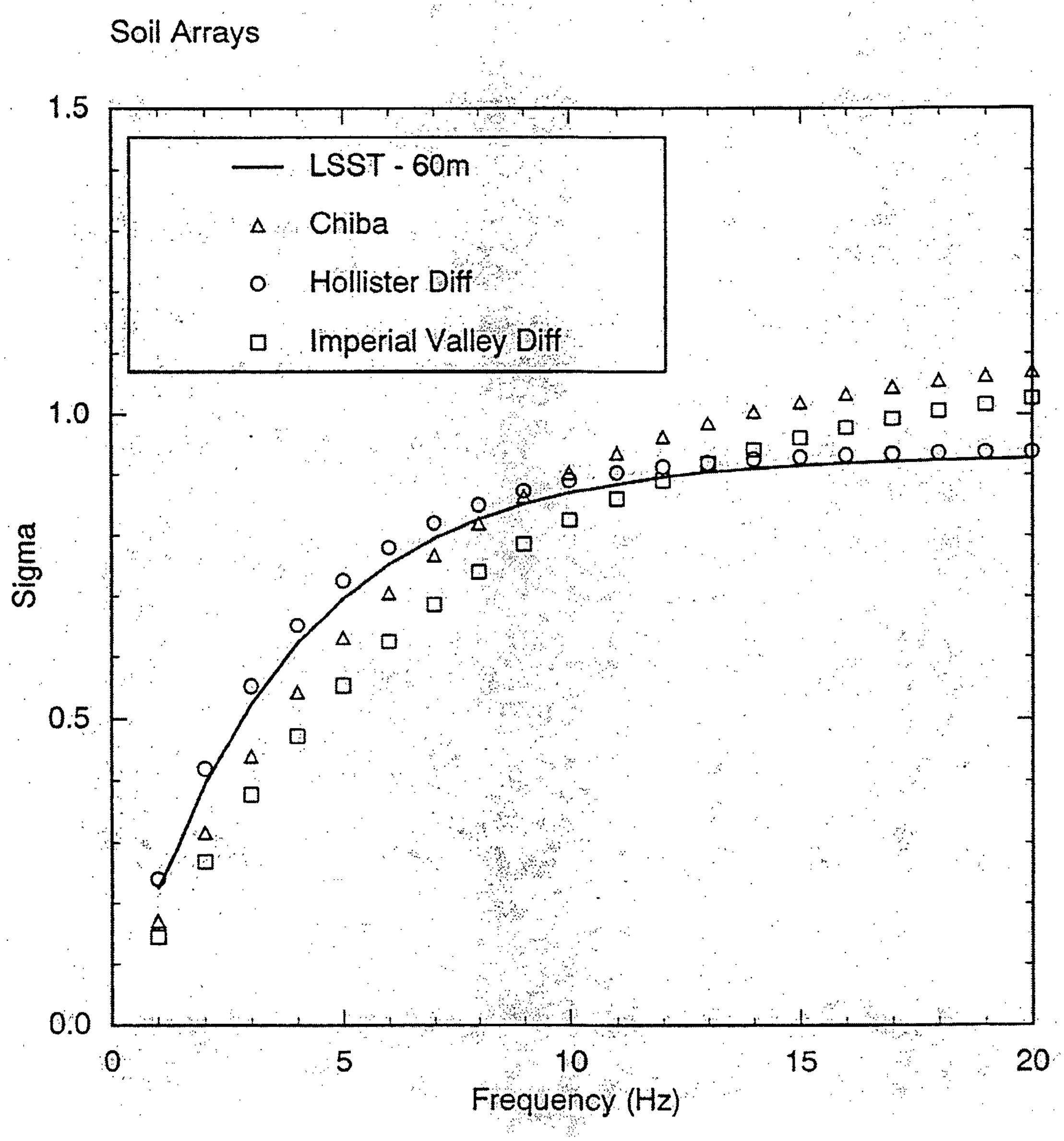

Figure 5-2. Amplitude variations from arrays on soil sites for a separation distance of 60 m.

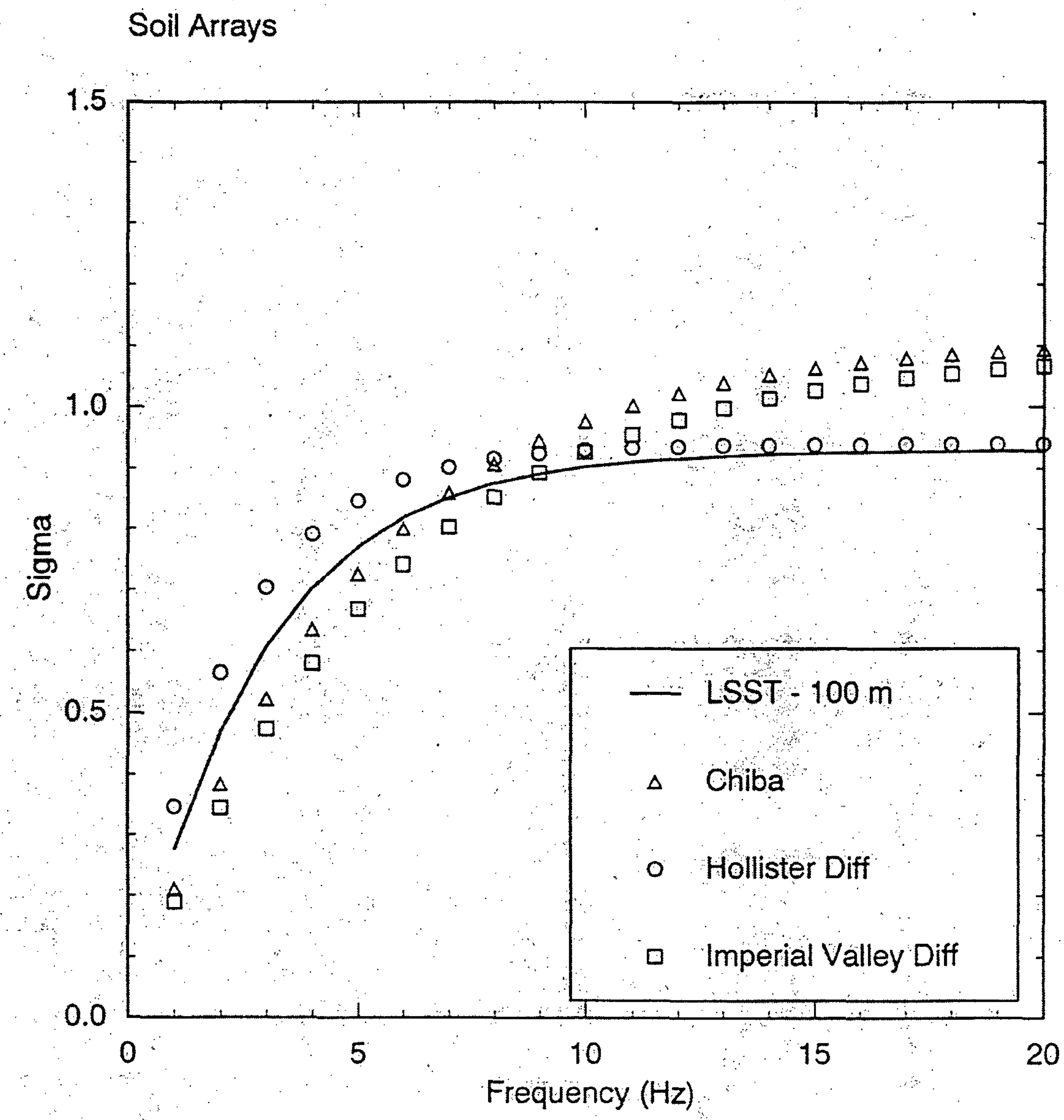

Figure 5-3. Amplitude variations from arrays on soil sites for a separation distance of 100 m.

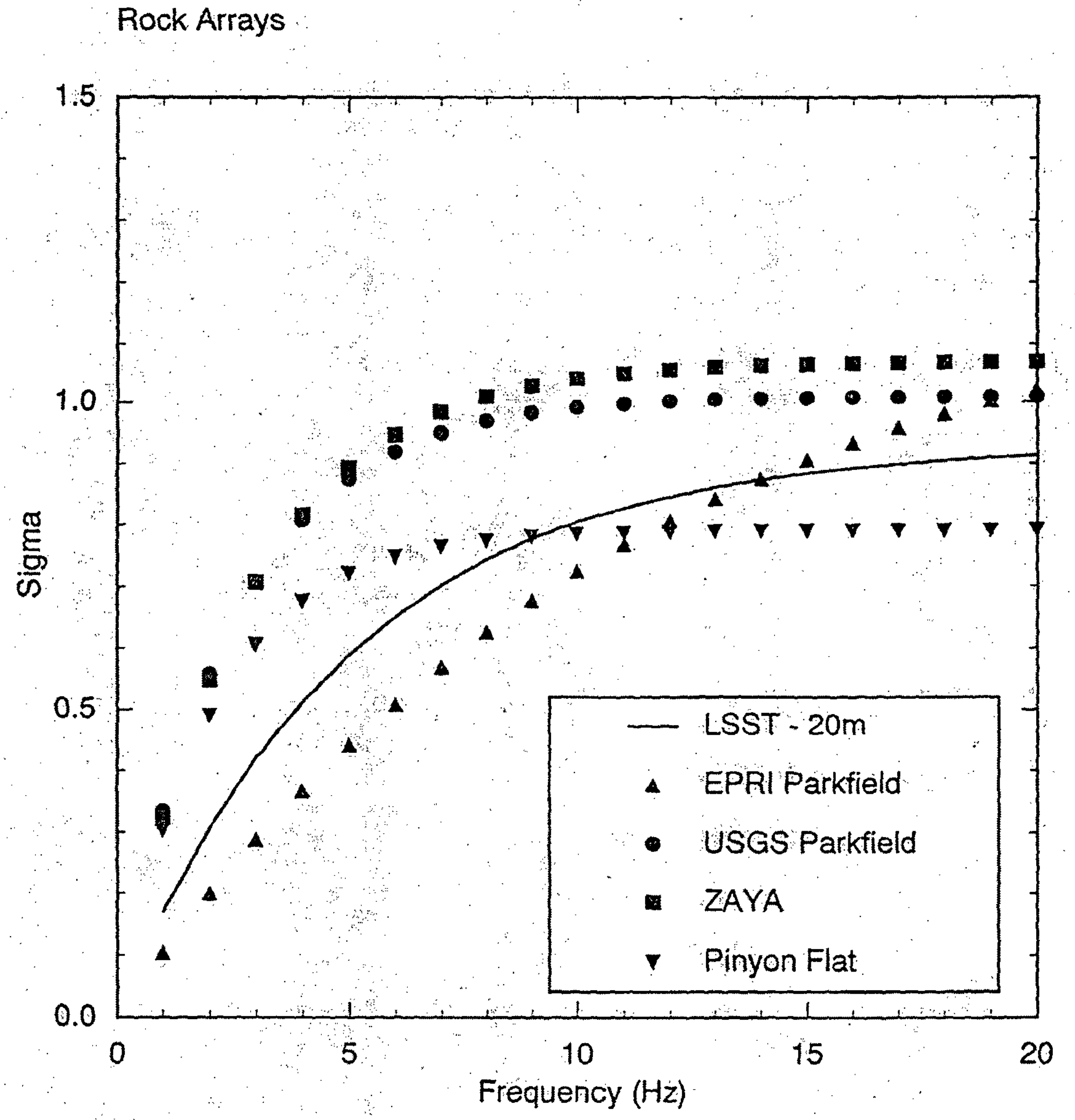

Figure 5-4. Amplitude variations from arrays on rock sites for a separation distance of 20 m.

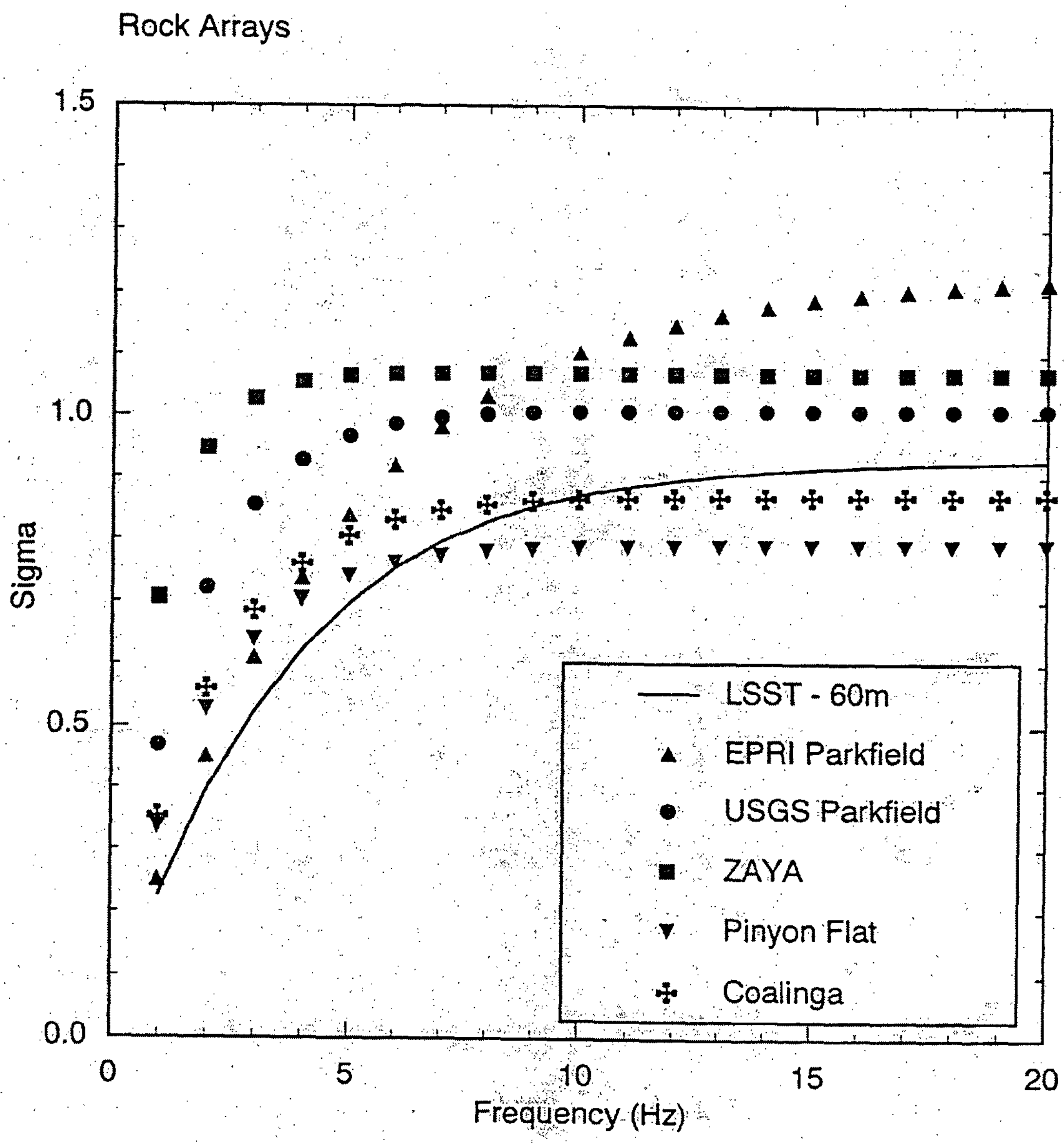

Figure 5-5. Amplitude variations from arrays on rock sites for a separation distance of 60 m.

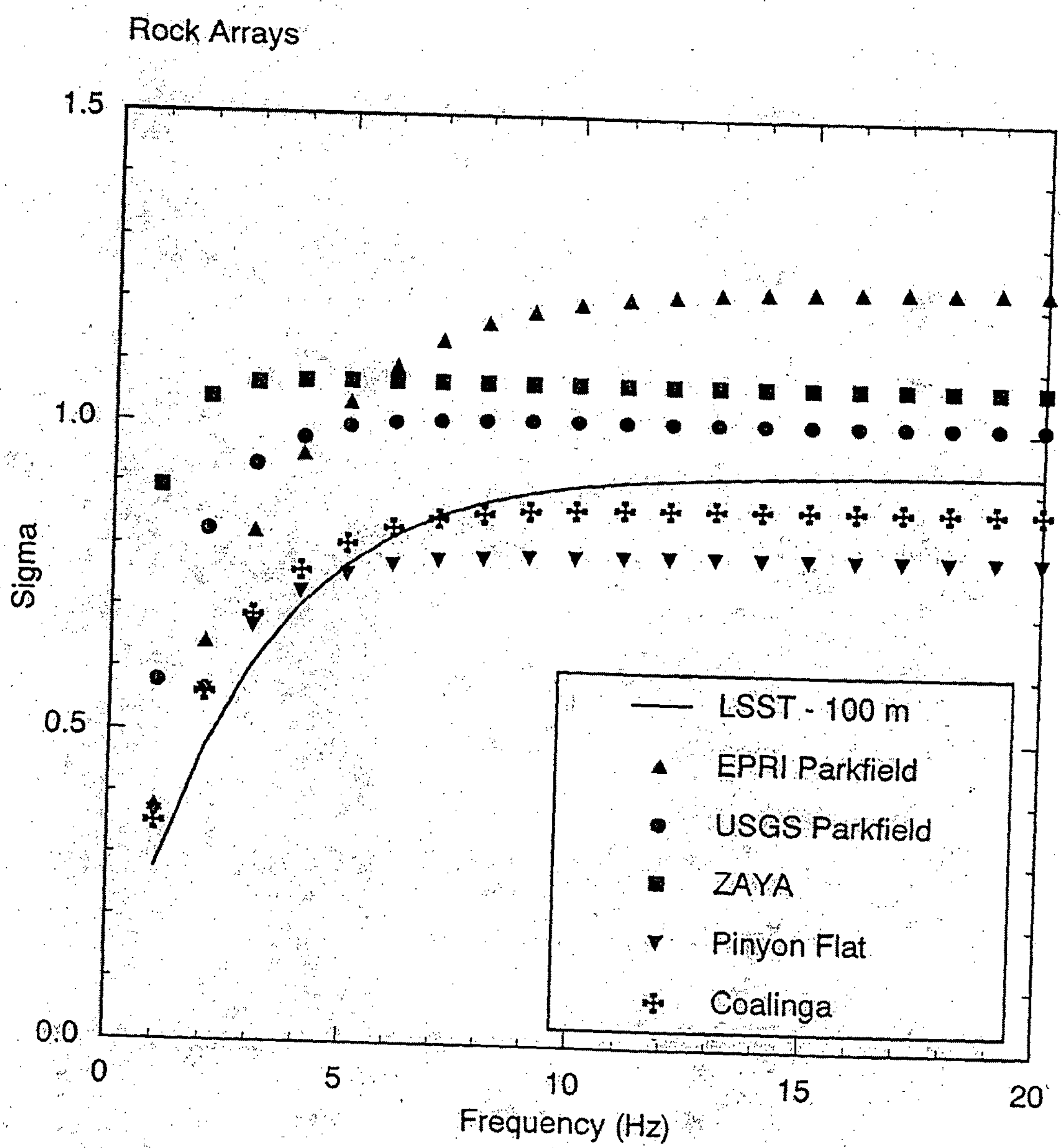

Figure 5-6. Amplitude variations from arrays on rock sites for a separation distance of 100 m.

6

USE OF MICRO-TREMOR DATA

As shown in Section 4, the spatial coherency for soil sites is similar from site to site, but it is more variable for rock sites. Ideally, array recordings at the site of interest would be used to estimate site-specific coherency function. Since most project do not have the time to set up a dense array of instruments and wait for earthquakes, other methods need to be considered such as using micro-tremore data or explosive sources. In this section, we evaluate the usefulness of micro-tremor data for estimating the site-specific coherency.

Micro-Tremor Data

Micro-tremors were measured at the EPRI Parkfield array site. Four temporary accelerometers were located at the some of the same locations as the permanent stations and run at high gain to record micro-tremors. The stations were moved around to different permanent station locations to sample the coherency for different station pairs. In all seven micro-tremor runs are used to estimate the coherency. These seven runs are listed in Table 6-1.

For each run, a five second time window is selected. The time windows for the runs were selected to avoid spikes in the data. The micro-tremor data are shown in Figures 6-1 to 6-7. In each case, the time window from 5 to 10 seconds is used.

Comparison With Earthquake Data

The coherencies computed from the micro-tremor data are compared to the average coherency from the two Parkfield earthquakes (see Section 3) in Figures 6-8 to 6-12 for separation distance ranges of 0-15 m, 15-30 m, 30-80 m, 80-150 m, and 150-300 m. The solid line shows the mean coherency of the two Parkfield earthquakes (Table 3-4) and the dashed lines show plus and minus one standard error. For all five distance ranges, the mean of the coherencies from the micro-tremor data is lower than the mean coherencies from the earthquake data.

Although the micro-tremor data exhibits coherency above the noise level at very short separations (e.g. Figures 6-8 and 6-9), the coherency from the micro-tremor data is not an accurate predictor of the S-wave window coherency during earthquakes. Therefore, we conclude that the use of micro-tremor data is not helpful in estimating site-specific coherency.

Table 6-1.
Ambient Noise Data

Window	Identifier	Stations	Peak Amplitude (cm/s/s)
1	9:34:53	NE4	0.015
		W1	0.005
		W2	0.012
2	11:31:27	NE4	0.014
		W3	0.004
		W4	0.003
3	12:40:11	NE3	0.008
		NE4	0.008
4	17:07:36	NE1	0.034
		NE4	0.030
5	18:44:45	G0	0.006
		NE4	0.017
		SE1	0.005
6	19:46:38	NE4	0.013
		SE2	0.007
		SE3	0.020
7	21:06:37	G0	0.009
		NE4	0.010
		SE4	0.006

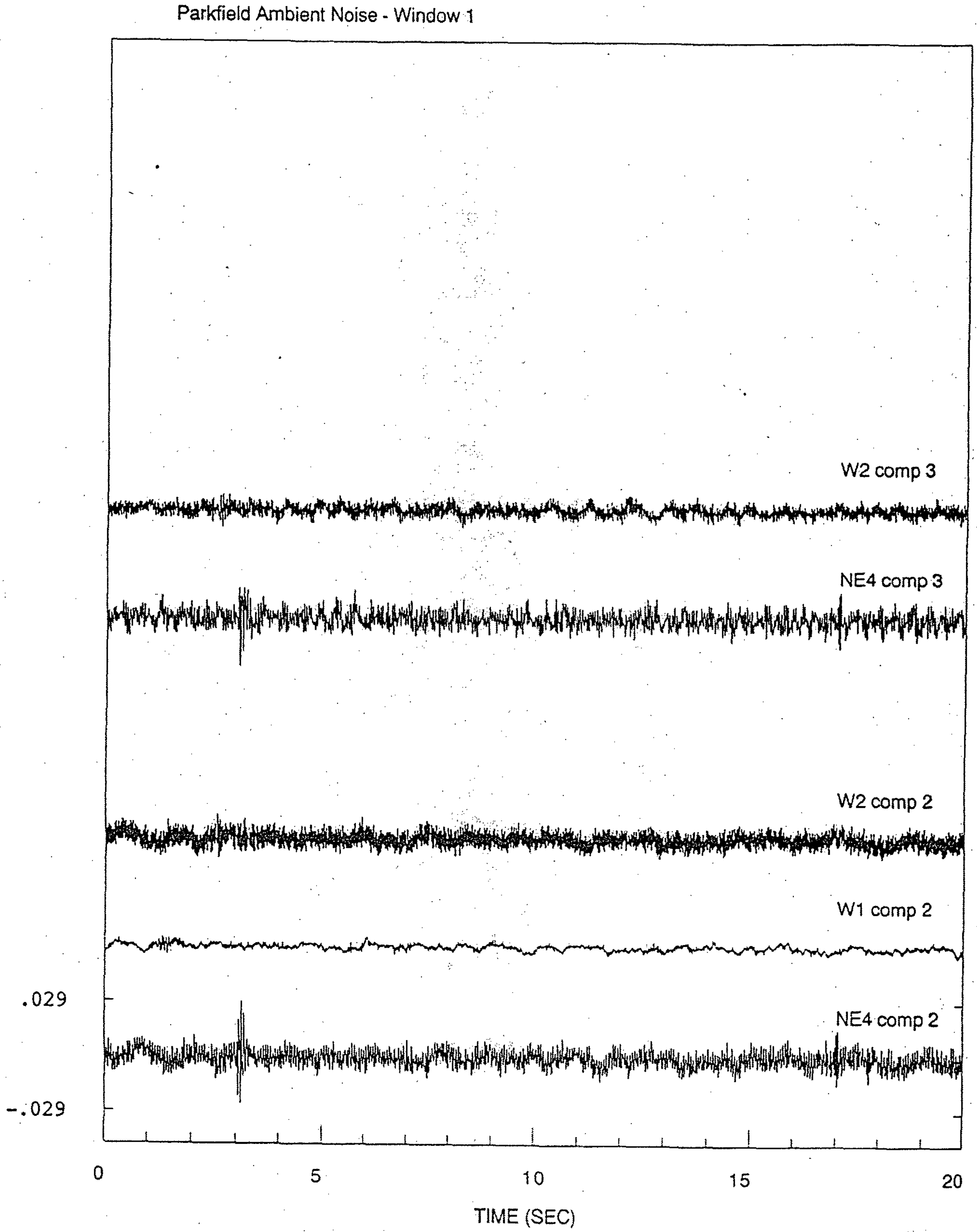

Figure 6-1. Ambient noise time histories for window 1.

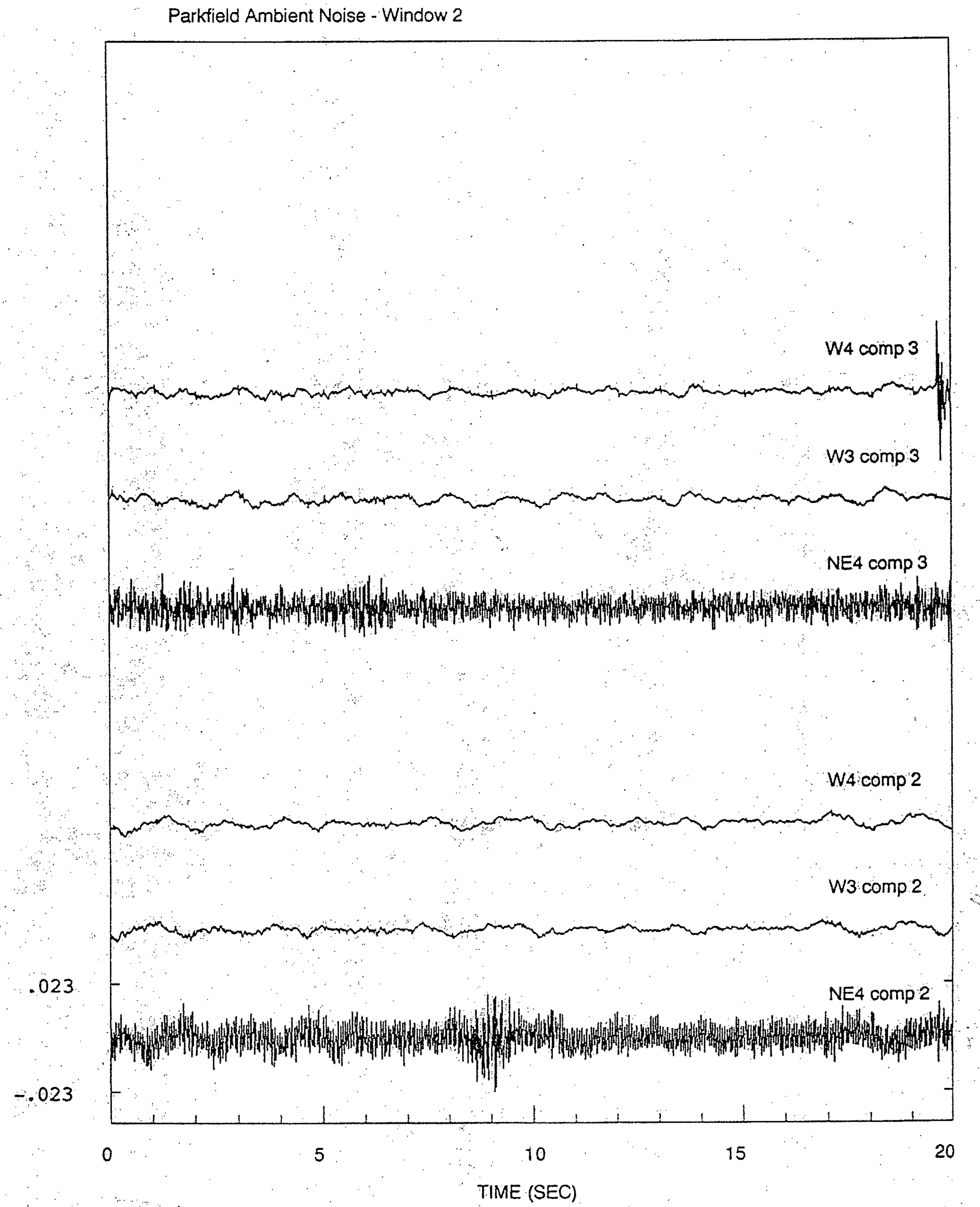

Figure 6-2. Ambient noise time histories for window 2.

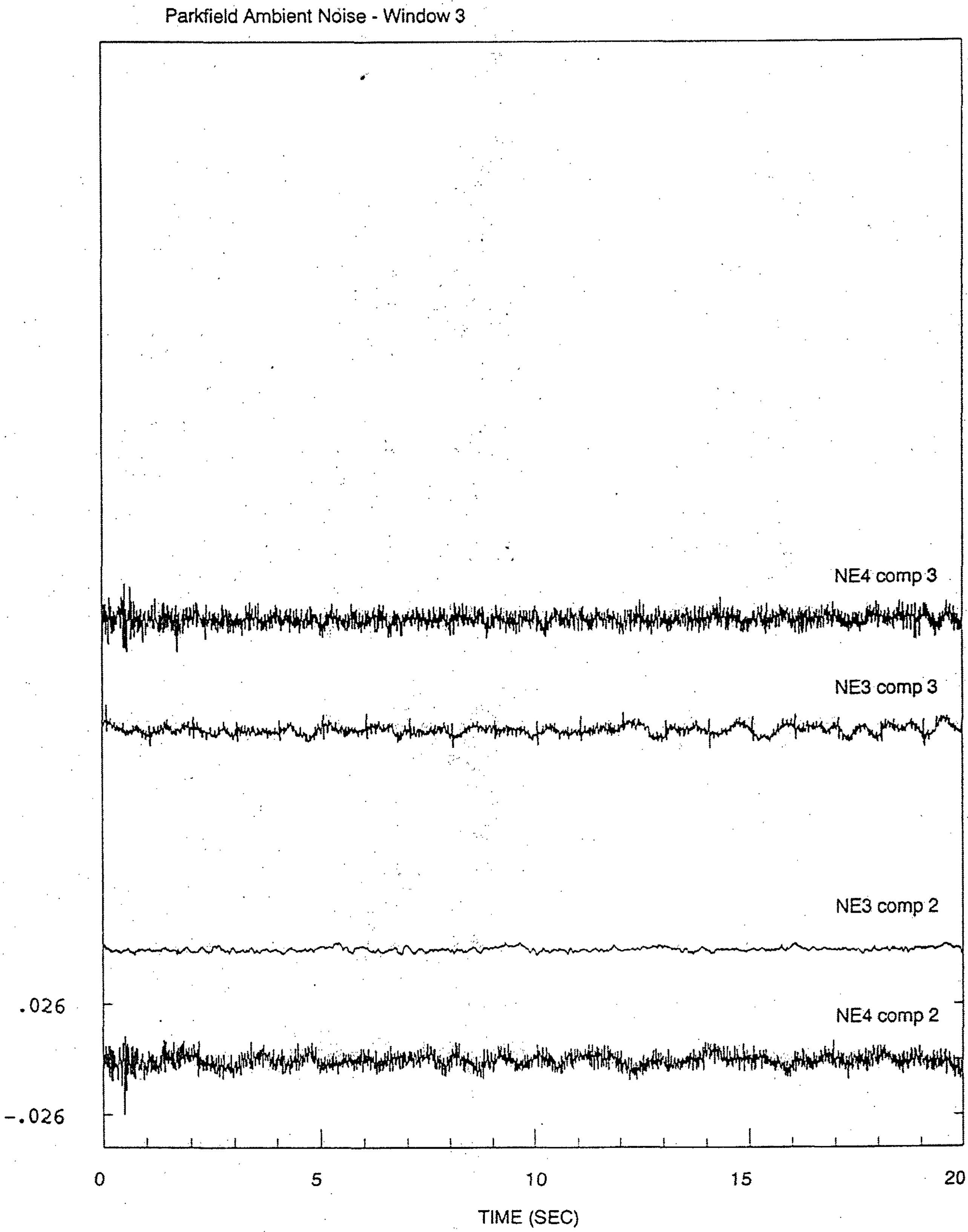

Figure 6-3. Ambient noise time histories for window 3.

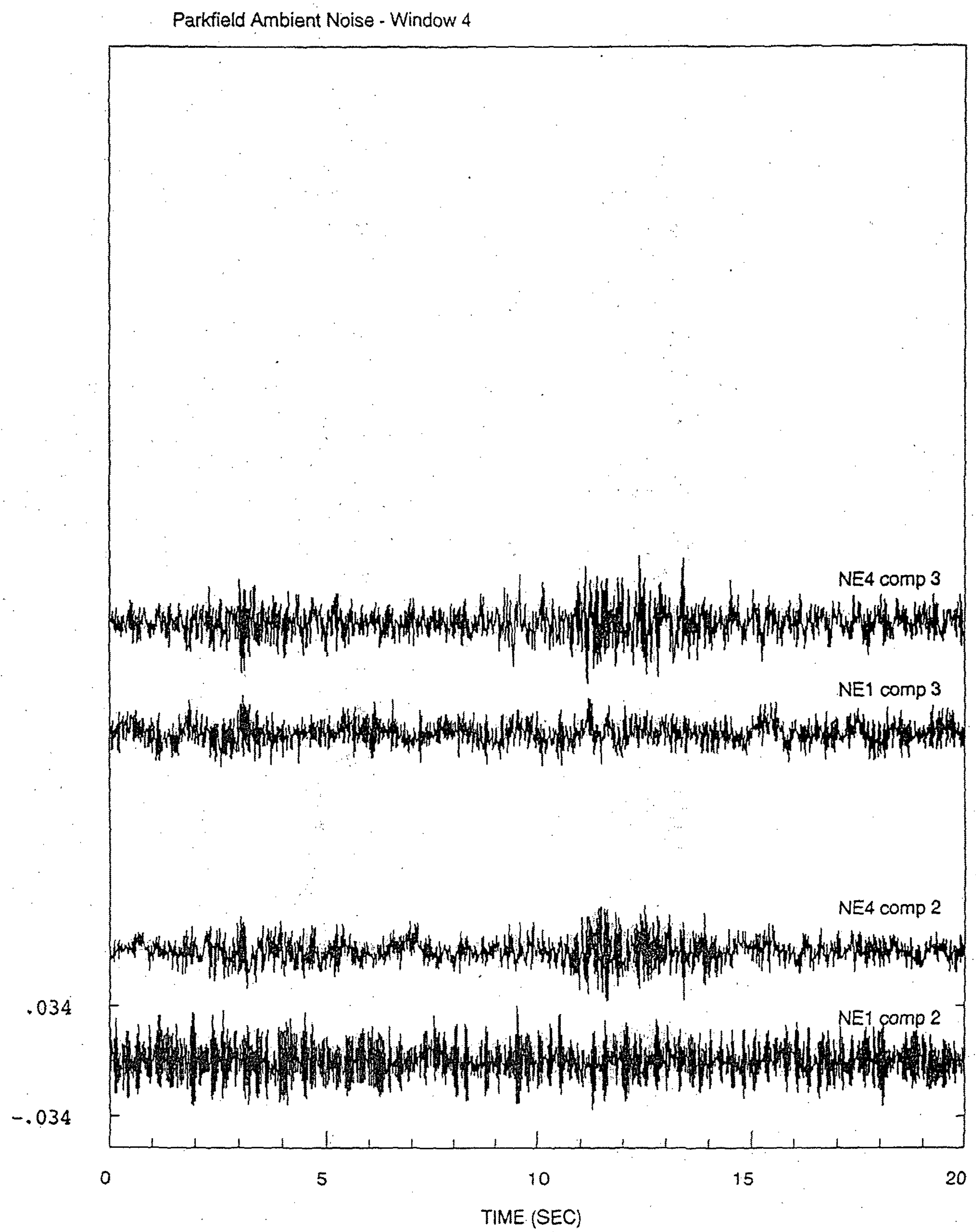

Figure 6-4. Ambient noise time histories for window 4.

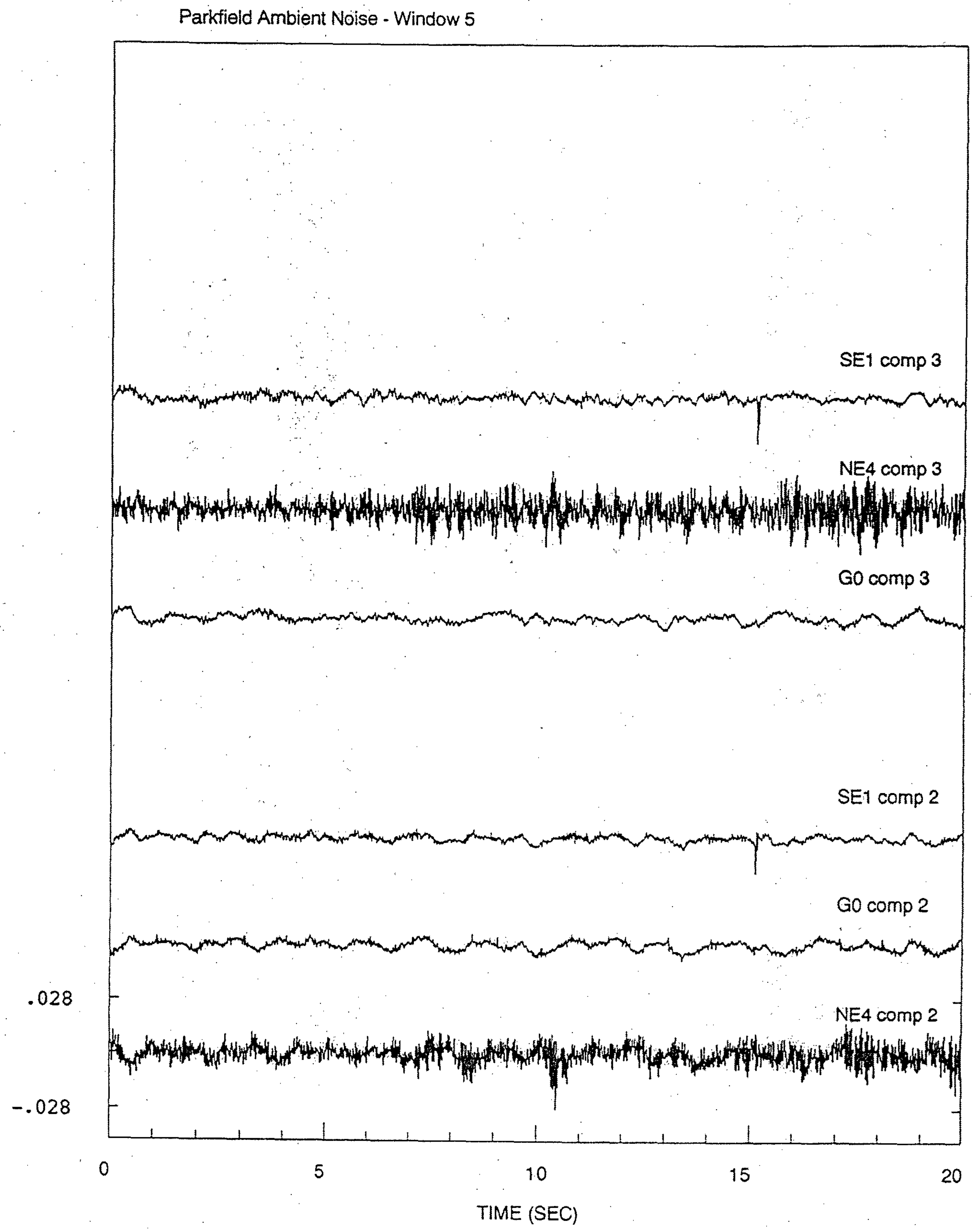

Figure 6-5. Ambient noise time histories for window 5.

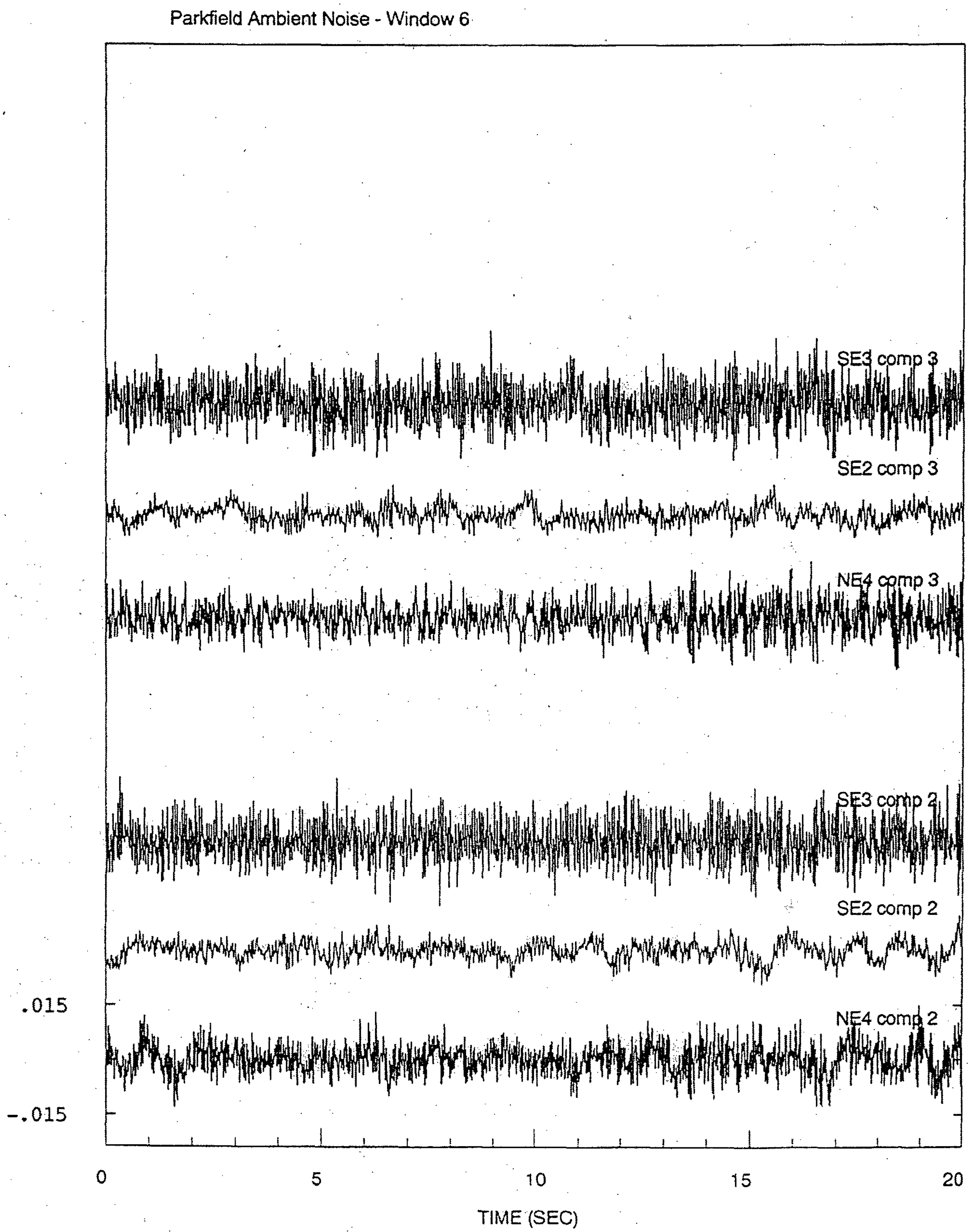

Figure 6-6. Ambient noise time histories for window 6.

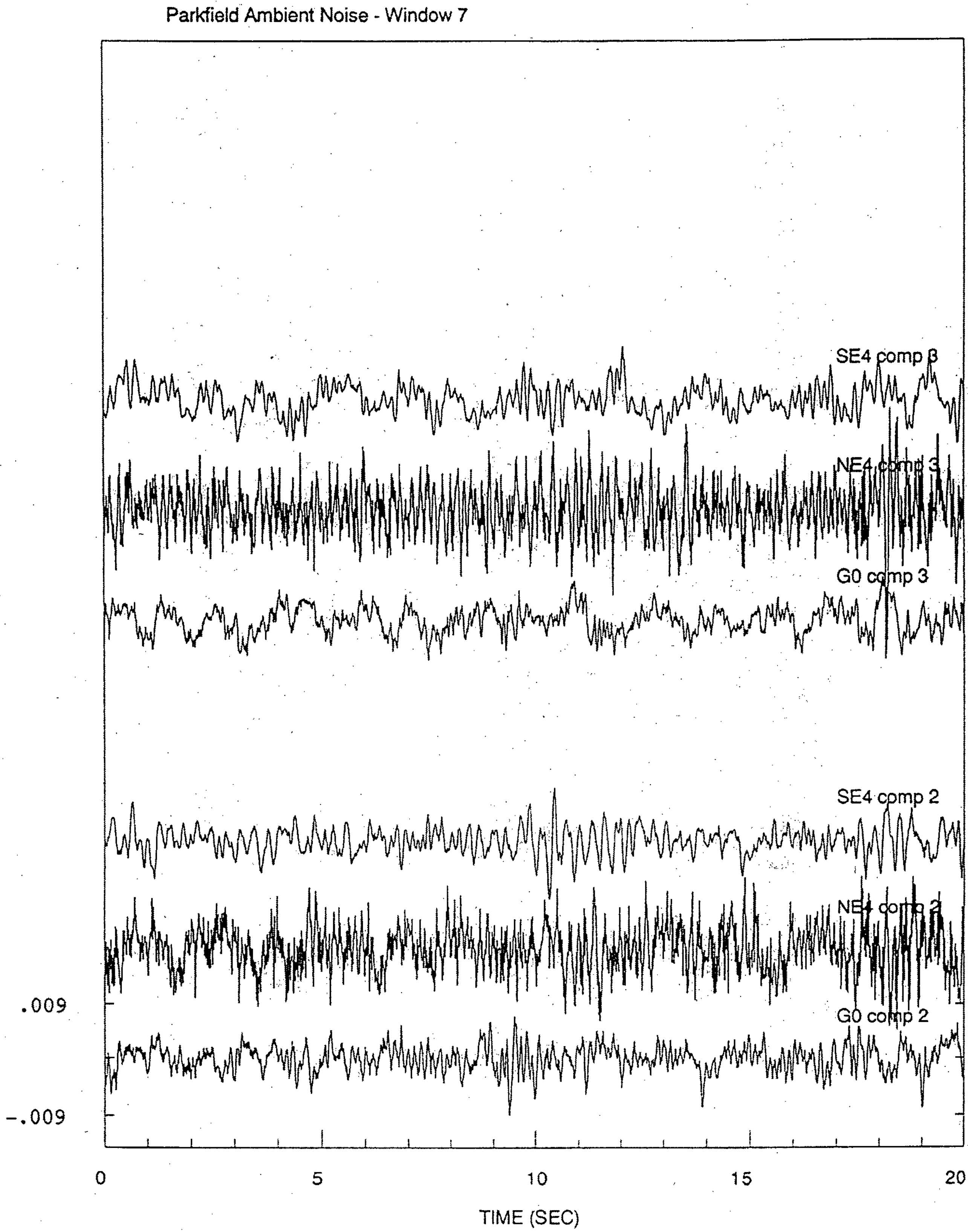

Figure 6-7. Ambient noise time histories for window 7.

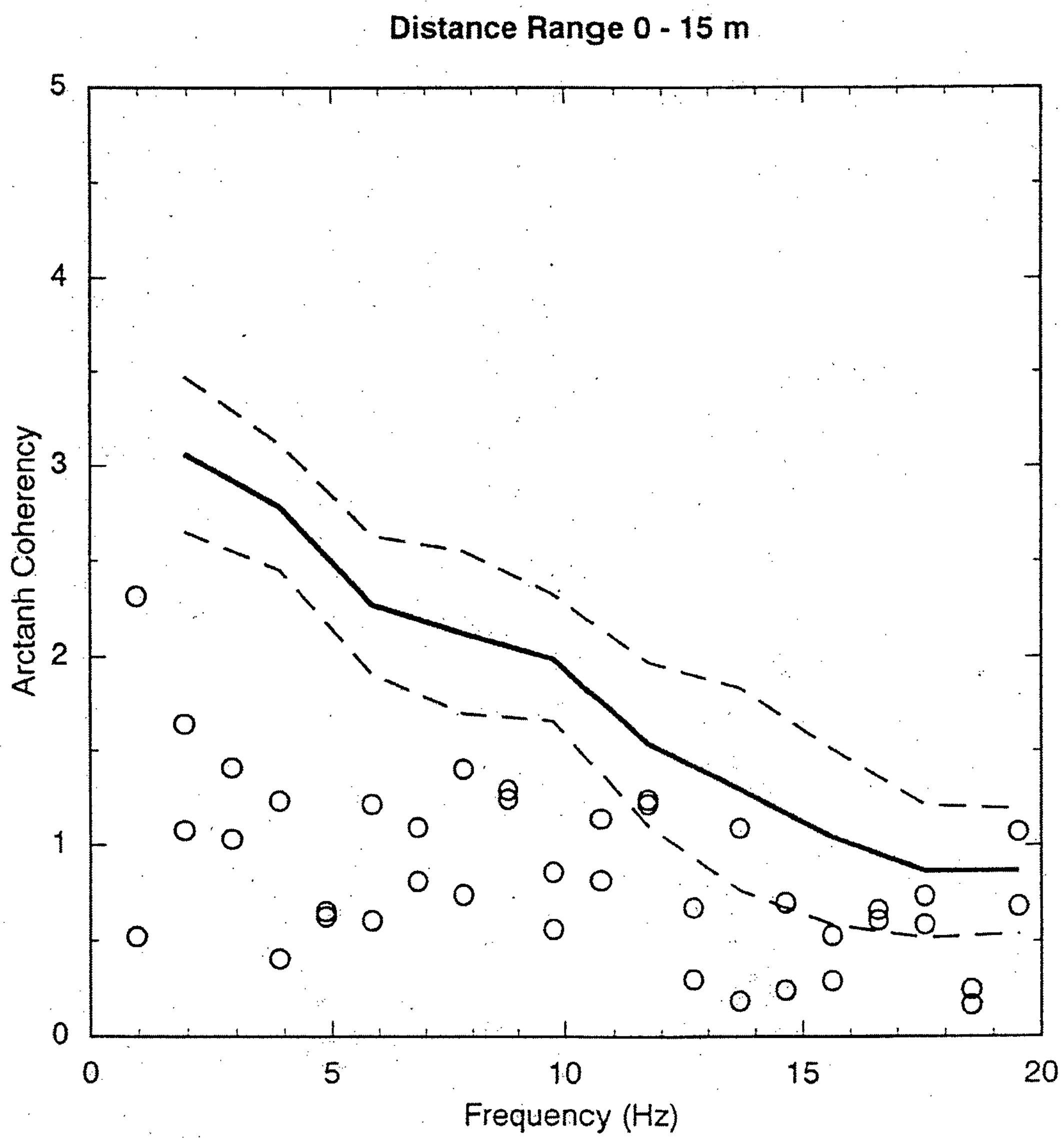

Figure 6-8. Comparison of coherency from ambient noise with the coherency from small earthquakes at the EPRI Parkfield array. Separation distance 5-15 m.

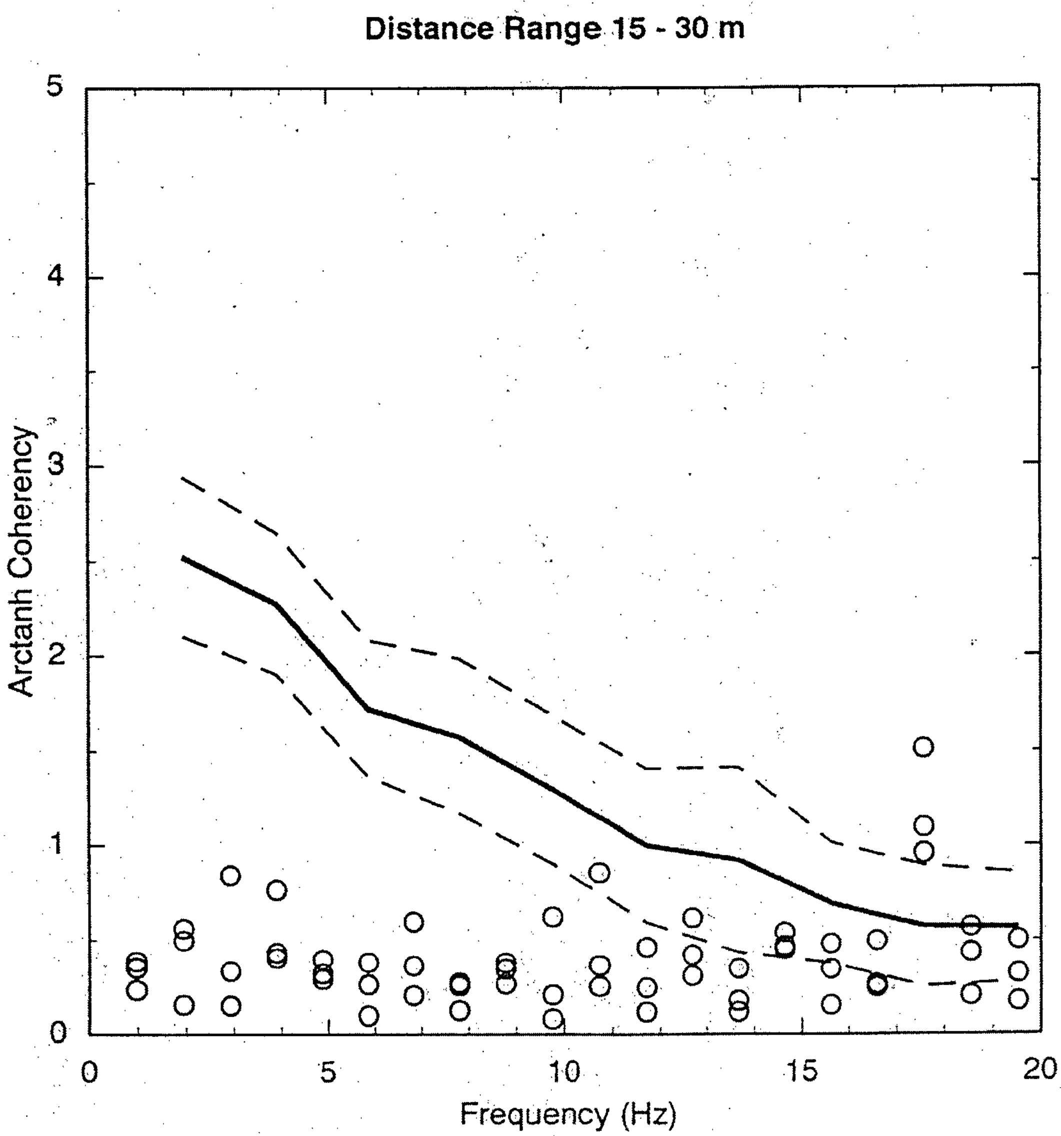

Figure 6-9. Comparison of coherency from ambient noise with the coherency from small earthquakes at the EPRI Parkfield array. Separation distance 15-30 m.

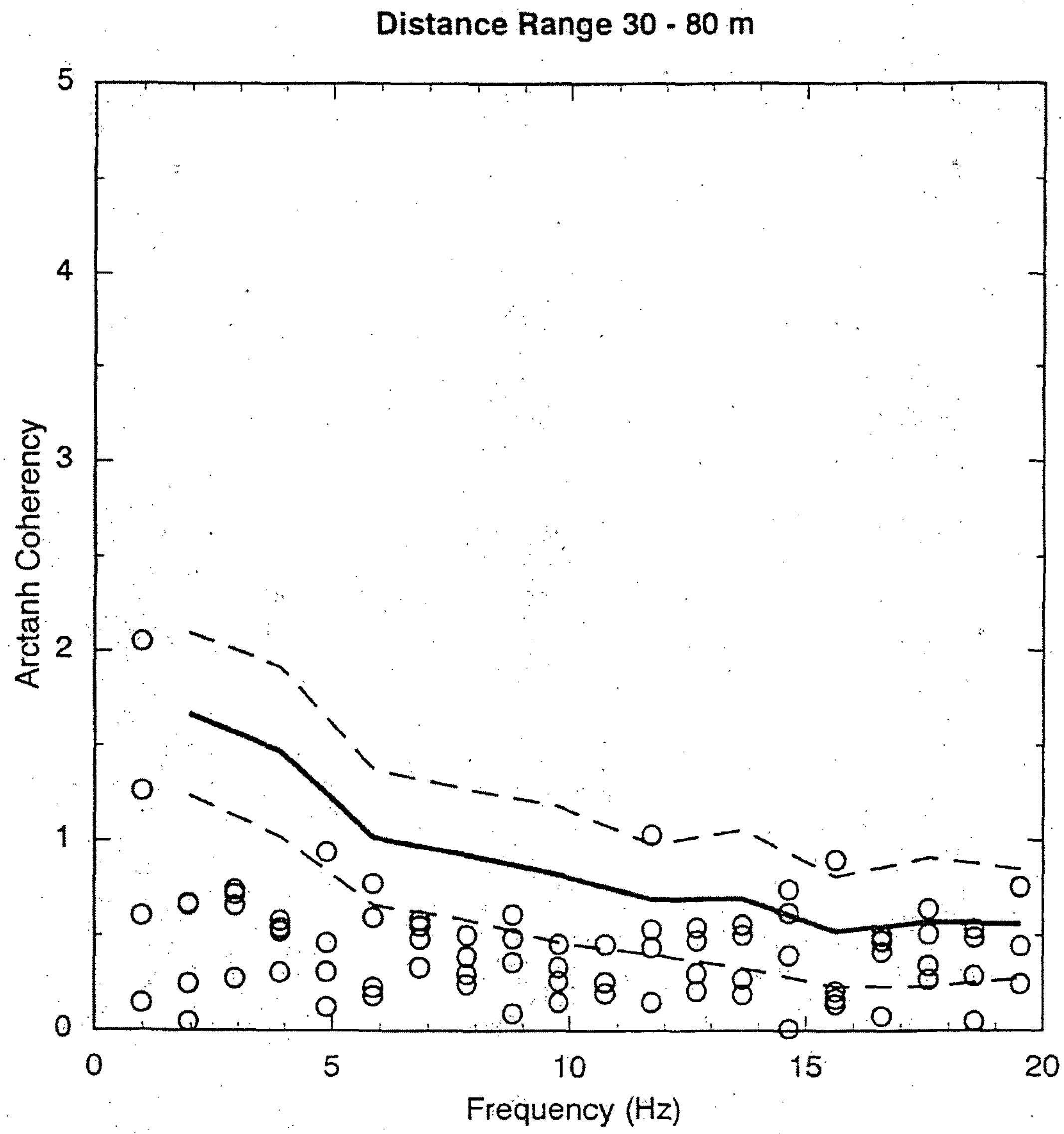

Figure 6-10. Comparison of coherency from ambient noise with the coherency from small earthquakes at the EPRI Parkfield array. Separation distance 30-80 m.

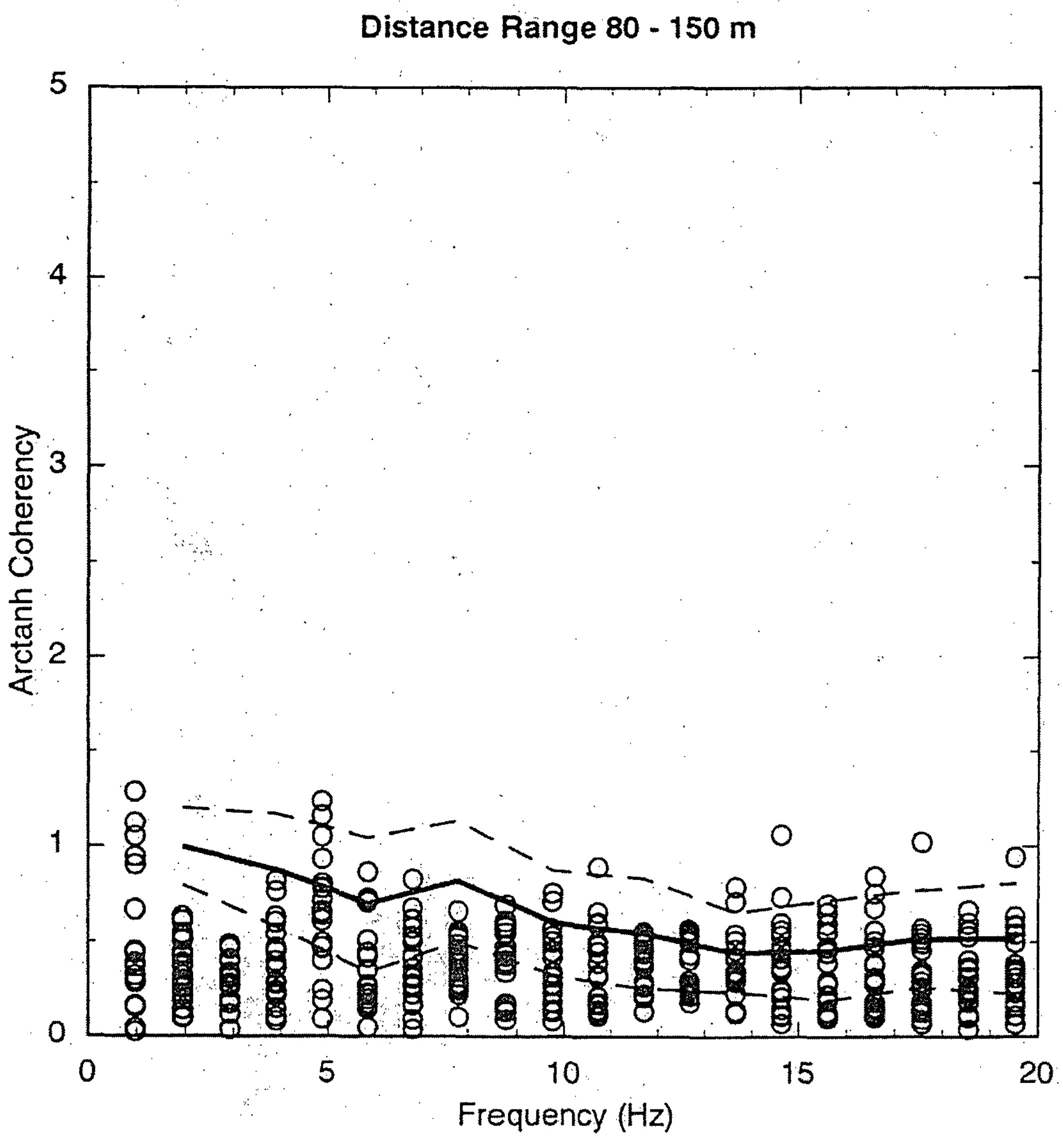

Figure 6-11. Comparison of coherency from ambient noise with the coherency from small earthquakes at the EPRI Parkfield array. Separation distance 80-150 m.

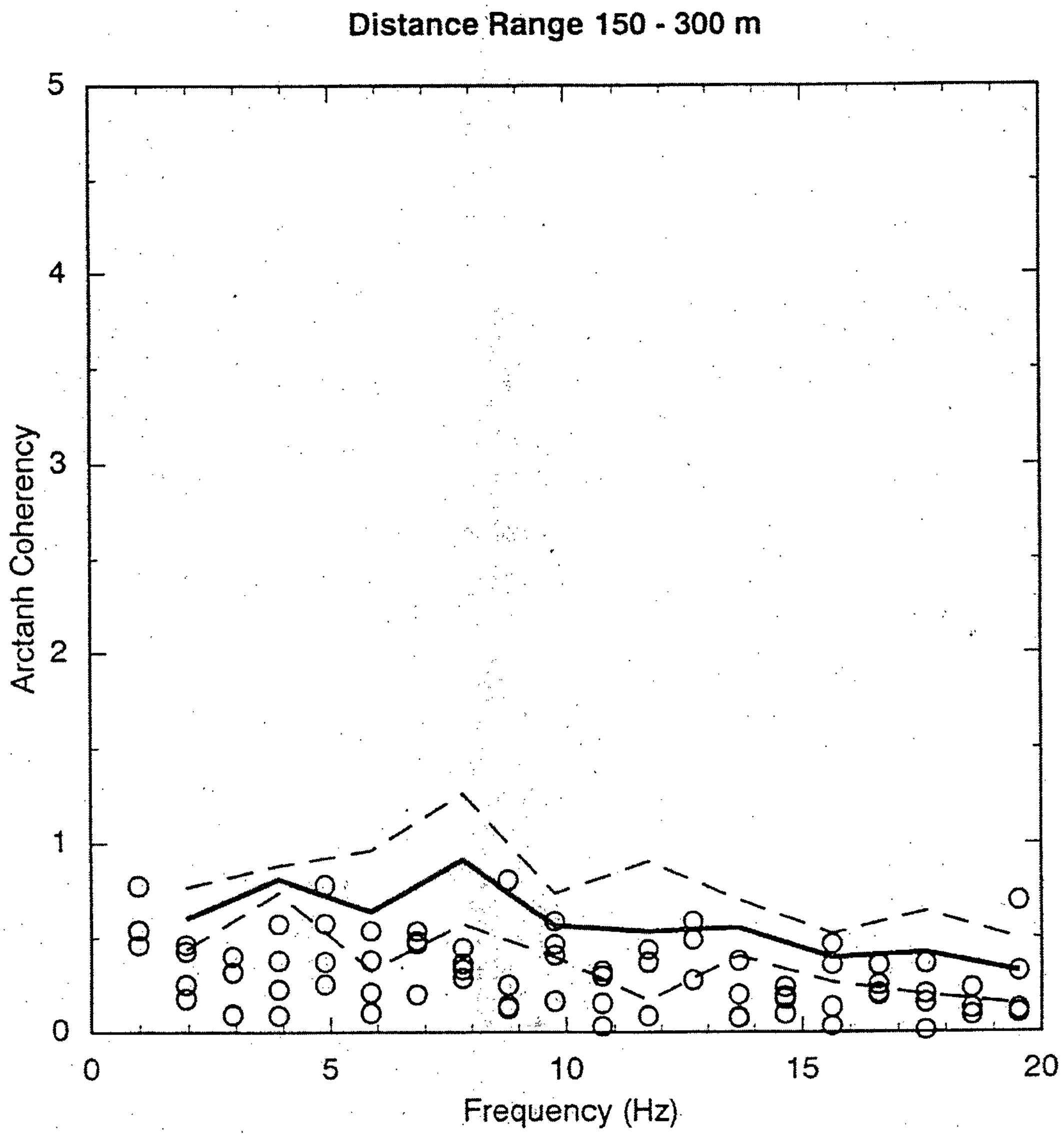

Figure 6-12. Comparison of coherency from ambient noise with the coherency from small earthquakes at the EPRI Parkfield array. Separation distance 150-300 m.

7

REFERENCES

Abrahamson, N. A., J. F. Schneider, and J. C. Stepp (1991). Empirical spatial coherency functions for application to soil-structure interaction, *Earthquake Spectra*, 7, 1-28.

Abrahamson, N. A. (1992). Spatial variation of earthquake ground motion for application to soil-structure interaction, EPRI Report 2978-1.

Anderson, D. G. and H. T. Tang (1987). Summary of soil characterization program for the Lotung Large-scale seismic experimnet, *Proc: Workshop on Lotung Large-Sacle Seismic Experiment*, EPRI, Palo Alto, CA, December 1987.

Bonamassa, O., J. E. Vidale, H. Houston, and S. Y. Schwartz (1991). Directional site resonances and the infludence of near-surface geology on ground motions, *Geophysical Research Letters*, **18**, 901-904.

Chang, C.Y., M. S. Power, Y. K. Tang, and C. M. Mok (1988). Evidence of nonlinear soil response during a moderate earthquake, Twelfth Inter. Conf. Soil. Mech. and Foundation Eng., August 13-18, 1989, Rio de Janeiro, Brazil.

Electric Power Research Institute (1988). Geological and geophysical characterization of the site of the Parkfield dense seismic array, RP2556-40.

Enochson, L. D. and N. R. Goodman (1965). Gaussian approximations to the distributions of sample coherence, Tech Report, AFFDL-TR-65-57, Wright-Patterson Air Force Base.

Fletcher, J. B., L. M. Baker, P. Spudich, and P. Goldstein. (1991?). The USGS Parkfield, California, dense seismographic array-UPSAR, *Bull. Seism. Soc. Am.*,

Hanson, R. (1992). Personal Communication.

Katayama, T., F. Yamazaki, F., S. Nagata, L. Lu, and T. Turker (1990). Development of strong motion database of the Chiba seismometer array, Earthquake Disaster Mitigation Engineering, Institute of Industrial Science, University of Tokyo, Report No. 90-1 (14).

Mueller, C. S, E. Sembera, and L. Wennerberg (1994). Digital recordings of aftershocks of the May 2, 1983 Coalinga, California Earthquake, U. S. Geol. Surv. OFR 84-697.

Mueller, C. and G. Glasmoyer (1990). Digital recordings of aftershocks of the 17 October 1989 Loma Prieta, California, Earthquake, U. S. Geol. Surv. OFR 90-503.

Owens, T. J., P. N. Anderson, and D. E. McNamara (1991). The 1990 Pinyon Flat high frequency array experiment, An IRIS Eurasian seismic studies program passive source experiment, PASSCAL Data Report #91-002.

Pavlis, G. (1992). Personal Communication.

Salsman, M. and R. Forshee (1988). Strong motion data from the Hollister earthquake of February 20, 1988, U. S. Geol. Surv., OFR 88-565.

Schneider, J.F., N.A. Abrahamson, P.G. Somerville, and J.C. Stepp (1990). Spatial variation of ground motion from EPRI's dense accelerograph array at Parkfield, California, Proc. Fourth U.S. Nat. Conf. on Earthquake Eng., EERI, Palm Springs, 375-384.

Smith, S. W., J. E. Ehrenberg, and E. N. Hernandez (1982). Analysis of the El Centro Differential Array for the 1979 Imperial Valley Earthquake, *Bull. Seism. Soc. Am.*, 72, 237-258.

Somerville, P.G., J.P. McLaren, and C.K. Saikia (1988). Site-specific estimation of incoherence of strong ground motion, Proc. Earth. Engin. Soil Dyn., Recent Advances in Ground Motion Evaluation, ASCE, Park City, Utah, 188-202.